

# Looking for Rings and Tides in Transiting Exoplanets

Akinbowale Babatunde Akinsanmi

Program Doutoral em Astronomia  
Departamento de Física e Astronomia  
2021

**Orientador**

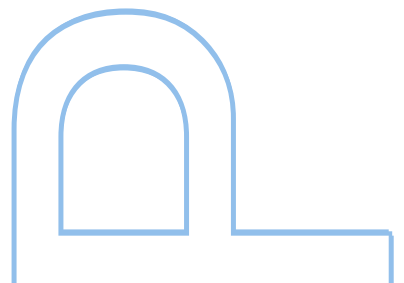
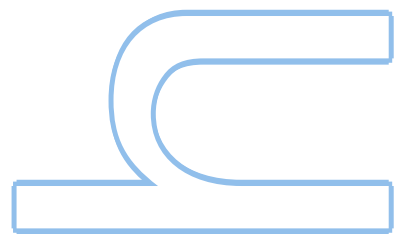
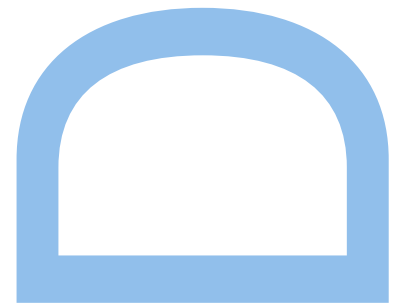
Susana C. C. Barros, Investigador, Instituto de Astrofísica

**Coorientador**

Nuno C. Santos, Professor Auxiliar, Faculdade de Ciências

**Colaborador**

Mahmoudreza Oshagh, Investigador, Instituto de Astrofísica de Canarias, Spain



LOOKING FOR RINGS AND TIDES IN TRANSITING EXOPLANETS

by

Akinbowale Babatunde Akinsanmi

A thesis submitted in conformity with the requirements  
for the degree of Doctor of Philosophy  
Graduate Department of Departamento de Física e Astronomia  
University of Porto

© Copyright 2021 by Akinbowale Babatunde Akinsanmi

# Dedication

*To my wife, Kemi, and unborn son, Erin André.*

*“The opportunity of a lifetime must be seized within the lifetime of the opportunity”* wrote Leonard Ravenhill. Studying astronomy was an opportunity to do that which I believed was bound to be intriguing and extremely challenging (at least for me). But in the words of Hellen Keller *“Life is either a daring adventure or nothing at all”* and I certainly would not settle for nothing.

## Acknowledgements

I would like to express my sincere gratitude to my supervisors Susana Barros and Nuno Santos without whom I probably would not have a reason to write this acknowledgement anyways. Their advice, trust and encouragements gave me the much needed support throughout the Ph.D. I would say “let’s do it again” but I think I could only survive the rigours of a Ph.D once in my lifetime. The road ahead would certainly keep us bound (gravitationally or any other way). I also have to thank Mahmoud Oshagh who provided me with tonnes of scientific and life advises that helped me navigate complex situations.

I also would like to extend my gratitude to all the people I met along this road who have supported me scientifically, socially, and emotionally. This list is so long that I best not name each one; from Colleagues, Researchers, Administrators, and Professors at IA to Collaborators and Friends from workshops and conferences. I also thank my Nigerian friends in Porto with whom I have shared several pleasant moments that made my stay in Porto feel “less foreign”.

A special gratitude to my darling wife, Kemi, who stood by me all through the ups and down of this Ph.D, keeping me grounded and balanced at at times. Perhaps, we can say we did this together. My appreciation further goes to my mother and siblings for their encouragements and immense love throughout this journey despite being far from home.

Finally, I acknowledge the financial support from Fundação para a Ciências e a Tecnologia (FCT - Portugal) though the PhD::Space fellowship PD/BD/135226/2017. This work was also supported by FCT through national funds (PTDC/FIS-AST/28953/2017) and by FEDER through COMPETE2020 - Programa Operacional Competitividade e Internacionalização (POCI-01-0145-FEDER-028953).

# Abstract

With the ever increasing number of detected exoplanets, detailed characterisation of these planets has become important which can allow better understanding of their shapes, interior structures, atmospheric composition, and can reveal the presence of satellites. Transiting planets present excellent opportunities to measure several properties that are important for planet characterisation. This thesis is focused on detecting rings and shape deformation (due to rotation and tides) in transiting exoplanets. These features are yet to be observed in exoplanets but are expected from theory or due to their prevalence amongst the planets of the Solar System.

The detection of ringed exoplanets would increase our understanding of the formation and evolution of ring systems. I present and develop upon a ringed planet transit tool, *SOAP3.0*, which can be used to probe for the presence of rings in transit light-curves and Rossiter-McLaughlin signals. I used *SOAP3.0* to model the light-curve of the long period planet, HIP 41378f showing that the presence of rings can explain the observed transit signal and provide an explanation for its anomalously low density.

Deformation of short period planets are expected due to the strong tidal forces acting on them by virtue of their proximity to their host stars. I showed that this deformation can be detectable from high-precision transit observations by modelling the planet shape as a triaxial ellipsoid and adapting a transit tool to generate the expected light-curve. Furthermore, the transit model allows to measure the second fluid Love number  $h_f$  of a planet which provides valuable insight into its interior structure. I also used the transit tool to identify promising targets to detect tidal deformation and measure  $h_f$ . Through simulations, I showed that precise estimates of the stellar limb darkening coefficients are required to detect tidal deformation and measure  $h_f$ .

Lastly, rotation-induced oblateness is observed, to different extents, in all the Solar System planets indicating their diverse formation and evolutionary histories. Measuring the oblateness of an exoplanet can provide information on its rotation period which can in turn give insight into how it formed and evolved as well as its atmospheric dynamics. I showed, for the first time, that the effect of oblateness can be observed in Rossiter-McLaughlin signals which can be combined with light-curve observations to better constrain oblateness. I also probed for oblateness in the light-curve of confirmed long-period planets, finding that Kepler-46b shows hints of a large oblateness of 0.173 indicative of a fast rotation rate of  $\sim 24 \text{ km s}^{-1}$ .

The tools developed within this thesis are useful in further probing for these subtle features in the high-precision transit observations expected from upcoming instruments such as *PLATO* and *JWST*.

# Resumo

Com o número cada vez maior de exoplanetas detectados, a caracterização detalhada destes planetas tornou-se importante, o que pode permitir uma melhor compreensão de suas formas, estruturas internas, composição atmosférica, e pode revelar a presença de satélites. Os planetas em trânsito apresentam excelentes oportunidades para medir várias propriedades importantes para a caracterização de planetas. Esta tese foca-se na detecção de anéis e deformações de forma (devido à rotação e marés) em exoplanetas que transitam a sua estrela. Estas características ainda não foram observadas em exoplanetas, mas são esperadas da teoria ou devido à sua prevalência entre os planetas do Sistema Solar.

A detecção de exoplanetas anelados aumentaria a nossa compreensão sobre a formação e evolução dos sistemas com anéis. Eu apresento e desenvolvo sobre uma ferramenta de trânsito de planetas anelados, *SOAP3.0*, que pode ser usado para sondar a presença de anéis em curvas de luz de trânsito e sinais de Rossiter-McLaughlin. Eu usei *SOAP3.0* para modelar a curva de luz do planeta de longo período, HIP 41378 f, mostrando que a presença de anéis fornece uma explicação para sua densidade anormalmente baixa.

A deformação de planetas de curto período é esperada devido às fortes forças de maré agindo sobre estes, em virtude de sua proximidade com as estrelas hospedeiras. Eu mostrei que esta deformação pode ser detectada a partir de observações de trânsito de alta precisão, ao modelar a forma do planeta como um elipse triaxial e adaptando uma ferramenta de trânsito para gerar a curva de luz esperada. Além disso, o modelo de trânsito permite medir o segundo número de Love fluido  $h_f$  de um planeta, o que fornece informações valiosas sobre a sua estrutura interna. Também usei a ferramenta de trânsito de maneira a identificar alvos promissores para detectar a deformação das marés e medir  $h_f$ . Através de simulações, mostrei que estimativas precisas dos coeficientes de limb darkening de estrelas são necessárias para detectar a deformação da maré e medir  $h_f$ .

Por último, o achatamento induzido por rotação é, em diferentes graus, observado para todos os planetas do Sistema Solar, indicando as sua diversa formação e histórias evolutivas. Medir o achatamento de um exoplaneta pode fornecer informações sobre o seu período de rotação e por sua vez dar uma ideia de como este planeta se formou, evoluiu, bem como da sua dinâmica atmosférica. Eu mostrei, pela primeira vez, que o efeito do achatamento pode ser observado nos sinais de Rossiter-McLaughlin que podem ser combinados com observações da curva de luz para melhor restringir o achatamento. Também testei achatamento em planetas confirmados de longos períodos, com Kepler-



46 b mostrando sinais de grande achatamento, 0,173, indicativo de uma rotação rápida de  $\sim 24 \text{ km s}^{-1}$ .

As ferramentas desenvolvidas nesta tese são úteis para estudar mais a fundo estas subtis características em observações de trânsito de alta precisão, esperadas de futuros instrumentos como *PLATO* e *JWST*.

# Contents

<b>Acknowledgements</b>	<b>iv</b>
<b>Abstract</b>	<b>v</b>
<b>Resumo</b>	<b>vii</b>
<b>1 Introduction</b>	<b>1</b>
1.1 Overview . . . . .	1
1.2 Detection Methods . . . . .	3
1.3 Thesis Focus . . . . .	15
<b>2 Analysing Transit data and Detecting Features</b>	<b>16</b>
2.1 Analysing Light-curve Data . . . . .	17
2.2 Transit Analysis . . . . .	24
2.3 Probing features in transit light-curves . . . . .	30
<b>3 Exoplanetary Rings</b>	<b>36</b>
3.1 Motivation . . . . .	37
3.2 Properties of planetary rings . . . . .	38
3.3 SOAP3.0 ringed planet transit tool . . . . .	41
3.4 Ringed planet transit signals . . . . .	43
3.5 Rings around Low-Density Planets . . . . .	46
<b>4 Tidal Deformation of Planets</b>	<b>58</b>
4.1 Planetary interiors and Love numbers . . . . .	59
4.2 Effects of tidal deformation . . . . .	61
4.3 Modelling tidal deformation . . . . .	62
4.4 Detectability of planet deformation and measurement of planet Love number	72
4.5 Discussion . . . . .	75

4.6	Summary and related works . . . . .	81
<b>5</b>	<b>Exoplanetary Oblateness</b>	<b>83</b>
5.1	Introduction . . . . .	84
5.2	Modelling oblate planet transits . . . . .	85
5.3	Oblateness-induced signature . . . . .	87
5.4	Detecting oblateness . . . . .	90
5.5	Discussion and Summary . . . . .	99
5.6	Probing for oblateness in light-curves of confirmed planets . . . . .	102
<b>6</b>	<b>Conclusions</b>	<b>108</b>
6.1	Summary . . . . .	108
6.2	Future Prospects . . . . .	111
	<b>Glossary</b>	<b>113</b>
	<b>Bibliography</b>	<b>115</b>

# List of Tables

2.1	Evidence categories for the Bayes factor . . . . .	30
2.2	Fiducial transit parameters adopted in the toy problem . . . . .	32
2.3	Priors and posterior estimates of parameters of the toy model. . . . .	34
3.1	Adopted parameters for the Saturn-like ringed planet . . . . .	44
3.2	Parameters of HIP 41378 f . . . . .	47
3.3	Adopted priors for model comparison on HIP 41378 f . . . . .	51
4.1	Confirmed planets with expected radial deformation greater than 5% . .	66
4.2	Adopted priors in fit of simulated light-curve of deformed WASP-103 b. .	73
4.3	Number of transits required to reach 50ppm/min noise level. . . . .	77
4.4	Results of LDC tests and $h_f$ values recovered. . . . .	79
5.1	Adopted system parameters of the hypothetical long period oblate planet.	91
5.2	Adopted priors for MCMC fit of simulated oblate planet transit. . . . .	96
5.3	Photon noise level per integration with different observational instruments.	100
5.4	Parameters of selected targets for probing oblateness. . . . .	103
5.5	Adopted priors and result of model comparison for Kepler-46b . . . . .	105

# List of Figures

1.1	Period-Mass-Radius plot of confirmed exoplanets . . . . .	2
1.2	Cumulative exoplanet detections by year and method . . . . .	3
1.3	Schematic of the RV method and a sample signal . . . . .	5
1.4	Schematic of transit light-curves and the observed light-curve of the first detected transiting exoplanet . . . . .	7
1.5	Examples of false positive scenarios in planetary transit detections . . . . .	10
1.6	Illustration of stellar limb darkening . . . . .	12
1.7	Illustration of the RM effect and the generated signal. . . . .	14
2.1	Contributions to the observed light-curve from a space telescope . . . . .	18
2.2	Illustration of the time scale of different stellar noise sources. . . . .	19
2.3	Analysis of the WASP-19 light-curve. . . . .	22
2.4	The signature of limb darkening feature in toy problem . . . . .	32
2.5	Posterior distribution of parameters of the LD and non-LD models. . . . .	34
2.6	Fit of LD and non-LD model to simulated LD transit in the toy problem . . . . .	35
3.1	Schematic of ring orientation . . . . .	42
3.2	Transit light-curve and RM signal of a Saturn-like ringed planet. . . . .	44
3.3	Contour plots showing variation in derived parameters from ring planet fit. . . . .	45
3.4	Spherical planet model fit to the C18 data of HIP 41378 <i>f</i> . . . . .	48
3.5	Radius distribution of planets with similar masses to HIP 41378 <i>f</i> . . . . .	49
3.6	Posterior of parameters of the ringed planet and planet-only models . . . . .	52
3.7	Planet-only and ringed planet model fits to C18 SC data of HIP 41378 <i>f</i> . . . . .	54
3.8	C5 SC Light-curve of the planet-only and ringed planet models. . . . .	54
3.9	Schematic of the ringed planet solution of HIP 41378 <i>f</i> . . . . .	55
4.1	Schematic of triaxial ellipsoid . . . . .	63
4.2	Quantification of tidal deformation as a function of distance to the star . . . . .	64
4.3	Illustration of the varying projected area of the ellipsoid with phase. . . . .	67

4.4	Comparison of ellipsoidal model light-curves of different $h_f$ values . . . . .	69
4.5	Spherical planet fit to the simulated light-curve of deformed WASP-103b . . . . .	71
4.6	Deformation signature and amplitude of different short-period planets. . . . .	71
4.7	Posterior distributions of parameters of the simulated deformed WASP-103 b. . . . .	74
4.8	Detectability of deformation in WASP-103b considering different noise levels. . . . .	75
4.9	Posterior distributions of parameters when fitting the LDCs. . . . .	80
5.1	Illustration of the ring planet model used to describe an oblate planet . . . . .	86
5.2	Oblateness-induced signatures in transit signals of HD 189733 b . . . . .	88
5.3	Contour plots showing amplitude of observable oblateness-induced signal . . . . .	93
5.4	Variation of RV oblateness amplitude at different spin-orbit angles . . . . .	94
5.5	Oblateness-induced signal for oblate planet with $\theta=45^\circ$ , $b=0.7$ . . . . .	94
5.6	Detectability of oblateness as a function of instrumental noise . . . . .	96
5.7	Posterior distribution when fitting oblate planet signals with 400 ppm 1 m s <sup>-1</sup> noise added. . . . .	97
5.8	Posterior of $f$ from simultaneous fit of light-curve and RM signal. . . . .	99
5.9	Posterior of parameters of the competing models for Kepler-46 b. . . . .	105
5.10	Oblate and spherical model fits to Kepler-46 b . . . . .	106
5.11	1D posterior distribution of $f$ for Kepler-302 c, TOI-216 c, and Kepler-167 e. . . . .	106
6.1	Projected area of deformed WASP-103b as a function of orbital phase. . . . .	112

# Chapter 1

## Introduction

*“There are infinite worlds both like  
and unlike this world of ours.”*

---

— Epicurus, 341 - 270 BC)

This thesis deals with the characterisation of planets orbiting stars other than the Sun, called *exoplanets*. The particular focus is to search for elusive features that are yet to be detected around exoplanets even though they are expected either from theory or observation of the Solar System planets. In this context, the aim is to contribute to advancing the search for planetary rings, rotation-induced oblateness and tidal deformation in exoplanets, all of which remain challenging to detect. This first chapter gives a brief overview of the exoplanetary field. Here, I summarise the methods by which exoplanets are detected and characterised which will be duly referenced in later chapters relating to the induced effects of the aforementioned features. The chapter concludes with the structure of the thesis.

### 1.1 Overview

Humans have long stared at the night sky and wondered about the existence of worlds beyond Earth and even the possibility that some of these could host life. This curiosity is one of the main motivations of the exoplanet field and continues to drive discoveries in the field till this day. The field really only became prominent and experienced a surge after the discovery of a Jupiter-like exoplanet, 51 Pegasi b, orbiting a Solar-like star (Mayor and Queloz, [1995](#)). The planet orbits much closer to its host star than any of the Solar System planets at a distance of only 0.05 AU (Astronomical Units) and a period of

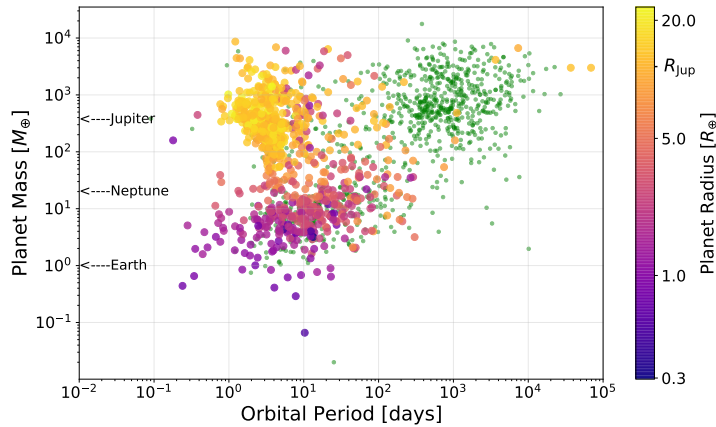


Figure 1.1: Period-Mass-Radius plot of confirmed exoplanets. Green points represent planets without radius measurements. Data from [NASA Exoplanet archive](#)

4.2 days (Mercury’s orbit is over 7 times farther from the Sun with a period of 88 days). This discovery was revolutionary, and was awarded the 2019 Nobel prize in Physics, because it challenged the theoretical expectations of planetary systems architecture and paved the way for many more exoplanet detections. Once it was found that giant planets could orbit close to their stars and not only in distant cool regions of the system, the gateway to exoplanet discoveries was immediately flung open. Now exoplanets are literally everywhere, numbering over 4300, with incredibly diverse properties than is seen within the Solar System.

Fig. 1.1 shows the diversity of exoplanets in orbital period, mass, and radius. Their radii and masses range widely from less than that of Earth to a few times greater than Jupiter. Exoplanets can be classified according to their masses - those in the mass range  $\sim 2 - 10 M_{\oplus}$  (Earth masses) are referred to as Super-Earths, those between  $10 - 100 M_{\oplus}$  as Neptunes and beyond  $100 M_{\oplus}$  as Jupiters. The deuterium burning limit of  $\sim 13 M_{\text{Jup}}$  (Jupiter masses) is usually considered the maximum mass of a planet before it is referred to as a brown dwarf or low mass star (Spiegel et al., 2011). In Fig. 1.1, the cluster of high-mass (and high-radius) planets with periods less than 10 days are referred to as hot-Jupiters, similar to the case of 51 Peg b. They are called “hot” because they are highly irradiated by their host stars which increases their equilibrium temperatures. A second cluster of planets can also be noticed corresponding to a population of hot or warm Super-Earths and Neptunes with periods less than 100 days while the third visible cluster are Jupiter-sized planets with long orbital periods. Ultimately, the direction of discovery is going towards the detection of terrestrial planets in their host star’s habitable zone, which is a distance from a star where the planetary conditions allow water to exist in liquid form.



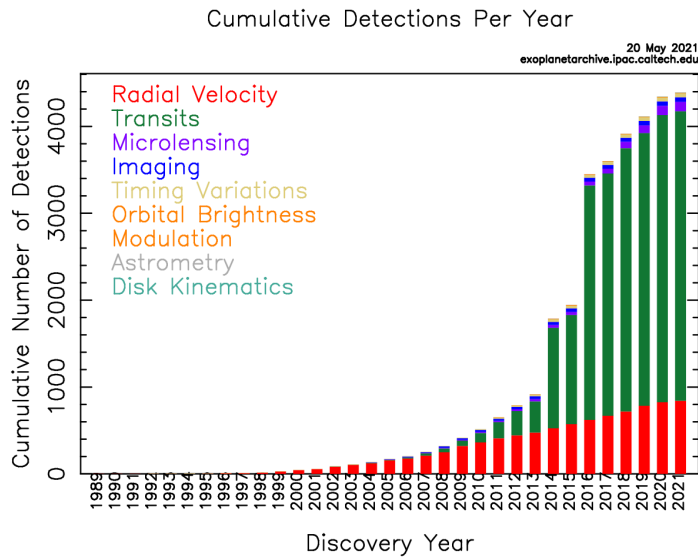


Figure 1.2: Cumulative number of exoplanet detections by year and method. Courtesy: [NASA Exoplanet archive](https://exoplanetarchive.ipac.caltech.edu)

It is important to note that the apparent populations of the detected planets are heavily influenced by our current detection methods, which are biased in the types of planet they can detect, as will be discussed in the next section.

## 1.2 Detection Methods

There are several methods employed to detect exoplanets. As shown in Fig. 1.2, the majority of exoplanets have been detected using the transit and Radial Velocity (RV) methods. This section presents an overview of both methods as they are the main methods used in the scope of this thesis (see e.g., Perryman, 2018; Santos et al., 2020, for a description of the other methods). Together, both methods provide complementary information that allows for better characterisation of exoplanets.

### 1.2.1 Radial Velocity (RV) Method

The RV method takes credit for the 1995 discovery of 51 Peg b and it remained the major exoplanet discovery method for more than a decade until it was surpassed by the transit method particularly due to the barrage of discoveries enabled by the *Kepler* space telescope (Borucki et al., 2010).

The presence of a planet around a star causes both the planet and star to orbit around the barycenter (center-of-mass) of the system. This holds true for any other stellar companion. As the star is significantly more massive than the planet, the location of the barycenter is closer to the star, usually within the star or close to its surface.

The RV method finds planets by searching for Doppler shifts in the spectral lines of the star as it moves towards and away from the observer due to gravitational interaction with the planet. As depicted in the left panel of Fig. 1.3, when the star approaches the observer, its spectral lines are shifted from their rest frame wavelength towards shorter wavelengths (blue-shift), whereas when the star recedes, the lines are red-shifted to longer wavelengths. The shift in wavelength,  $\Delta\lambda$ , compared to the rest frame value,  $\lambda_0$ , is given, in the non-relativistic limit, by

$$\frac{\Delta\lambda}{\lambda_0} = \frac{V_r}{c}, \quad (1.1)$$

where  $c$  is the speed of light and  $V_r$  is the line-of-sight (radial) velocity of the star relative to the observer which depends on the orbital inclination of the planet,  $i_p$ . Thus,  $\Delta\lambda$  is negative when the lines are blue-shifted and positive when red-shifted. The RV signal is given by

$$V_r = K [\cos(\omega + \nu) + e \cos \omega] + \gamma, \quad (1.2)$$

referred to as a Keplerian function where  $\gamma$  is the proper motion of the barycenter,  $e$  is the eccentricity,  $\omega$  is the argument of periastron, and  $\nu$  is the true anomaly. The semi-amplitude of the RV signal,  $K$ , for a planet with period,  $P$ , around a star of mass,  $M_*$ , is given (e.g., in Perryman 2018) by

$$K = \frac{28.4 \text{ m s}^{-1}}{\sqrt{1 - e^2}} \frac{M_p \sin i_p}{M_{\text{Jup}}} \left( \frac{M_*}{M_\odot} \right)^{-2/3} \left( \frac{P}{1 \text{ yr}} \right)^{-1/3}. \quad (1.3)$$

With the equations above, the RV signal induced by an orbiting planet can be calculated. The right panel of Fig. 1.3 shows the simulated RV signal of a Jupiter-mass planet with  $P=1$  yr and compares the RV signal shape for a circular orbit and an eccentric one with  $e = 0.5$  and  $\omega = 95^\circ$ .

From Eq. 1.3, we see that the RV method favours the detection of more massive and shorter period planets since they induce larger RV variations. Notice how in Fig. 1.1 there are indeed only a few Earth-mass planets. A Jupiter-, Neptune-, and Earth-mass planet with an orbital period of 1 yr around a Solar-mass star will produce RV variations with semi-amplitude of 28.4, 1.53 and 0.09  $\text{m s}^{-1}$  respectively. Therefore very precise RV measurements are required to detect Earth-mass planets. Current spectrographs, such as *HARPS* (High Accuracy Radio Velocity Planet Searcher; Pepe et al. 2002) installed on the ESO 3.6 m telescope in La Silla, are capable of RV precisions lower than 1  $\text{m s}^{-1}$  that allows to detect the RV signal of Super-Earth mass planets. However, *ESPRESSO* (Echelle Spectrograph for PREcision Super Stable Observations; Pepe et al. 2018) in-

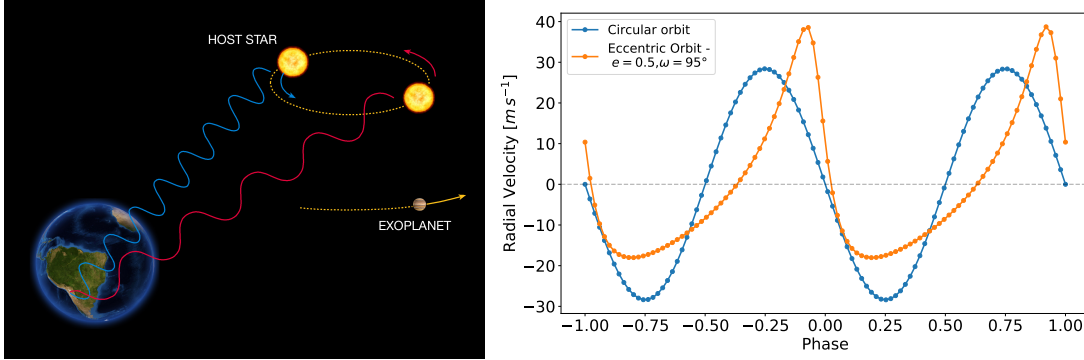


Figure 1.3: Left: Schematic of the RV method (Courtesy: ESO). Right: RV signal of a Jupiter-mass planet with a Period of 1 yr (simulated using the RadVel package; Fulton et al. 2018). The impact of eccentricity on the observed RV shape is shown.

stalled at ESO’s VLT represents the state-of-the-art instrument in RV measurements capable of RV precisions as low as  $0.1 \text{ m s}^{-1}$  (Damasso et al., 2020; Sozzetti et al., 2021).

Equation 1.3 also reveals that, when  $M_*$  is known (through spectroscopic or asteroseismic observations), the RV method can only determine the minimum mass of a planet,  $M_p \sin i_p$ , due to the unknown component of the stellar velocity perpendicular to the line-of-sight. For this reason, the observed RV variation can either be due to a low-mass planet with an orbital inclination close to  $90^\circ$  or a higher-mass planet with lesser inclination. Measuring  $i_p$ , for instance from transit observation, is thus necessary to obtain the true planetary mass  $M_p$ . The impact of inclination on the measured mass is however not so substantial. For randomly oriented orbits, the statistical probability that a planet has an inclination greater than some value  $i$  (between 0 and  $90^\circ$ ) is given by  $\mathcal{P}_i = \cos i$  which indicates that 87% of all systems will have  $i_p > 30^\circ$ , corresponding to  $\sin i_p > 0.5$ . Therefore, there’s an 87% probability that the measured  $M_p \sin i_p$  will be more than half the actual mass  $M_p$  of the planet (Lovis and Fischer, 2010; Fischer et al., 2015).

RV surveys such as the *HARPS* and *Keck* surveys of FGK stars (Howard et al., 2010; Mayor et al., 2011) at the turn of last decade detected a large population of Super-Earth and Neptune mass planets suggesting that low mass planets are more frequent than massive planets. These surveys further indicated that low mass planets are mostly part of multiplanetary systems (e.g. Lovis et al., 2011), a result that was later confirmed with transit surveys. Furthermore, the fact that the RV signal is amplified for planets around less massive stars motivated surveys to search for planets around M-dwarfs (e.g., Bonfils et al. 2013; Reiners et al. 2018) which are also the most populous stars in our galaxy.

### 1.2.2 Transit Method

The transit method is responsible for the discovery of a large number of exoplanets (3335, as at June 2021). A transit occurs when a planet passes in front of its host star from the perspective of the observer. When this occurs, the planet blocks a fraction of the stellar light causing a temporary dimming of the star's brightness. Detecting a planet by the transit method thus involves monitoring the brightness of the star in search for a periodic dip in its brightness associated with the passage of a planet. A transit light-curve is produced from the measurement of the stellar flux as a function of time (see Fig. 1.4a). The depth of the transit,  $\delta$ , is related to the area of stellar disk covered by the planet and therefore provides a measure of the planet-to-star radius ratio. For a uniform intensity star, the transit depth is given by

$$\delta \simeq \left( \frac{R_p}{R_*} \right)^2, \quad (1.4)$$

where  $R_p$  and  $R_*$  are the radii of the planet and star respectively. This shows that it is easier to detect larger planets with the transit method since they cause deeper transits. A Jupiter-sized planet transiting a Solar-like star would cause a transit depth of  $\sim 1\%$ . The transit will be even deeper if the star were smaller, making M-dwarfs once again good targets for detecting exoplanets, particularly Earth-sized ones. Combining radius measurements from transit and mass measurement from RV finally allows astronomers to estimate the bulk densities of exoplanets and compare them to those of the Solar-System planets determining if a planet is rocky or contains significant amounts of volatiles.

In more detail, a transit begins when the projected disk of the planet touches the limb of the star, known as first contact. The stellar flux decreases progressively as the planet continues to move onto the stellar disk until the entire planet disk blocks starlight at second contact. The flux level reaches a minimum and remains flat (ignoring limb darkening; see §1.2.2) until the third contact when the planet begins to exit the stellar disk causing the stellar flux to rise. The transit ends at the fourth contact as both disks no longer overlap. The time between the first and second contact is referred to as the transit ingress while the egress corresponds to the time between the third and fourth contact. Although the ingress and egress durations are usually equal, light-curve asymmetry due to orbital eccentricity, planet oblateness, or rings can cause the durations to differ.

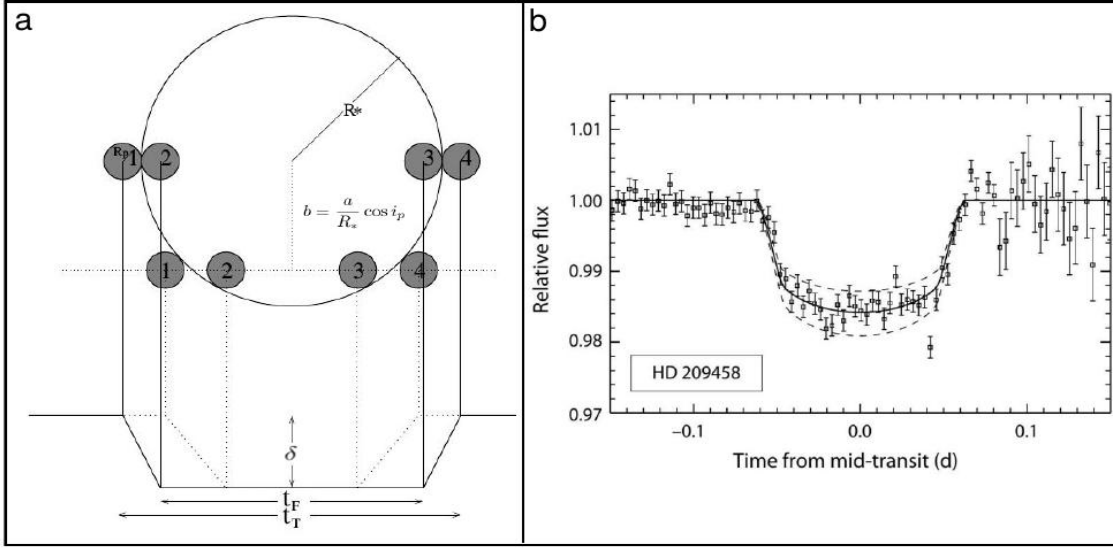


Figure 1.4: **(a)** Schematic of the transit method showing the four contact points, different impact parameter transits and the observables of the light-curve ( $\delta$ ,  $t_T$ ,  $t_F$  as described in text). Figure adapted from Seager and Mallen-Ornelas (2003). **(b)** Light-curve of the first detected transiting exoplanet HD 209458 b (Charbonneau et al., 2000).

Besides the transit depth from which the  $R_p/R_*$  is derived, other observables from transit observations that allow to derive more planetary and orbital parameters are: the duration of total transit  $t_T$  (time between contacts 1 and 4) and the duration of full transit  $t_F$  (time between contacts 2 and 3) as indicated in Fig. 1.4a. The orbital period  $P$  can also be obtained from mid-transit time ( $t_0$ ) measurements of a sequence of transits. From these, Seager and Mallen-Ornelas (2003) showed that, for circular orbits, it is possible to derive the scaled semi-major axis of the planet orbit as

$$\frac{a}{R_*} = \left\{ \frac{(1 + \sqrt{\delta})^2 - b^2[1 - \sin^2(t_T\pi/P)]}{\sin^2(t_T\pi/P)} \right\}^{1/2}, \quad (1.5)$$

where  $b$  is the impact parameter of the transit defined as the sky-projected distance, in units of stellar radii, between the centres of the star and planet at mid-transit. It is given as

$$b = \frac{a}{R_*} \cos i_p = \left\{ \frac{(1 - \sqrt{\delta})^2 - [\sin^2(t_F\pi/P)/\sin^2(t_T\pi/P)](1 + \sqrt{\delta})^2}{1 - [\sin^2(t_F\pi/P)/\sin^2(t_T\pi/P)]} \right\}^{1/2}, \quad (1.6)$$

and allows us estimate the inclination,  $i_p$ , of the planetary orbit, which can be combined with RV observation to determine a planet’s true mass. The impact parameter ranges from  $b = 0$  for a transit across the stellar centre to  $b = 1$  for a transit across the stellar limb. In the case where  $b = 1$ , only one hemisphere of the planet disk overlaps the stellar disk throughout transit in what is known as a ‘grazing transit’. In practice, a grazing transit would still include values of  $b$  until  $b = 1 + R_p/R_*$ .

Furthermore, with Kepler’s third law given by

$$P^2 = \frac{4\pi^2 a^3}{G(M_* + M_p)}, \quad (1.7)$$

where  $G$  is the gravitational constant, it is possible to obtain a transit-derived stellar density assuming that  $M_p \ll M_*$  which is usually satisfied. This is done by substituting  $\rho_* = 3M_*/4\pi R_*^3$  in Eq. 1.7 giving:

$$\rho_* = \frac{3\pi}{GP^2} \left( \frac{a}{R_*} \right)^3. \quad (1.8)$$

This is a method of estimating stellar density (independent of other methods such as asteroseismology) using only the light-curve parameters. Conversely, in fitting transit light-curve, the known stellar density can be used to place prior constraints the value of  $a/R_*$  (which indirectly determines the transit duration  $t_T$ ). See Kipping (2010b) for modifications to Eq. 1.5–1.8 for an eccentric orbit.

Clearly, transit observations provide us with a treasure trove of information, but there’s a catch: the orbit of a planet needs to be properly aligned from our point of view in order to observe a transit. This alignment requires that  $|b| < 1 \pm R_p/R_*$ , where the ‘+’ or ‘-’ sign allows for grazing transits or excludes them. This means that a transit only occurs when the projected distance between the centres of the planet and star is less than the stellar radius. Therefore, the geometric probability that a randomly-oriented planet transits is host star is given (e.g., in Perryman 2018) by

$$\mathcal{P}_{\text{tr}} = \left( \frac{R_* \pm R_p}{a} \right) \left( \frac{1}{1 - e^2} \right). \quad (1.9)$$

The probability implies that planets closer to their stars are more likely to transit. It also shows that transits of planets on eccentric orbits are more likely than those of circular orbit planets with the same semi-major axis since they can get closer to the star at

pericenter. The probability that a Jupiter-sized planet at 1 AU from the Sun will transit is only 0.5%. Therefore, the large sizes and proximity of hot-Jupiters makes them ideal for transit detections which explains the cluster of these planets in Fig. 1.1.

The first planet observed to transit its star was HD 209458 b (Charbonneau et al., 2000; Henry et al., 2000). With a derived radius of  $1.27 R_{\text{Jup}}$ , it confirmed that the Jupiter-mass objects detected with RV were indeed Jupiter-sized giant planets with similar densities. Figure 1.4b shows the transit light-curve of HD 209458 b (Charbonneau et al., 2000). The number of transiting planet grew rapidly after this detection with follow-ups of RV detected planets and ground-based transit surveys such as *HATNet* (Bakos et al., 2002), *OGLE* (Udalski et al., 2003), *WASP* (Pollacco et al., 2006) and *TrES* (Alonso et al., 2004) which had sufficient precision to detect these giant planets.

The first space-based transit observation was that of HD 209458 b using the Hubble Space Telescope (*HST*; Brown et al., 2001) revealing the power of space-based photometry for providing highly precise photometry capable of particularly searching for features such as rings and moons. The *Spitzer* space telescope also provided the first secondary eclipses of exoplanets as the planets HD 209458 b and TrES-1b were occulted by their stars (Deming et al., 2005; Charbonneau et al., 2005). These space-based observations motivated the first space missions to find transiting exoplanet such as *CoRoT* (Auvergne et al., 2009) and *Kepler* (Borucki et al., 2010). The *Kepler* space mission helped reveal/confirm several important clues about exoplanets. One is that super-Earths are ubiquitous<sup>1</sup> and are estimated to exist in about half of all Sun-like stars (Howard et al., 2012; Schlichting, 2018). Second is that multi-planetary systems are also very common, are dominated by super-Earths, and rarely contain transiting giant planets (Latham et al., 2011; Lissauer et al., 2011).

The *Kepler* prime mission was completed in 2013 after a failure of a second reaction wheel affected its pointing stability. The mission was modified as the *K2* mission which allowed observations of new fields of view along the ecliptic (Howell et al., 2014). The *Kepler* spacecraft was finally retired in 2018 after exhausting its fuel.

Current space missions include the Transiting Exoplanet Survey Satellite (*TESS*; Ricker et al., 2015) and the CHaracterising ExOPlanet Satellite (*CHEOPS*; Broeg et al., 2013; Benz et al., 2020). While *TESS* surveys the entire sky in sectors for transiting

---

<sup>1</sup>Recall the cluster of super-Earths with  $P < 100$  days in Fig. 1.1

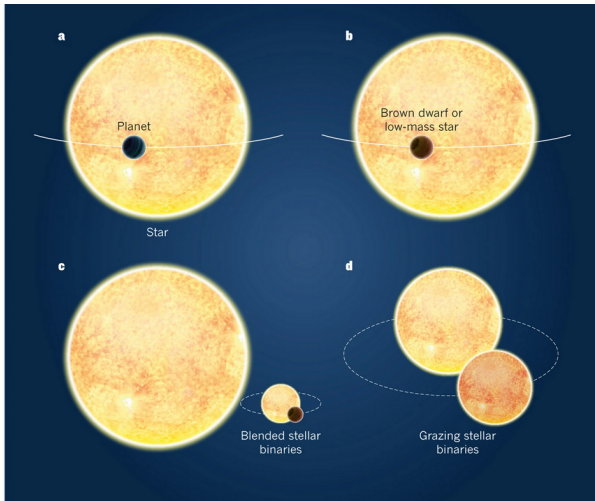


Figure 1.5: Examples of false positive scenarios in planetary transit detections. Image from Cameron (2012)

exoplanets, *CHEOPS* performs targeted observations of bright stars in order to better characterise known exoplanets. Future space missions such as the James Webb Space Telescope (*JWST*; Beichman et al., 2014), PLAnetary Transits and Oscillations of stars (*PLATO*; Rauer et al., 2014) satellite, and the Atmospheric Remote-Sensing Infrared Exoplanet Large-survey (*ARIEL*; Tinetti et al., 2016) will allow unprecedented instrumental precisions to better understand different properties of planets and their host stars.

The transit method is prone to false positives signals which mimic the characteristic light-curve of a transiting planet. These false positives signals can be due to configurations of two or more stars (see Fig. 1.5) such as grazing eclipses of a binary star, eclipsing binary in a triple system, transiting brown or white dwarf, or even a background transiting planet amongst others (Fressin et al., 2013; Santerne et al., 2013). Therefore, transiting planets need to be validated usually using other detection methods (such as the RV method) or statistical techniques that calculate the False Positive Probability taking into account the transit shape, duration, depth and derived stellar density (Torres et al., 2011; Morton, 2012; Barros et al., 2014b).

### Limb darkening

The transit illustration in Fig. 1.4a assumes that the stellar intensity is uniform from centre to limb, leading to a flat-bottomed transit and a direct relation between the transit depth and radius ratio (Eq. 1.4). In reality, the stellar disk is brighter at the centre and darkens progressively towards the limb, an effect known as limb darkening. Due to this effect, the transit will be deeper at mid-transit since the planet obscures more stellar



intensity at the centre than any other region. Limb darkening thus causes the light-curve to become round at the bottom, and also at ingress and egress as seen in Fig. 1.4b for the HD 209458 b transit. Limb darkening occurs due to the stratification in stellar density and temperature with altitude. When observing a transit, the line-of-sight towards the limb is oriented at an angle  $\phi$  from the normal to the stellar surface causing an optical depth  $\tau$  of unity to be attained at a higher altitude where the stellar temperature and intensity are lower (see Fig. 1.6).

The limb darkening is usually represented as a function of  $\mu = \cos \phi$  ( $\mu = 1$  at the centre of the stellar disk and zero at the limb). Several parametric limb darkening laws have been proposed which attempt to approximate the intensity profile from stellar atmospheric models. Some examples of popular limb darkening laws are:

- The Linear law (Milne, 1921):

$$I(\mu)/I(1) = 1 - u(1 - \mu). \quad (1.10)$$

- The quadratic law (Kopal, 1950):

$$I(\mu)/I(1) = 1 - u_1(1 - \mu) - u_2(1 - \mu)^2. \quad (1.11)$$

- The square-root law (Diaz-Cordovez and Gimenez, 1992):

$$I(\mu)/I(1) = 1 - u_1(1 - \mu) - u_2(1 - \sqrt{\mu}). \quad (1.12)$$

- The power-2 law (Hestroffer, 1997; Maxted, 2018):

$$I(\mu)/I(1) = 1 - u_1(1 - \mu^{u_2}). \quad (1.13)$$

- Four parameter law (Claret, 2000):

$$I(\mu)/I(1) = 1 - \sum_{i=1}^4 u_i(1 - \mu^{i/2}). \quad (1.14)$$

- The three-parameter law: (Sing et al., 2009):

$$I(\mu)/I(1) = 1 - \sum_{i=2}^4 u_i(1 - \mu^{i/2}). \quad (1.15)$$

where  $I(1)$  is the intensity at the centre of the disk and  $u_i$  are the limb darkening coefficients (LDCs) for each law. For all of these laws, a strict constraint is that the stellar intensity is everywhere positive and decreases from centre to limb. Estimates of the coefficients can be obtained from theoretical tables (e.g., Claret and Bloemen, 2011) calculated considering the properties of the host star (such as the effective temperature, logarithm

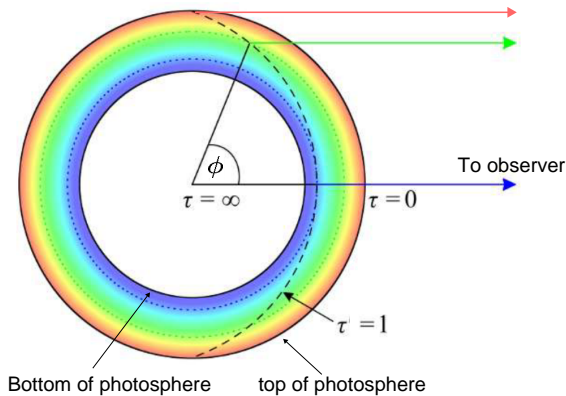


Figure 1.6: Illustration of stellar limb darkening. Coloured rings represent altitudes in the stellar photosphere with different temperatures from hotter (blue) to cooler (red) layers. The dashed line shows the surface with optical depth  $\tau=1$ . Adapted from Müller (2015)

of the surface gravity and metallicity) and the wavelength range of the transit observation.

As limb darkening modifies the shape of a light-curve, it can affect the inferred parameters like the radius ratio and other higher-order effects such as those sought-after in this thesis (Csizmadia et al., 2012; Short et al., 2019; Akinsanmi et al., 2019). Therefore, accurate treatment of limb darkening is crucial especially for very precise transit measurements (Kipping, 2013a; Espinoza and Jordán, 2015). The effect of limb darkening on light-curves is wavelength-dependent and is reduced at longer wavelength where the contrast between the emergent flux from the centre and limb is minimised. So transits observations at longer passbands have flatter transit bottoms.

### Transit Timing and Transit Duration Variations

Transiting planets in multi-planetary systems may have non-keplerian orbits due to gravitational interaction between the planets. Such interactions meddle with the usual clockwork precision of periodic transits and can lead to transit timing variations (TTV) and transit duration variations (TDV). If the transit of a planet is detected, deviations from a linear ephemeris can reveal the presence of an additional planet in the system, even if non-transiting, and also allow determination of its mass, period and eccentricity (Agol et al., 2005; Holman, 2005; Nesvorný, 2019). TTVs are stronger for planets near mean-motion resonances in which the ratio of periods of two planets is close to the ratio of small integers. The first significant TTV detection was in the Kepler-9 system which showed large-amplitude TTVs due to two Saturn-sized planets (Holman et al., 2010). After that, TTVs have been observed in more than 100 systems (Holczer et al., 2016) but the first

case of discovery and complete characterisation of a non-transiting planet was for Kepler-46 (Nesvorný et al., 2012). Given the prevalence of super-Earths in multi-planetary systems, several of their masses have been measured by TTV (e.g. Steffen et al. 2013).

One source of TDV is variation in orbital eccentricity of a planet due to resonant interaction. Eccentricity variations affect the speed and length of a transit thereby modifying the transit duration between consecutive transits. This has been observed in KOI-142 (Nesvorný et al., 2013) where the TTVs and TDVs were used to detect the non-transiting companion KOI-142 c.

Additionally, the presence of a moon around an exoplanet (exomoon) could cause observable TTVs and TDVs since a moon gravitationally perturbs the planet along its orbit. TTVs and TDVs have even been proposed as methods to detect them (Szabó et al., 2006; Kipping, 2009a,b).

### Rossiter-McLaughlin signal

In addition to the photometric signal of a transiting planet, a spectroscopic transit signal can be obtained by measuring the star's RV shift during the transit of a planet. A rotating star has half of the stellar disk approaching the observer as the other half recedes. Therefore, stellar light from the approaching half will be blue-shifted whereas light from the receding half will be red-shifted due to Doppler effect (see Fig. 1.7). In the absence of a planetary transit, the shift from both halves of stellar disk will average out when integrated. However, when a planet transits the star, it first occults part of the blue-shifted (or red-shifted) half causing the disk-integrated stellar light to be slightly red-shifted (or blue-shifted).

As the planet transits across the stellar disk, it blocks different regions with varying RV components thereby causing an anomaly referred to as the Rossiter-McLaughlin (RM) effect (Rossiter, 1924; McLaughlin, 1924). Fig. 1.7 depicts how the observed RM signal varies as a planet, with same parameters, follows different paths across the star. The three paths would result in the same transit light-curve but different RM signals, so the RM signal can give us extra information about a transiting planet. Since the RM effect is sensitive to the planet's transit path, it offers information about the projected angle between the planet's orbital plane and the stellar equatorial plane which is referred to as the spin-orbit angle,  $\lambda$ . It also allows measurement of the projected stellar rotational velocity,  $v \sin i_*$ .

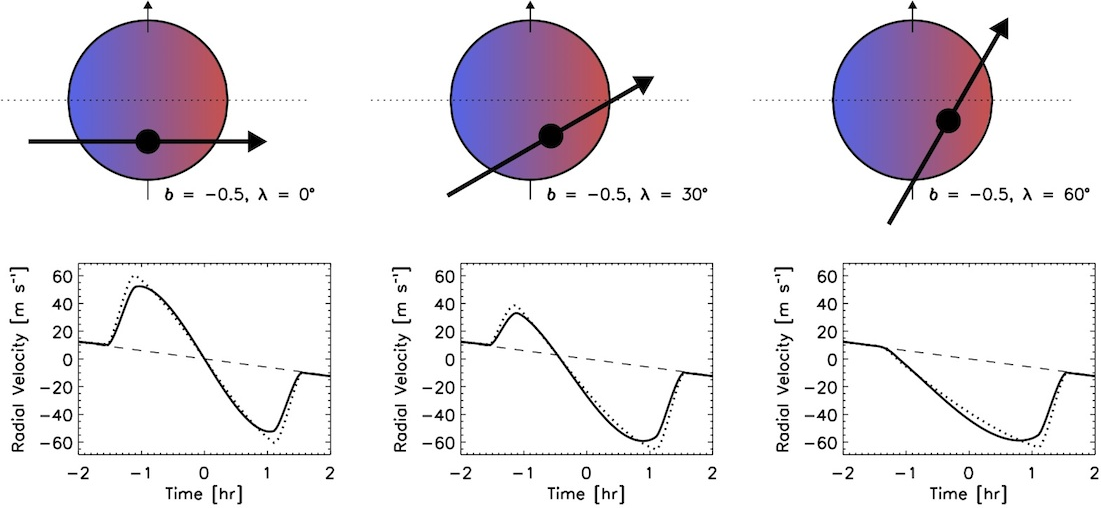


Figure 1.7: Top: Different transit paths (defined by angle  $\lambda$ ) of a planet across a rotating star. Bottom: The resulting RM signals from the different transit paths. The long dashed line indicates the stellar RV signal without a transiting planet, while the solid and dotted curves represent the RM signals with and without limb darkening respectively. From Gaudi and Winn (2007).

Fig. 1.7 shows the RM signal for different values of  $\lambda$ . A perfectly aligned planet ( $\lambda=0^\circ$ ) produces an RM signal that is anti-symmetric about the mid-transit time while the RM signal of a misaligned planet will either be asymmetric ( $\lambda=30^\circ$ ) or lead to an anomaly in only one of the stellar hemispheres ( $\lambda=60^\circ$ ).

The amplitude of RM effect,  $A_{RM}$ , is given (e.g. Triaud 2018) as

$$A_{RM} \propto \nu \sin i_* \left( \frac{R_p}{R_*} \right)^2 \sqrt{1 - b^2}. \quad (1.16)$$

The RM effect is most significant for large planets transiting fast rotating stars. Queloz et al. (2000) was the first to report observation of the RM effect for an exoplanet, HD 209458 b, measuring a spin-orbit angle of  $3.9^\circ$ . Spin-orbit angle measurements using RM observations are now regularly obtained and it has shown that exoplanets have a large diversity in  $\lambda$ , from aligned to highly misaligned and even retrograde systems (Hébrard et al., 2008; Anderson et al., 2015; Esposito et al., 2014). The distribution of spin-orbit angle can help inform migration theories and histories of exoplanets (Winn et al., 2010).

### 1.3 Thesis Focus

In deriving some of the exoplanet parameters and properties above, specifically for transiting planets, an implicit assumption has been made that the exoplanet is spherical and has no extended features. However, a departure from sphericity due to tidal deformation, oblateness or rings could alter the relationship between these parameters and impact the shape of the observed transit light-curve and RM signal. With increasing instrumental precisions, the subtle effects of these features in transit data become more prominent thereby better allowing their detection and proper characterisation.

This manuscript is composed of three distinct parts, each dealing with a different investigation of how exoplanetary transits can be used to detect and characterise tidal deformation, rings and oblateness. Therefore, the thesis should be more appropriately titled “*Looking for rings and shape deformation in transiting exoplanets*”.

In Chapter 2, I lay the ground work for identifying the signature of features in transit data, detrending methods that preserve these signatures and Bayesian approach to comparing models with and without the sought-after features. Chapter 3 is an investigation into the detection of exoplanetary rings, effects of rings to transit signals and the derived parameters, identification of suitable candidates and an analysis of a specific case. In Chapter 4, I adapt a transit tool to model the light-curve of tidally deformed planets. Afterwards, this tool was is used to investigate the detectability of tidal deformation in short-period planets and identify favourable targets. I also show how detecting tidal deformation allows to gain insight into the interior structure of planets. Chapter 5 investigates the signature of rotation-induced oblateness showing that the induced signal in spectroscopy can complement that from photometry and also presents analyses of some potential candidates. Finally in Chapter 6, I present the conclusions of my work and future outlook for the detection of these features.

# Chapter 2

## Analysing Transit data and Detecting Features

*“As long as one keeps searching, the answers come.”*

---

— Joan Baez

With the ever-increasing number of detected exoplanets, the field of exoplanetary science has been shifting away from just planet detection towards understanding the detected planets through detailed characterisation. This involves probing the composition of their atmospheres, interior structures, their potential to host satellites and other planetary features that have been observed in the Solar-System planets. The transit method is very useful in planet characterisation as it offers a wealth of information not readily accessible through other methods. It has been used to study exoplanet atmospheres through transmission spectroscopy (Lendl et al., 2017; Madhusudhan, 2018; Kreidberg, 2018a; Taberner et al., 2021), measure planet obliquity from gravity darkening due to rapid stellar rotations (Ahlers et al., 2020; Lendl et al., 2020) and from RM observations (Sanchis-Ojeda and Winn, 2011; Addison et al., 2016), and to probe for the presence of moons, rings, and trojans (Kipping, 2013a; Heising et al., 2015; Cabrera et al., 2018) amongst others.

The transit method is versatile for many studies because different features or properties modify the standard anatomy of the transit light-curve and RM signal thereby allowing to probe for their presence. *Features*, as used in this thesis, refers to astrophysical phenomena that can impact the properties of an observed transit signal. In general,

these features can be from the star or planet e.g., limb darkening, gravity darkening, stellar spots, moons, rings or planet shape deformations amongst others.

This thesis focuses on using the transit method to probe for the presence of planetary features. I mainly focus on the light-curve effects as they are more promising to detect the signatures of the features. This chapter begins with a description of statistical and computation methods used in analysing and fitting transit light-curves, performing inference including parameter estimation and model selection. Then I use a toy problem to describe strategies employed to identify, characterise and detect the signature of features in transit observations which will serve as a background for the investigation of tidal deformation, rings and oblateness in subsequent chapters.

## 2.1 Analysing Light-curve Data

Typically, observed light-curve data consists of stellar flux measurements, the flux uncertainties and a time value indicating when each observation was performed. The time is usually given in Barycentric Julian Date (BJD) which is a correction of the Julian Date to account for variations in the position of the Earth relative to the barycenter of the Solar System. The time between successive observation is called the cadence of the data. However, in many cases the data might have large gaps where observations were not taken due to data down-link from the spacecraft to ground, passage through the South Atlantic Anomaly (e.g., Bonfanti et al., 2021) or daytime interruptions for ground-based observations. The flux value is a measure of the amount of photons recorded by the instrument’s detector for each exposure.

The observed light-curve is often a combination of several signals: the planet transit, stellar variability, spacecraft systematics, and detector noise among others (Fig. 2.1). Transit light-curve analysis usually involves “cleaning” the data (by removing outliers, NaNs and data points with quality issues such as detector anomaly, stray light or cosmic ray hit), estimating and correcting for contamination from other sources, correcting instrumental effects and stellar variability, searching for transits, and estimating parameters by fitting (not necessarily in that order). For illustration, I analyse the simple case of WASP-19 by describing and performing some of these steps individually on the data. Note however that, in practice, some steps are usually performed simultaneously on the data.

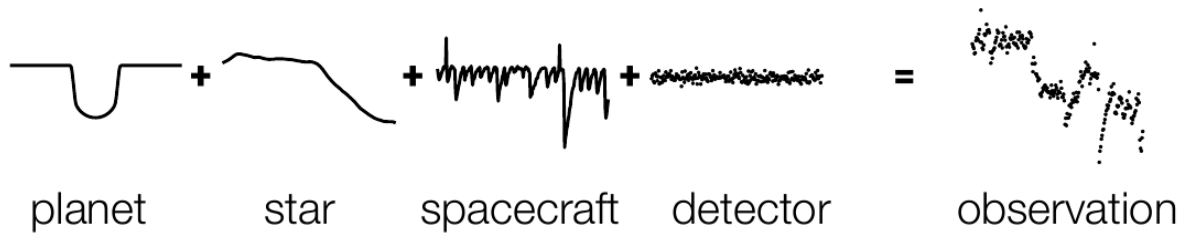


Figure 2.1: Contributions to the observed light-curve from a space telescope (Credit: Dan Foreman-Mackey).

### 2.1.1 Stellar variability

Exoplanet host stars themselves present different sources of astrophysical noise that could hinder the detection and characterisation of exoplanets. These noise sources include stellar oscillations, granulation, and magnetic active regions each with different amplitudes and timescales as shown in Fig. 2.2. Stellar oscillations are due to pressure waves originating from the stellar interior which induce correlated noise with timescales of a few minutes (5 – 15) and photometric amplitudes of 100–300 ppm (Oshagh, 2018a). Stellar granulation is due to convection on the stellar surface producing photometric variability with timescales of minutes to several hours and amplitude of around 75 ppm comparable with the transit depth of an Earth-sized planet (Gilliland et al., 2011). The magnetic activity of a star causes structures on the stellar surface referred to as active regions. These active regions could be dark spots or bright faculae. The presence of active regions on the stellar surface can induce photometric variability as the star rotates them in and out of view leading to variability timescales similar to the rotation period of the star. As such, even though one has to remove the induced variability when searching for planet transits, the presence of starspots can help deduce the stellar rotation period as we shall see in the analysis of WASP-19.

### 2.1.2 Searching for Transits in light-curve data

The sector 9 *TESS* light-curve of WASP-19 with 2-min cadence was downloaded from the Mikulski Archive for Space Telescopes (MAST) using the `LightKurve` python package (Lightkurve Collaboration et al., 2018). All points with non-zero quality flag were removed from the data to avoid introducing systematic, then a moving median filter was used to remove outliers greater than  $3\sigma$ . The header of the light-curve file provides an estimate of the level of contamination in the aperture via the “CROWDSAP” keyword which indicates the fraction of the total flux in the aperture that comes from the target



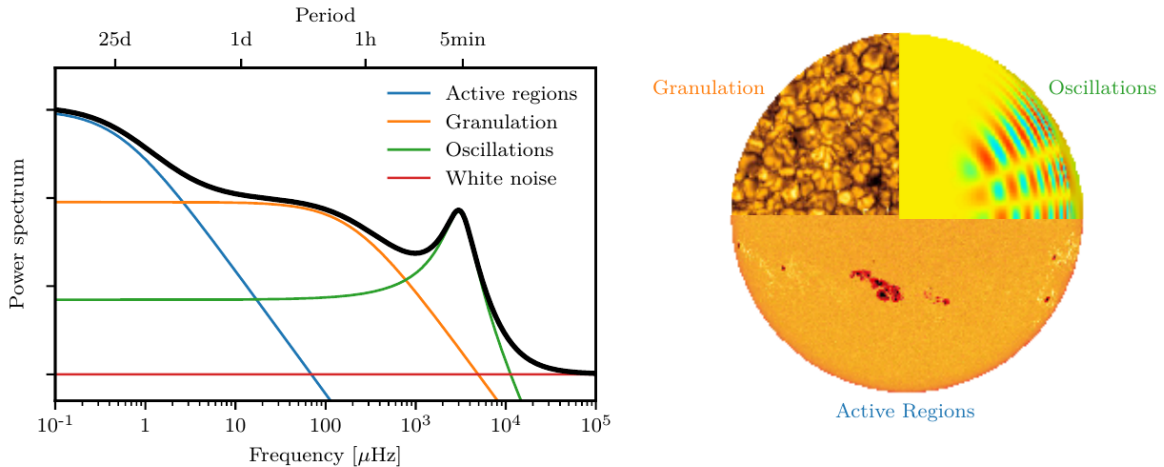


Figure 2.2: Power spectrum illustrating the time scale of different stellar noise sources. Figure from Faria (2018).

star ( $f_t$ ). For the WASP-19 observation, the “CROWDSAP” value is 0.8927 implying a contamination flux fraction ( $f_c$ ) of 0.107. The observed flux ( $F_{\text{obs}}$ ) can then be decontaminated following the prescription of Kipping and Tinetti (2010) to obtain the stellar flux ( $F_*$ ) using

$$F_* = F_{\text{obs}} \left( 1 + \frac{f_c}{f_t} \right) - \frac{f_c}{f_t}. \quad (2.1)$$

The decontaminated light-curve of WASP-19 is shown in Fig 2.3a with a large gap in between due to data down-link to Earth. We see several dips corresponding to the transit of a planet, WASP-19b, and a long-term periodic variation that can be due to the presence of stellar spots (Espinoza et al., 2019). The spacing between the dips is the orbital period of the planet. The periodicities in the data can be determined by running some variation of the Box-Least-Square (BLS) algorithm (Kovács et al., 2002) or Lomb-Scargle (LS) periodogram (Lomb, 1976; Scargle, 1982). In brief, the BLS algorithm is used to search for transit-like signals in photometric time-series by modelling the transit as a periodic box-shaped signal with four parameters: period, duration, depth and reference time. The search is performed on the data across several trial periods ranging from the shortest expected period to a maximum of half the duration of the data (to allow at least 2 transits). The best-fit of each trial period is used to construct a periodogram showing the signal power at the most likely orbital periods. A variation of the BLS, called Transit Least Squares (TLS) was recently developed to model the transit shape better,

instead of with a box, by including limb darkening effects (Hippke and Heller, 2019). It detects transits more reliably and is particularly optimised for detecting small planets. The Lomb-Scargle periodogram is used to detect periodicities in unevenly-sampled time-series making it useful in determining the period of stellar variations in light-curves and also the orbital period of a planet in RV datasets (See Zechmeister and Kürster 2009; VanderPlas 2018; Mortier et al. 2015). Both algorithms are performed individually on the WASP-19 data to recover the orbital period of the planet and period of stellar variability.

The periodogram obtained from running the BLS algorithm on the WASP-19 data is shown in Fig. 2.3b revealing an orbital period of 0.788 days for the planet. The result of the BLS gives a reference time, which is an estimate of the mid-transit time ( $t_0$ ) of the first transit in the data, and also an estimate of transit duration ( $t_T$ ). The LS periodogram is shown in Fig. 2.3c indicating a periodicity of 10.95 days attributed to the rotation period of the star (Espinoza et al., 2019).

### 2.1.3 Detrending transit data

The stellar variability, as discussed in Sect. 2.1.1, causes the flux level around each transit to vary with time. For the sake of analysing transits, it is necessary to detrend the light-curve so that the mean out-of-transit flux has no trend with time. First, it is easier to analyse the normalised data so the flux values and the errors are divided by the median flux. Several methods have been employed in the exoplanet literature to detrend light-curves such as sliding medians, Gaussian Processes (GP), spline and polynomial fitting among many others (see discussion in Hippke et al. 2019).

In the case of detrending light-curve before transit fitting (e.g., Holczer et al., 2016), it is important to preserve the transit information whilst detrending, especially when searching for features. As such, data points in and around transits are typically masked out before such detrending. Given that the period, transit duration and first time of mid-transit ( $t_0 [0]$ ) has been determined from the BLS, it is straight-forward to identify all the transits in the data using

$$t_0 [n] = t_0 [0] + n P, \quad (2.2)$$

where  $t_0 [n]$  is the mid-transit time of the  $n^{\text{th}}$  subsequent transit. For each transit  $n$ , data points within some time range on either side of  $t_0 [n]$  can be masked.

Below, I give a brief description of detrending with GPs, polynomials and filters and apply a GP to the WASP-19 data.

### Gaussian Processes

GPs are non-parametric models that attempt to infer the correlation of measured data instead of trying to fit the parameters of a function. This property makes it useful in cases where the functional form of the model is not known such as in the modelling of stochastic processes and instrumental systematics in light-curves. A GP is a collection of random variables such that the joint distribution of any of its sub-set is a joint Gaussian distribution (Rasmussen and Williams, 2006). A GP is defined by a mean function  $m(x)$  and a covariance function (or kernel)  $k(x, x')$  so that

$$f(x) \sim GP(m(x), k(x, x')), \quad (2.3)$$

where  $x$  are the observed data points. To define a GP, one thus has to define  $m(x)$  and  $k(x, x')$ . For a light-curve normalised to unity,  $m(x)$  can be set to one to define the flux baseline. The covariance function defines the smoothness, periodicity and stationarity of the GP. It can be any function that takes two arguments such that  $k(x, x')$  generates a positive definitive covariance matrix  $k$  (Rasmussen and Williams, 2006). An example of a widely-used covariance function adopted in modelling correlated noise in light-curves (e.g., Gibson et al., 2012; Gibson, 2014; Chen et al., 2020) is the squared-exponential kernel given by

$$k(x, x') = A^2 \exp\left(-\frac{|x - x'|^2}{2l^2}\right), \quad (2.4)$$

where  $A$  and  $l$  are the hyperparameters that describe the amplitude and length-scale of the kernel. It shows that for two input points  $x$  and  $x'$ , the covariance is around unity when the input points are close and decreases exponentially as the distance between the inputs increase.

New covariance functions can be built from a sum or product of different kernels. The output of a GP is a normal distribution expressed in terms of the mean and variance where the mean corresponds to the most likely output that explains the variability in the data. The GP package `celerite` (Foreman-Mackey et al., 2017) provides a quick, efficient and scalable modeling of variability and contains several kernels such as the Matern-3/2 and Simple Harmonic Oscillator (SHO) kernels that have been used to model stellar trends and instrumental systematics in light-curves (e.g. Barros et al. 2020; Jenkins et al. 2020;

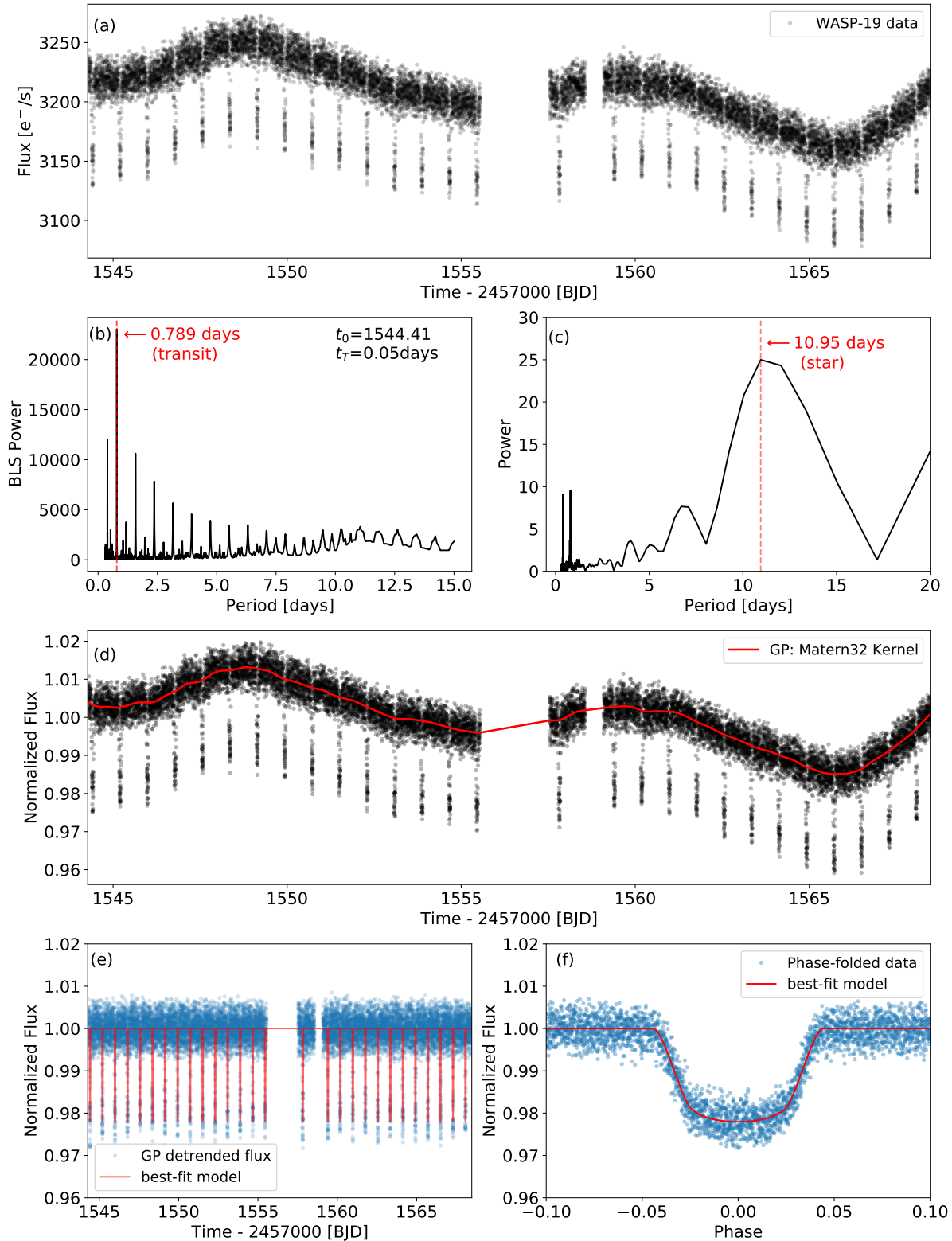


Figure 2.3: Analysis of the WASP-19 light-curve. **(a)**: The SAP light-curve after decontamination and outlier removal. **(b)**: BLS periodogram showing the period of maximum power corresponding to the orbital period of the planet WASP-19b. **(c)**: LS periodogram showing the period of stellar variability. **(d)**: Detrending of the normalised light-curve using a Matern-32 GP kernel. **(e)**: The GP detrended light-curve and over-plotted best-fit transit model. **(f)**: Phase-folded light-curve and best-fit transit model.

Bonfanti et al. 2021).

As an example, Fig. 2.3d shows the mean of a GP model with Matern-3/2 kernel used to model the stellar variability in the WASP-19 data. It can be seen to provide a very good fit to the trends without affecting the in-transit points since they were masked. The full light-curve data is then divided by the mean of the GP model to obtain the detrended light-curve shown in Fig. 2.3e. Note that it is common to fit the GP alongside the transit model or inflate the uncertainties of the observed flux by the standard deviation of the GP model in order to propagate the GP model uncertainties to the transit parameters.

### Polynomial fit

For most analyses of the transits in a light-curve, the data points far from transits are not important to adequately estimate the planet’s transit parameters. Therefore, one can define a baseline region around each transit, say 2 transit durations on either side of the mid-transit, which can be fitted with a low-order polynomial while ignoring the point within transit (around 0.6 transit durations around  $t_0$ ). The data points in this region including the transit points are then divided by the best-fit polynomial. In practice, selecting the appropriate polynomial order requires one to compute some goodness-of-fit statistic to ensure that the baseline flux is not overfitted. The pitfall of higher order polynomials is that they tend to overfit the gap (where in-transit points were masked) which affects the transit depth. This can be mitigated by fitting the polynomial and transit simultaneously. This light-curve detrending method is relatively simple, has been applied severally in the literature (e.g, Holczer et al., 2016) and is used in the `exotrending` Python package (Barragán and Gandolfi, 2017).

### Filtering

Filtering involves selecting a contiguous subset of the data, based on number of points or timespan, and applying some statistic or function on them for the purpose of smoothing the data. Some common filtering methods include Savitzky-Golay (SG) filtering, mean and median filtering among others. SG filtering (Savitzky and Golay, 1964) is a method of cadence-based filtering where smoothing is achieved by dividing successive subsets of the data, containing a defined number of points, by the best-fit low-order polynomial. This has the effect of removing the long-term trend in the data. SG filter is the default method for detrending in the `LightKurve` package. Similar filtering can also be achieved by computing the sliding mean or median of the subsets. These filtering methods and

others are implemented in the `Scipy` Python suite (Virtanen et al., 2020).

## 2.2 Transit Analysis

The standard transit model depends on a set of parameters  $\theta$  and the time  $t$  of flux measurements. The typical parameters for the transit of a planet in a circular orbit ( $e = 0$ ) are given by:

$$\theta = \{R_p/R_*, a/R_*, b, t_0, P\} \quad (2.5)$$

which accurately captures the depth, duration and shape of the transit. The number of parameters of the transit model will be increased by the inclusion of additional features that affect the transit light-curve. For instance, modelling limb darkening using the quadratic law from Eq. 1.11 will introduce two extra parameters ( $u_1$  and  $u_2$ ) to the transit model, whereas using the linear law from Eq. 1.10 will add only one more parameter. Similarly, including the effects of rings, oblateness or tidal deformation will also add new parameters to the standard model.

The parametric transit model can be used to fit observed transit data to determine the parameters. Typically, the fitting procedure returns the optimal set of model parameters  $\theta$  that minimises the sum-of-square statistic,  $\chi^2$ , given as:

$$\chi^2 = \sum_{i=1}^N \frac{[F_i^{\text{obs}} - F_i^{\text{model}}(\theta)]^2}{\sigma_i^2} \quad (2.6)$$

where  $F_i^{\text{obs}}$  is the observed flux at time  $t_i$  with uncertainties  $\sigma_i$ . A transit tool like `Batman` (Kreidberg, 2015) is used to calculate the model flux  $F_i^{\text{model}}(\theta)$  which depends on the parameters  $\theta$ . The optimal set of parameters is referred to as the maximum likelihood estimate (MLE) since minimising  $\chi^2$  is equivalent to maximising the likelihood that these parameters generate a transit model that best fits the observed data. Several minimisation algorithms are available (e.g in `Scipy` optimisation library) for finding the minimum  $\chi^2$  (MLE) given an initial guess of the parameters. However, it is possible for the algorithm to get stuck in a local minimum depending on the initial guess values. This problem can be mitigated using global optimisation algorithms such as Basin-Hopping, Simulated Annealing or Differential Evolution (e.g. Xiang et al. 1997; Storn and Price 1997; Olson et al. 2012) which do not depend on initial values. For instance, the Differential Evolution (DE) algorithm (implemented in `Scipy`) can be very fast and efficient for finding the global minimum even though it requires more function evaluations than

gradient-based minimisation methods.

Fitting a transit model, with the parameters in Eq. 2.5 and quadratic limb darkening law, to the detrended WASP-19 light-curve gives the MLE of the parameters. The best-fit values of  $P$  and  $t_0$  are similar to those obtained from the BLS fit. The best-fit transit model is overplotted on the detrended data shown in Fig. 2.3e and also on the phase-folded data in Fig. 2.3f. It is however common to apply a Bayesian statistical approach to parameter estimation which give robust uncertainties on the model parameters.

### 2.2.1 Bayesian Inference

The Bayesian approach for performing statistical inference involves using probabilities to make statements about unobserved quantities based on observed data. It assigns probabilities to hypotheses and provides a self-consistent method of combining observed data with prior information to obtain a posterior probability distribution. When new data is observed, it allows to update the prior knowledge using the posterior obtained from previous data. It also allows for robust modelling of observational uncertainties. Bayesian inference finds application in problems relating to (1) *parameter estimation* where the aim is to infer the joint posterior distribution of the parameters of a model given prior information and observed data, and (2) *model comparison* where the aim is to find out which model best explains the observed data out a set of competing models.

Bayesian inference is based on Bayes' theorem given by:

$$\overbrace{P(\theta|D, M)}^{\text{posterior}} = \frac{\overbrace{P(D|\theta, M)}^{\text{likelihood}} \cdot \overbrace{P(\theta|M)}^{\text{prior}}}{\underbrace{P(D|M)}_{\text{evidence}}} = \frac{\mathcal{L}(\theta) \cdot \pi(\theta)}{\mathcal{Z}} \quad (2.7)$$

where the *posterior* is the joint probability distribution of a model,  $M$ , with parameters,  $\theta$ , given the observed data,  $D$ . It combines information from the *prior distribution* of the parameters with the *likelihood* of observed data given the model parameters and normalises it by the *evidence*. These probabilities are briefly described below

#### Priors

Prior distributions encode our present knowledge or assumption about the parameters of the model such as their physical range or distribution based on previous estimates or

observation. It is necessary to define a prior distribution for all parameters in the model which can be informative or weakly informative (uninformative), depending on how much knowledge we have on the parameter. The most commonly used priors are the *uniform* and *normal* priors.

A *uniform* prior is an example of a weakly informative or uninformative prior which encodes our ignorance about a parameter. It minimises the effect that a prior has on the posterior and can be used when only the possible range of a parameter is known. For example, we know that the impact parameter of a non-grazing transit ranges between 0 and 1. The uniform prior for a parameter  $\theta_i$  that lies between  $a$  and  $b$  with equal probability is given by

$$\mathcal{U}(a, b) = \begin{cases} (b - a)^{-1} & : a < \theta_i < b \\ 0 & : \text{otherwise.} \end{cases} \quad (2.8)$$

A *normal* (or *Gaussian*) prior is a good example of an informative prior. It is used when there is a measurement of a parameter with mean and  $1\sigma$  estimates based on previous observation/experiment. This can be the case, where the density of the host star is obtained from asteroseismology and its estimate is combined with the orbital period of the planet through Eq. 1.8 to set a normal prior on the scaled semi-major axis. The normal prior of a parameter  $\theta_i$  with mean  $\mu$  and standard deviation (width)  $\sigma$  is given by

$$\mathcal{N}(\mu, \sigma) = \frac{1}{\sqrt{2\pi\sigma^2}} \exp\left(-\frac{(\mu - \theta_i)^2}{2\sigma^2}\right) \quad (2.9)$$

The particular choice of prior can impact the posterior distribution. For instance, a uniform prior may truncate or even exclude the maximum of the likelihood, whereas a normal prior might have a width that is too constraining on an inaccurate mean. When defining an informative prior from several competing previous estimates, a prior that encompasses all estimates is preferred (Parviainen, 2018). It is also advisable to perform a sensitivity analysis to understand how strongly the results are influenced by the adopted priors, particularly when performing model comparison. In some cases, informative priors can be constructed by parameterising the observed distributions of a parameter e.g. the observed radius distribution of exoplanets in a certain mass range or the eccentricity



distribution of exoplanets (Kipping, 2013b).

### Likelihood

The likelihood is the probability of the observed data  $D$  given a model  $M$  with parameters  $\theta$ . For a particular set of parameters, the joint likelihood of the data of length  $N$  is a product of the independent likelihood of each data point  $P(D_i|\theta, M)$  so that

$$P(D|\theta, M) = \prod_i^N P(D_i|\theta, M). \quad (2.10)$$

For normally distributed data with uncorrelated noise of standard deviation  $\sigma$ , the individual likelihood of the data points is a Gaussian so that Eq. 2.10 can be written as product of  $N$  Gaussians

$$\mathcal{L}(\theta) = P(D|\theta, M) = \prod_i^N \left( \frac{1}{\sqrt{2\pi\sigma_i^2}} \right) \exp\left(-\frac{1}{2}\chi^2\right) \quad (2.11)$$

where  $\chi^2$  is given in Eq. 2.6. To account for possible underestimation of the flux uncertainties  $\sigma_i$ , a jitter term  $\sigma_j$  can be added such that the variance  $\sigma_i^2$  in Eqs. 2.6 and 2.11 is replaced by  $\sigma_i^2 + \sigma_j^2$ . In practice, there usually exists some correlated noise in the data and as such the likelihood has to be modified to model the correlated noise as a stochastic process e.g. using Gaussian Processes or wavelet analysis; (Carter and Winn, 2009; Cubillos et al., 2016; Parviainen, 2018).

### Posterior

The posterior is the probability that the model  $M$  with parameters  $\theta$  is true given the data. As the evidence is just a normalising factor, Eq. 2.7 can be rewritten as

$$P(\theta|D, M) \propto \mathcal{L}(\theta) \cdot \pi(\theta). \quad (2.12)$$

representing a combination of our knowledge before observing the data (prior) and what is learned from the data (likelihood). For parameter estimation, we aim to obtain a joint posterior distribution for the parameters of the model. The marginal posterior distribution for each parameter is obtained by integrating the joint posterior  $\mathcal{L}(\theta) \cdot \pi(\theta)$  over all other parameters to infer the model parameters.

Calculating the marginal posterior distribution is usually done by random sampling

(Markov Chains) in order to approximate the posterior. A Markov Chain Monte Carlo (MCMC) sampler generates a large number of random samples from the full parameter space of  $\theta$  with a probability density that is proportional to the posterior distribution (Cubillos et al., 2016). The sampler starts a chain from a point  $\theta^{(j)}$  (one complete set of model parameters) in the parameter space and computes the posterior probability of this point. It then proposes a jump to another point  $\theta^{(j+1)}$  and accepts the new point based on the posterior probability ratio,  $\alpha$ , between the current and proposed points. If  $\alpha > 1$ , the point is accepted and added to the chain whereas if  $\alpha < 1$ , the point is accepted with probability  $\alpha$ . The sampling continues by proposing a new point in the parameter space.

The dependence of the previous point implies that consecutive samples in the MCMC are not always independent of each other and the starting point can impact the evolution of the chains. Therefore, MCMC typically requires a large number of iterations. The influence of the starting point and the correlation between samples can be mitigated by excluding the initial samples (a few percent of the total chain length), and then keeping only every  $n^{\text{th}}$  samples in a process called thinning. To infer the model parameters from an MCMC, the chains need to have converged. The Gelman-Rubin statistic (Gelman and Rubin, 1992) is a widely-used convergence test that ensures that different chains within the MCMC are similar to each other. Calculating the autocorrelation length is also a convergence diagnostic indicating the required number of iterations necessary to have independent samples and the value of  $n$  to use in thinning the chains (Foreman-Mackey et al., 2013).

The marginal posterior distribution or credible interval (CI) of each parameter can be described by a summary statistic. Usually, the median of the distribution and the 68% CI are reported as the best-estimate and uncertainty of the parameters.

The `emcee` python package (Foreman-Mackey et al., 2013) based on the Goodman and Weare (2010) Affine-Invariant MCMC ensemble sampler is used in parts of this thesis and offers fast and efficient parameter estimation.

## Evidence

The evidence, also called the marginal likelihood, is regarded as a normalisation constant that ensures that the posterior probability (Eq. 2.7) integrates to unity. Although it is usually not computed when performing parameter estimation, it is a necessary component for comparing models. The evidence is the probability of the observed data given the

model and is computed as the integral of the likelihood and prior distribution over the entire parameter space as

$$\mathcal{Z} = P(D|M) = \int \mathcal{L}(\theta) \cdot \pi(\theta) d\theta. \quad (2.13)$$

It does not depend on the value of the individual parameters but on the size of the parameter space and the enclosed likelihood. As such, the evidence is very sensitive to the choice of adopted priors. Its value is larger for a model where more of parameter space have high likelihood and is smaller for a model with significant low-likelihood regions. For this reason, it plays an import role in model comparison and penalises models with wasted parameter space - a simple model with a compact parameter space will have a larger  $\mathcal{Z}$  than a more complicated one unless the complexity is justified by the data.

Given data  $D$  and two competing models,  $M_1$  and  $M_2$ , the posterior probabilities of the models can be compared from Bayes' theorem as

$$\frac{P(M_1|D)}{P(M_2|D)} = \frac{P(M_1)}{P(M_2)} \cdot \frac{\mathcal{Z}_1}{\mathcal{Z}_2}, \quad (2.14)$$

where  $P(M_1)$  and  $P(M_2)$  are the prior probabilities. When both models have equal prior probabilities, then the ratio of the posterior probabilities is equal to the ratio of evidences called the Bayes factor given as

$$\mathcal{B}_{12} = \frac{\mathcal{Z}_1}{\mathcal{Z}_2} = \exp(\log \mathcal{Z}_1 - \log \mathcal{Z}_2). \quad (2.15)$$

Therefore, model comparison can be done by obtaining the evidence of the competing models and calculating  $\mathcal{B}_{12}$ . The value of  $\mathcal{B}_{12}$  expresses the degree to which the data supports  $M_1$  over  $M_2$ . Kass and Raftery (1995) provided simplified guideline for interpreting the Bayes' factor which has been extended in Table 2.1 to show the cases when the evidence for  $M_2$  is stronger than that of  $M_1$  (Lee and Wagenmakers, 2013). For example,  $\mathcal{B}_{12} = 5$  would imply that  $M_1$  is 5 times more likely to have produced the observed data and constitutes a moderate evidence for  $M_1$ . The inverse is the case for  $\mathcal{B}_{12} = 1/5$  where  $M_2$  is 5 times more likely. So we have that  $\mathcal{B}_{21} = 1/\mathcal{B}_{12}$ .

Obtaining evidence for a model involves computing the evidence integral in Eq. 2.13 which is more challenging than computing the posteriors. As such, specialized numerical methods are used in calculating it. One of such methods is called Nested sampling (Skilling, 2004, 2006) which calculates the evidence by integrating the prior within nested

Table 2.1: Evidence categories for the Bayes factor following the label structure of Kass and Raftery (1995) and Lee and Wagenmakers (2013).

$\mathcal{B}_{12}$	Interpretation
>150	Extreme evidence for model 1
20 to 150	Very strong evidence for model 1
3 to 20	Moderate evidence for model 1
1 to 3	Anecdotal evidence for model 1
1	no evidence for either model
1/3 to 1	Anecdotal evidence for model 2
1/20 to 1/3	Moderate evidence for model 2
1/150 to 1/20	Very strong evidence for model 2
<1/150	Extreme evidence for model 2

contours of constant likelihood. It additionally generates posterior samples and is capable of sampling complex multi-modal distributions.

The `dynesty` python package (Speagle, 2019) based on the nested sampling algorithm is used in parts of this thesis to estimate the Bayesian evidence and perform model comparison.

## 2.3 Probing features in transit light-curves

### 2.3.1 The observable signature of features in transit light-curves

The presence of an astrophysical feature, not accounted for in the standard transit model, can affect the observed transit light-curve by modifying the duration, depth or shape of the expected transit, or introducing an asymmetry. Identifying the signature of a feature involves separating the observable contribution of that feature from the standard transit model. Ideally, the signature of a feature should be the difference between the transit light-curve that includes the feature and that without the said feature. However, when analysing light-curve observations, the parameters of the transit are not known a priori but are determined from fitting *a model* to the data. Therefore, the induced signature of the feature is the residual obtained from fitting the transit observation with a model without the feature included (Barnes and Fortney, 2003). This can be well-illustrated with a *toy problem*.

### Toy problem

Let's set up a simple *toy problem* where limb darkening (LD) is considered as an additional feature to the standard transit model. The aim is to identify the signature of limb darkening in a light-curve. Through simulations, we can identify the transit signature of limb-darkening in order to characterise its form, amplitude and localisation in the light-curve. For this, the `Batman` transit tool was used to simulate the transit light-curve of a Jupiter-sized planet with a 10 day period around a Sun-like star. The fiducial parameters of the planet are listed in Table 2.2. The simulation assumes observations with 30 secs cadence which are made with the *Spitzer* space telescope at the  $4.5 \mu\text{m}$  passband. This setup was selected to make the identification of the limb darkening feature more challenging. The impact of limb darkening is reduced at this wavelength, leading to a flatter transit bottom that is similar to a case without limb darkening. The limb darkening feature is included by considering the simplest limb darkening law (linear: Eq. 1.10) which has the linear coefficient ( $u$ ) as its only parameter. The value for  $u$  used in the simulation is derived for this passband from the `LDTk python` package (Parviainen and Aigrain, 2015). We then fit the simulated light-curve with a transit model that does not account for limb darkening (non-LD model). The fitted parameters are the same given in Eq. 2.5 (except for  $P$  which is fixed) whose maximum likelihood estimates are obtained by minimising  $\chi^2$  (Eq. 2.6) with the Differential Evolution algorithm.

Table 2.2 shows the maximum likelihood estimate from the fit. We see that, even in this long wavelength band, not accounting for the effect of limb darkening in the light-curve fit leads to systematic errors in the estimation of other transit parameters as the non-LD model attempts to mimic the simulated LD transit by modifying its parameters. A larger  $R_p$  is obtained in order to match the deeper transit of the LD transit. Whereas,  $b$  and  $a/R_*$  are modified in attempt to maintain the original transit duration and shape despite the larger  $R_p$ . Figure 2.4 shows the fit residuals (simulated – non-LD fit) which has an amplitude of 367 ppm and represents the observable induced signature of limb darkening in the simulated light-curve. We observe, as expected, that the effect of limb darkening is mostly concentrated around the ingress and egress phases since the intensity at the limb differs the most from the averaged intensity of the star. Due to the larger  $R_p$  in the non-LD fit, the transit is longer and thus begins earlier, which causes the initial positive turn in the residuals. The largest difference between both signals occurs immediately after ingress (second contact) when the full disk of the simulated planet blocks a low-intensity (limb-darkened) region of the star whereas the non-LD fit planet blocks a higher stellar intensity in the same region. As the planets in both cases approach mid-

transit, the simulated planet blocks regions with higher stellar intensity than the non-LD fit planet and a negative residual is obtained. This pattern is repeated in reverse as the planets approach egress since the light-curve is symmetric. The same exercise done using a longer cadence of 15 mins instead of 30secs leads to a lower amplitude LD signature of 186 ppm. This shows the importance of adequate time sampling in identifying or detecting features in transit light-curves.

Table 2.2: Fiducial transit parameters adopted in the toy problem and the result from fitting with a non-LD transit model.

Parameter	Values	MLE
$R_p [R_*$	0.1	0.1005
$b$	0.5	0.547
$a/R_*$	19.542	19.023
$t_0$	0	$1 e^{-8}$
$u$	0.1201	–

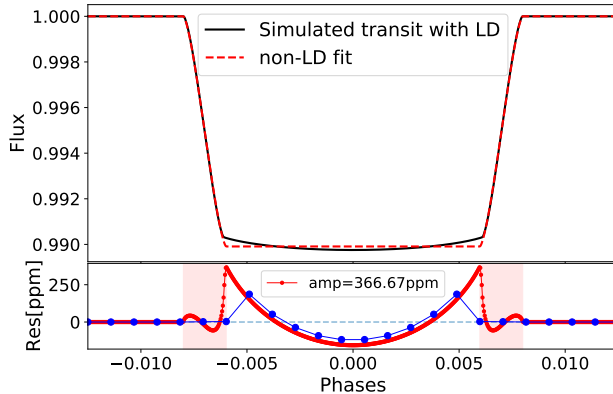


Figure 2.4: Top: Simulated limb darkened transit of the fiducial planet (black) and the model fit without limb darkening (red). Bottom: The residuals (simulated – fit) of amplitude (amp). The blue curve shows the lower amplitude residual for a fit to simulation with 15 mins cadence while the shaded regions indicate the ingress and egress phases.

### 2.3.2 Detecting features from light-curve analysis

In order to detect a feature in the light-curve, it is necessary to compare the model without the feature to that with the feature to estimate which one explains the data better. This problem is well-suited to the Bayesian Model comparison discussed in §2.2.1.

Let’s expand the toy problem with a different aim of determining if a transit observation includes the limb darkening feature or not. This might not be as clear-cut since the level of noise in the data might be many times higher than the amplitude of the feature to be detected. To do this, we take the same simulated LD transit of the toy problem and add Gaussian noise with a level of 2 times the amplitude of the LD feature ( $2 \times 367$  ppm). We then fit the a LD model ( $M_1$ ) and a non-LD model ( $M_2$ ) to the sim-

ulated observation using `dynesty` in order to obtain the evidence of the models and the posterior of the parameters. Note that  $M_2$  is nested within  $M_1$  since for  $u = 0$  in  $M_1$ ,  $M_1$  reduces to  $M_2$ . Therefore, to detect the limb darkening feature, a non-zero value of  $u$  has to be obtained with statistical significance in  $M_1$  and the Bayesian evidence of  $M_1$  should be higher than for  $M_2$ . A uniform prior is adopted on the parameters in both models including  $u$  since there is no prior knowledge of it except that it is in the range  $[0, 1]$ .

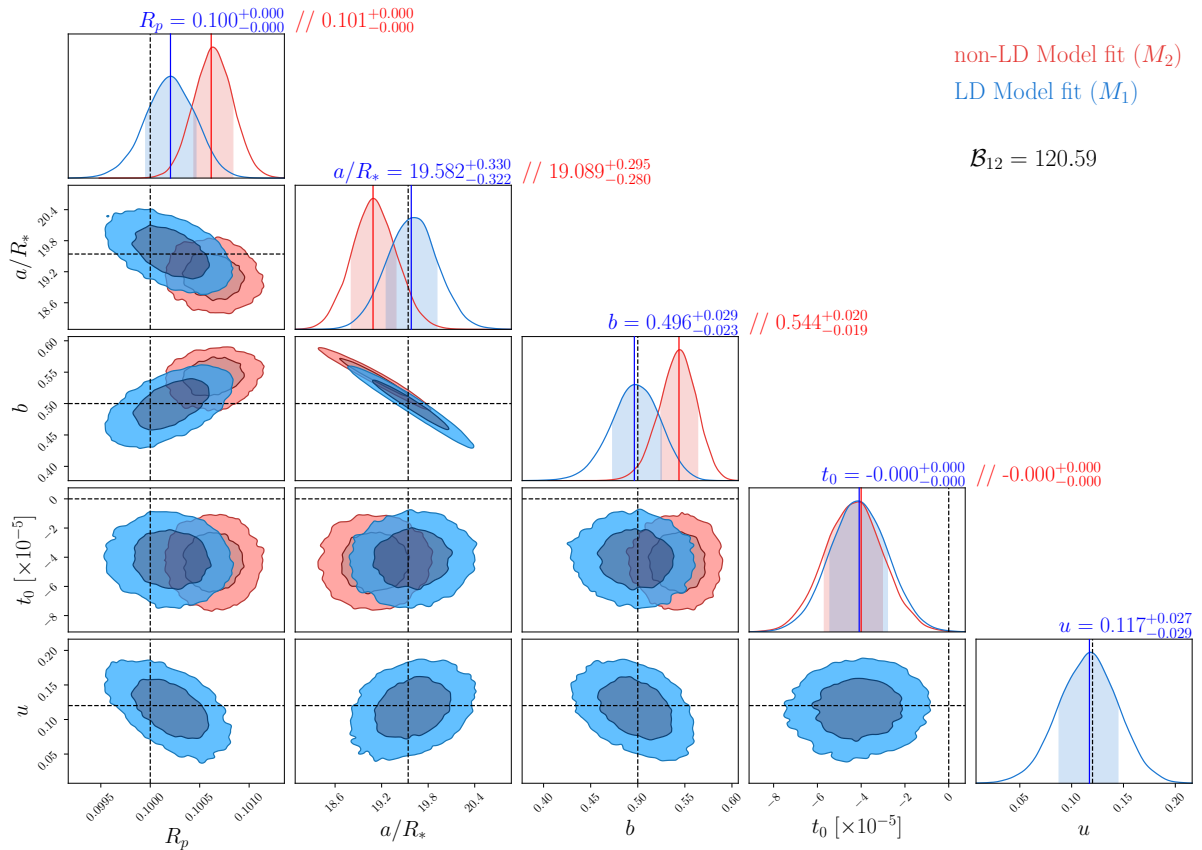
The adopted priors of the parameters and the median of the posterior from both fits are reported in Table 2.3 while the posterior distributions are shown in Fig. 2.5. Notice how in Fig. 2.5, the median values of the non-LD model fit differ more from the simulated values (vertical dashed lines) than the LD model fit, its values are adjusted such that it mimics the simulated light-curve. Also, the non-LD fit parameters are more precise than those from the LD fit since the uncertainty of the limb darkening parameter in the LD model is propagated to the rest of the parameters. More importantly, comparing the log evidences using Eq. 2.15 results in a Bayes' factor of  $\mathcal{B}_{12} = 120.59$ . This implies a very strong evidence for the LD model ( $M_1$ ) despite the fact that both transit models seem to be well-below the scatter of the simulated observation in Fig. 2.6 and the residuals from both fit are just slightly different. The high value of  $\mathcal{B}_{12}$  implies that the addition of the limb darkening parameter is justified by the data. Furthermore, a value of  $u = 0.117 \pm 0.029$  is obtained for LD model fit indicating a  $4\sigma$  detection of the limb darkening feature.

Performing the same exercise but with a noise level of 3 times the LD feature amplitude ( $3 \times 367$  ppm) gives a reduced  $\mathcal{B}_{12} = 2.68$  which is an anecdotal evidence in favor of  $M_1$ . The detection significance of  $u$  also reduces to  $2.5\sigma$ . In general, as the noise level in the data increases compared to the amplitude of the feature to be detected, the detectability of the feature reduces until there's only comparable evidence between both models or the simpler model without the feature becomes preferred.

As will be seen in the following chapters, the typical photometric noise level is usually high compared to the subtle features we are trying to detect. As such several transit observations are required to lower the noise level. Even so, some of the best-case scenarios will be an anecdotal/moderate evidence for the sought-after feature.

Table 2.3: Priors of parameters of the toy model and result of model comparison for a model without limb darkening (non-LD model) and a model with limb darkening (LD model).

Parameter	Values	Priors	LD model ( $M_1$ )	non-LD model ( $M_2$ )
$R_p [R_*$	0.1	$\mathcal{U}(0.05, 0.15)$	$0.1001 \pm 2.5e^{-4}$	$0.1006 \pm 1.7e^{-4}$
$b$	0.5	$\mathcal{U}(0, 1)$	$0.496^{+0.029}_{-0.023}$	$0.544^{+0.020}_{-0.019}$
$a/R_*$	19.542	$\mathcal{U}(14, 25)$	$19.582^{+0.330}_{-0.322}$	$19.089^{+0.295}_{-0.280}$
$t_0$	0	$\mathcal{U}(-1e^{-3}, 1e^{-3})$	$-4e^{-5} \pm 1.3e^{-5}$	$-4e^{-5} \pm 1.7e^{-5}$
$u$	0.1201	$\mathcal{U}(0, 1)$	$0.117^{+0.027}_{-0.029}$	–
rms [ppm]	–	–	708.95	716.01
$\log \mathcal{Z}$	–	–	4841.470	4836.6770


 Figure 2.5: Posterior distribution of parameters of the LD and non-LD models. The Bayes factor,  $\mathcal{B}_{12}$  is also shown. The values on the histograms show the median and 68% credible interval of the posteriors for both models while the black vertical lines indicate the original simulated value for each parameter.



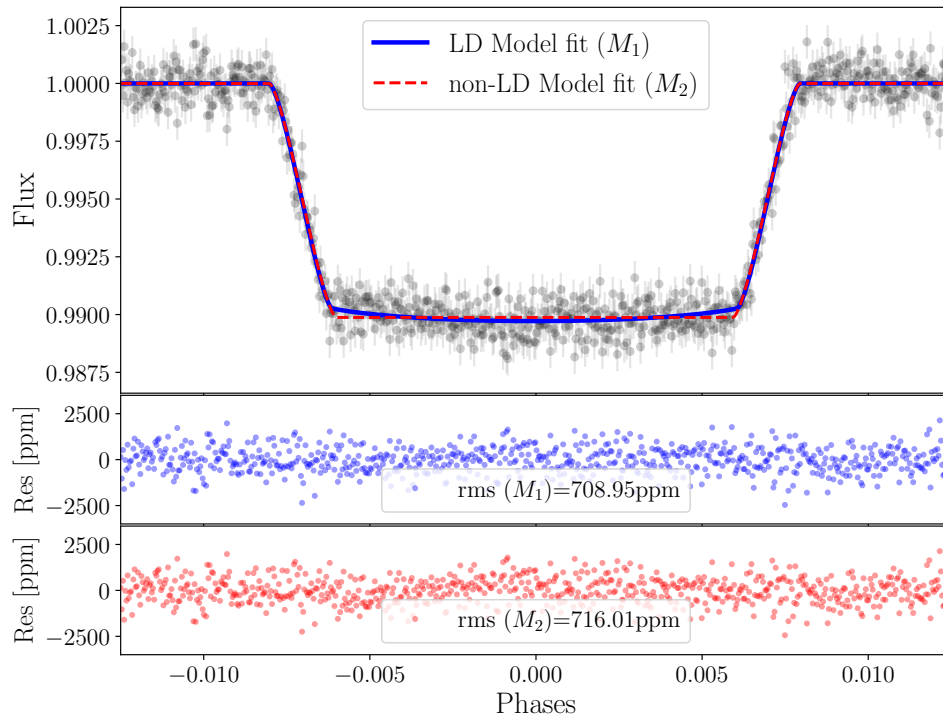


Figure 2.6: Fit of LD model (blue) and non-LD model (red) to simulated limb-darkened transit in the *toy problem*. The residuals from both fits and their root-mean-square value (rms) are also shown.

# Chapter 3

## Exoplanetary Rings

*“I have observed the highest planet [Saturn] to be tripled-bodied. This is to say that to my very great amazement Saturn was seen to me to be not a single star, but three together, which almost touch each other.”*

---

— Galileo Galilei, 1610

Planetary rings were first observed when Galileo pointed his telescope to Saturn in 1610, even though they were falsely interpreted at the time as “handles” or large moons. They were, of course, later better described as a thin ring around the planet. Further observations revealed that Saturn, in fact, has a ring system separated by gaps and composed of numerous tiny particles. Rings have since been a fascinating subject of scientific inquiry and were subsequently discovered around several objects within the Solar-system, popularly around the giant planets but recently also around smaller rocky bodies (Braga-Ribas et al., [2014](#); Ortiz et al., [2015](#), [2017](#)).

The properties of rings vary widely between planets and even within the ring system of a planet. Saturn has the most extensive and dense rings which are bright due to their icy composition, while the rings of Uranus and Neptune are narrow, dark and separated by large gaps, and those of Jupiter are faint and composed of dusty particles. With the prevalence of rings around the solar system, they are expected to also exist around exoplanets.

This chapter investigates the detection and characterisation of planetary rings, particularly Saturn-like, around exoplanets (exorings). I start with the motivation to detect

exorings and then present the tool used in modelling the transit signals of ringed planets. Afterwards, I show some of the effects of rings to transit signals and their derived parameters. Although the work presented in this chapter is mostly on transit light-curves, I briefly touch on the ring signature in RM signals. Finally, I conclude with the analysis of a possible case of exorings.

## 3.1 Motivation

The presence of several ringed objects within the Solar-system has motivated the search for these exquisite features around exoplanets. Despite their ubiquity in the Solar System, there still exists several lingering questions about rings such as: their origins and formation mechanisms, evolution, compositions, and ages amongst others (Charnoz et al., 2018a,b). The lifespan of rings are also not clear; are they long-lived or is it just serendipitous that we are able to observe so many ringed objects in our Solar System at this present time. Detecting additional ringed objects can help unlock some of these mysteries (and most certainly introduce new ones) by improving our knowledge about rings and their diversities. Even the long-held idea that rings are exclusive features of giant planets was recently dismissed by the detection of rings around the Centaurs Chariklo and Chiron (Braga-Ribas et al., 2014; Ortiz et al., 2015), and the dwarf planet Haumea (Ortiz et al., 2017).

The detection of exorings (or their absence) would help understand the prevalence of rings around planets and know if ringed planets can exist within the snowline (where most of the detected exoplanets orbit and silicate rings have been shown to be theoretically possible; Schlichting and Chang 2011). Exorings can also provide valuable insight into the origin and formation of rings: if they formed alongside their planets or later as the planets evolve. With several detected exorings, it becomes possible to probe the lifespan of rings based on their occurrence around stars of different ages. Furthermore, exorings could inform migration scenarios of a planet as their presence can imply little or no migration. If a ringed planet with silicate rings is found within the snow line, then its more likely that it didn't migrate from further out in the system where there is limited amount of refractory materials. Moreover, as rings have been observed to co-evolve with moons, detecting rings can reveal the presence or formation of exomoons.

Despite the large number of discovered exoplanets, exorings are yet to be discovered. Several techniques have been proposed to identify and characterise their signatures from

transit light-curves, RM signals, and reflected light signals (e.g. Barnes and Fortney 2004; Ohta et al. 2009; Mooij et al. 2017; Santos et al. 2015; Sucerquia et al. 2020; Arkhypov et al. 2021).

The transit method is very useful in searching for rings as their presence can modify the observed light-curve and RM signal, causing a number of potentially detectable effects (see e.g. Barnes and Fortney, 2004; Tusnski and Valio, 2011; Akinsanmi et al., 2018). These works show that high precision observations and time sampling are required to detect Saturn-like rings around exoplanets. Several searches for transiting ringed planets have been performed and in some cases possible ringed candidates have been identified or limits placed on ring parameters (e.g., Heising et al. 2015; Aizawa et al. 2017, 2018). An interesting case of a transiting ring-like structure spanning 0.6 Astronomical Units (AU) was found around an unidentified stellar companion J1407 b (Kenworthy and Mamajek, 2015). However, the nature or orbit of the companion cannot be ascertained.

## 3.2 Properties of planetary rings

There are a number of ring, planet and orbital considerations that ensure the long-term stability and survival of rings around a planet. I review some important ones here that are useful in constraining the presence of rings around exoplanets.

### 3.2.1 Ring stability and composition

**Hill Radius:** For a satellite to orbit a planet, its distance from the planet must be such that the gravitational influence of the planet dominates over external forces from the host star. This is referred to as the Hill radius,  $R_{\text{Hill}}$ , of the planet and it is given for an eccentric orbit (e.g., Hamilton and Burns, 1992) as

$$R_{\text{Hill}} = a(1 - e) \left( \frac{M_p}{3M_*} \right)^{1/3} = R_p(1 - e) \left( \frac{GP^2\rho_p}{9\pi} \right)^{1/3}, \quad (3.1)$$

where  $\rho_p$  is the density of the planet. For Saturn with  $\rho_p = 0.687 \text{ g cm}^{-3}$ ,  $P = 29.46 \text{ yrs}$  and  $e=0.0565$ , we obtain  $R_{\text{Hill}} = 1056 R_p$ . At  $R_{\text{Hill}}$ , the tidal forces from the host star and the gravitational force of the planet are in equilibrium. Therefore, beyond  $R_{\text{Hill}}$  a companion body becomes gravitationally unbound to the planet.

**Roche Radius:** This is the distance from of a body where its tidal forces overcomes the self-gravity of an orbiting companion leading to deformation and eventual break-up of the companion. Rings would therefore be expected to form within the Roche radius of a planet. For ring particles of density  $\rho_r$  orbiting a planet, the Roche radius  $R_{\text{Roche}}$  is given (e.g., Pater and Lissauer, 2015) as

$$R_{\text{Roche}} = 2.46 R_p \left( \frac{\rho_p}{\rho_r} \right)^{1/3}. \quad (3.2)$$

The main rings in the Solar system are all within the  $R_{\text{Roche}}$  of their respective hosts. Considering  $\rho_r = 1 \text{ g cm}^{-3}$  for the icy particles that make up Saturn’s rings, we obtain  $R_{\text{Roche}} = 2.2 R_p$  for Saturn. Beyond  $R_{\text{Roche}}$ , ring materials are unstable and need to be constantly replenished otherwise they coalesce to form satellites or are removed from the system (Charnoz et al., 2018b).

The long-term stability of rings around a planet can be assessed by calculating  $R_{\text{Hill}}$  and  $R_{\text{Roche}}$ . At long distances from the star,  $R_{\text{Roche}}$  is typically far less than  $R_{\text{Hill}}$  (see computed values for Saturn above). This is required for stable rings as the planet’s gravitational influence at the outer regions of the Hill sphere ( $\gtrsim 2/3 R_{\text{Hill}}$ ) are unstable due to the strong competition with the stellar tides and orbital perturbations (Hamilton and Burns, 1991; Winter and Neto, 2001). Therefore, the radial extent of any stable ring around a planet has to be within  $R_{\text{Roche}}$  and  $R_{\text{Roche}} < 2/3 R_{\text{Hill}}$ . This condition might not hold for some close-in exoplanets since  $R_{\text{Hill}}$  decreases closer to the star and one can have  $R_{\text{Roche}} \simeq R_{\text{Hill}}$ . In such a case, the exoplanet cannot hold stable rings.

We see from Eq. 3.1 that  $R_{\text{Hill}}$  is smaller for planets on eccentric orbits, which can bring the planet closer to the star along the orbit, implying that rings can be become unstable ( $R_{\text{Roche}} \simeq R_{\text{Hill}}$ ). Rings are therefore more favoured around planets on circular orbits than eccentric orbits. Indeed the eccentricities of the Solar-System ringed planets are below 0.06.

We also see in Eq. 3.2 that  $R_{\text{Roche}}$  depends on the density of the ring materials. Denser ring materials will have smaller  $R_{\text{Roche}}$  and will be tightly packed around the planet. This means that, if we are able to estimate the radial extent of the ring from transit, and assume it is at the Roche radius, we can get an estimate of the density of the ring materials  $\rho_r$ . Once  $\rho_r$  is obtained, the equilibrium temperature  $T_{\text{eq}}$  of the planet can be calculated to assess if rings of such density can exist around the planet.  $T_{\text{eq}}$  is given by (e.g., Perryman, 2018)

$$T_{\text{eq}} = T_* \sqrt{\frac{1}{2 a/R_*}} (1 - A_B)^{1/4}, \quad (3.3)$$

where  $A_B$  is the bond albedo of the planet and  $T_*$  is the effective temperature of the star. Saturn has  $T_{\text{eq}} = 90$  K which allows for icy rings since the value is below the sublimation temperature of water ice (170 K). Planets closer to their host stars and with high equilibrium temperatures, will require rings with higher densities that can withstand the high temperature.

### 3.2.2 Ring orientation

The rings around a planet lie on a plane that depends on the balance between the planet's centrifugal force and stellar tide which varies with the distance of the rings from the planet (Tremaine et al., 2009). The distance from the planet where these forces balance out is defined as the Laplace radius  $R_L$  given by (Schlichting and Chang, 2011)

$$R_L^5 = 2 J_2 R_p^2 a^3 (1 - e)^{3/2} \frac{M_p}{M_*}. \quad (3.4)$$

Within  $R_L$ , rings settle in the planet's equatorial plane while beyond  $R_L$  they settle in the orbital plane. Since rings spread out until  $R_{\text{Roche}}$ , we can determine the plane of the rings by taking the ratio of  $R_L$  and  $R_{\text{Roche}}$  given by (Schlichting and Chang, 2011)

$$\frac{R_L}{R_{\text{Roche}}} \simeq 0.75 \left( \frac{J_2}{0.01} \right)^{1/5} \left( \frac{M_p/M_*}{0.001} \right)^{-2/15} \left( \frac{R_p}{R_{\text{Jup}}} \right)^{2/5} \left( \frac{a/R_*}{21.5} \right)^{3/5} \left( \frac{\rho_r}{3 \text{ g cm}^{-3}} \right)^{1/3}, \quad (3.5)$$

where  $J_2$  is the quadrupole gravitational moment of the planet which ranges from  $\sim 0.003$ – $0.015$  for the Solar System giant planets (Carter and Winn, 2010a). For  $R_L/R_{\text{Roche}} > 1$ ,  $R_L$  is large so the rings are entirely within  $R_L$  and thus lie in the equatorial plane of the planet. For  $R_L/R_{\text{Roche}} < 1$ ,  $R_L$  is small so the rings extend beyond  $R_L$  and so transition from lying in the equatorial plane close to the planet to lying in the orbital plane farther from the planet (Schlichting and Chang, 2011).

Using Eq. 3.5, we can calculate that close-in planets will have  $R_L/R_{\text{Roche}} < 1$ , and the rings will align with the orbital plane making them edge-on and hard to detect (see Fig. 3.1; Saturn's rings are also not visible when viewed edge-on). Longer period planets are therefore more favourable for detecting rings since their rings can have non edge-on orientations.

### 3.3 SOAP3.0 ringed planet transit tool

The transit signal of a ringed planet is modelled here with the SOAP3.0 transit tool (Akisanmi et al., 2018). SOAP3.0 is capable of generating transit light-curve and RM signal for a transiting ringed planet. SOAP3.0 was developed as a modification to previous versions of the SOAP code presented, with various additions, in Boisse et al. (2012), Oshagh et al. (2013b), and Dumusque et al. (2014). The previous versions simulate the photometric and RV effects of stellar activity on the surface of a rotating star, and the impact on planetary transits.

SOAP3.0, as with the predecessor tools, numerically simulates the star as a square grid of  $n \times n$  cells on the sky-plane. Each cell contains a flux value and a cross-correlation function (CCF). The CCF is modelled by a Gaussian with a defined width and amplitude (or using the Solar CCF) which is Doppler-shifted from cell to cell based on the local projected rotational velocity. The flux and resulting CCF in each cell is weighted by the quadratic limb darkening law. For a transiting planet, its position and projected area on the stellar grid are calculated at each phase. Afterwards, the flux and CCF contributions of the planet-eclipsed grid points are subtracted from the stellar disk-integrated value (Oshagh et al., 2013b). Similarly, in the case of a ringed planet, the projected area of the planet+ring is calculated and the contributions from the eclipsed grids are subtracted.

The rings are assumed to be circular, geometrically thin, uniform, and opaque. The ring is defined by inner and outer radii  $r_{\text{in}}$  and  $r_{\text{out}}$  in units of the planetary radius  $R_p$ . The ring has two orientation angles:  $i_r$  is the inclination of the ring plane with respect to the sky plane ( $0^\circ$  and  $90^\circ$  for face-on and edge-on rings projections respectively) while  $\theta$  defines the obliquity/tilt of the ring from the orbital plane. It ranges from  $0 - 180^\circ$  and is measured anti-clockwise from the transit chord as indicated in Fig. 3.1.

We see in Fig. 3.1 that the maximum projected ring area is at face-on ( $i_r = 0^\circ$ ) while the minimum is at edge-on ( $i_r = 90^\circ$ ) where the planet appears ringless. The effective projected area  $A_{\text{P+R}}$  is given by (Zuluaga et al., 2015)

$$A_{\text{P+R}} = \overbrace{\pi R_p^2}^{\text{planet}} + \overbrace{\pi R_p^2 [\xi^2(r_{\text{out}}) - \xi^2(r_{\text{in}})]}^{\text{ring}} \quad (3.6)$$

where  $\xi$  calculates the effective outer and inner ring radius taking into account regions

of overlap between the ring and planet. It is given as

$$\xi^2(r_{\text{in/out}}) = \begin{cases} r^2 \cos i_r - 1 & : r \cos i_r > 1 \text{ (no overlap)} \\ r^2 \cos i_r \frac{2}{\pi} \arcsin(z) - \frac{2}{\pi} \arcsin(z r \cos i_r) & : \text{otherwise} \end{cases} \quad (3.7)$$

with  $z = \sqrt{r^2 - 1}/r \sin i_r$ .

Planetary rings like those of Saturn, being the most extensive and most opaque, are the best cases for detection since they block out the most light during transit. Therefore, we consider Saturn-like rings in the discussions that follow.

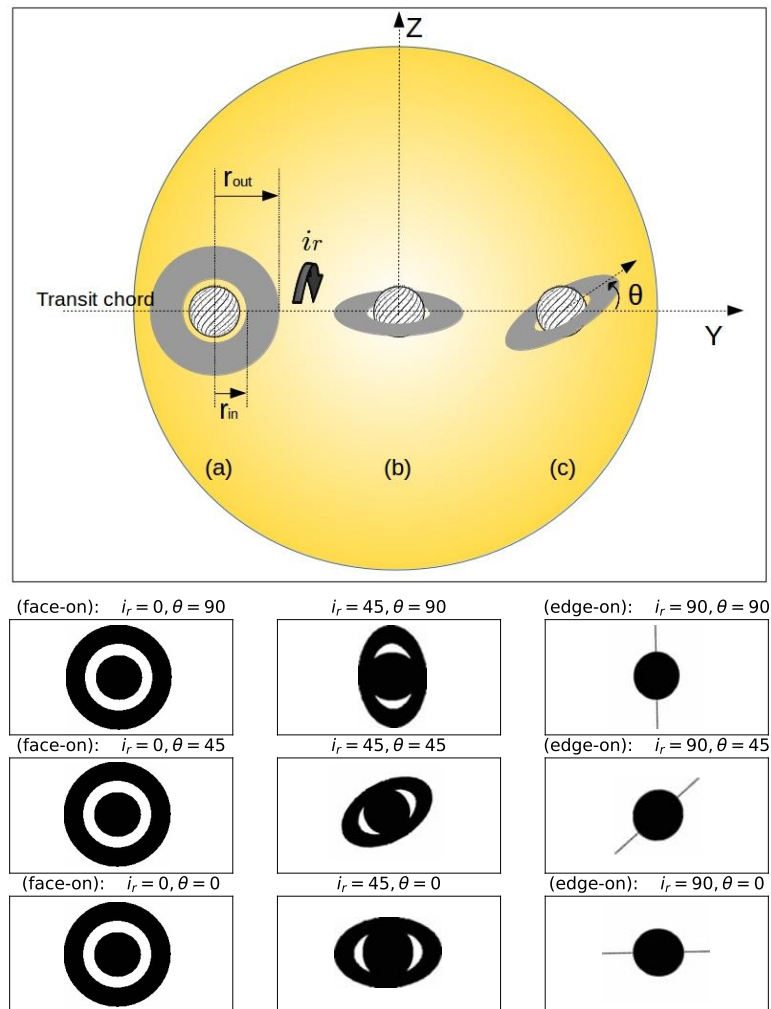


Figure 3.1: *Top*: Schematic of a transiting ringed planet with different ring orientations with sky plane YZ. (a) planet with face-on ring ( $i_r = 0^\circ$ ). (b) planet with  $i_r = 60^\circ, \theta = 0^\circ$ . (c) planet with  $i_r = 60^\circ, \theta = 30^\circ$ . *Bottom*: More  $i_r$  and  $\theta$  combinations (Adapted from Akinsanmi et al., 2018, 2020).



## 3.4 Ringed planet transit signals

To show the light-curve and RM signal generated by SOAP3.0, I simulate the transit of a Saturn-sized planet with rings orbiting the Sun with a period of 5 yrs. The adopted parameters in the simulation are given in Table 3.1 with ring parameters similar to those of Saturn’s B-ring<sup>1</sup>.

The light-curves and RM signals for the transit of the planet with ring and also the planet alone (without ring) are shown in Fig. 3.2. We see that since the ring blocks additional light, it leads to a deeper transit light-curve and larger RM signal amplitude. Furthermore, due to the radial extent of the ring, a longer transit is also observed.

### 3.4.1 Effects of rings on transit-derived parameters

The ring-induced signatures (in the light-curve and RM signal) are obtained by fitting the simulated ringed planet signals with planet-only transit models. The light-curve and RM signal of the fitted model and their residuals are also shown in Fig. 3.2. The ring signatures in the residuals show anomalies in the ingress and egress regions owing to the non-spherical projected planet+ring shape and the gap between the planet and ring. The ring gap has been shown to be important for identifying rings (see e.g. Barnes and Fortney, 2004; Ohta et al., 2009; Akisanmi et al., 2018). We obtain ring signature amplitudes of 210 ppm and  $2.3 \text{ m s}^{-1}$  from the light-curve and RM signal respectively.

As expected, the parameters from the planet-only model fit adjust to emulate the longer and deeper transit of the simulated ringed planet signals. We retrieve a larger  $R_p$ , higher  $b$  lower  $a/R_*$  and different LDCs than the simulated values. A comparison of the simulated values to the result from the light-curve fit is given in Table 3.1. When combined with a known planetary mass, the larger inferred  $R_p$  leads to a lower planetary density that is only 1/3 of the true simulated value. Similarly, the lower inferred  $a/R_*$  leads to a lower stellar density  $\rho_*$  (following Eq. 1.8) that is only 2/3 of the true stellar density.

The variation in the derived parameters and the ring signature amplitude depend on the combination of ring orientation angles  $\theta$  and  $i_r$ . To show the variation of the derived parameters from light-curve fits, I simulated ringed planet light-curves with different  $i_r - \theta$  combinations and fit each light-curve with a planet-only model. The difference (or

---

<sup>1</sup>[caps.gsfc.nasa.gov](https://caps.gsfc.nasa.gov)

Table 3.1: Adopted parameters for the Saturn-like ringed planet

Parameters	Simulated ringed planet values	Planet-only light-curve fit
$R_*$ [ $R_\odot$ ]	1.0	–
$\rho_*$ [ $\text{g cm}^{-3}$ ]	1.41	0.926
$u_1, u_2$	0.29, 0.34	0.488, 0.122
$\nu \sin i_*$ [km/s]	2	–
$a/R_*$	628.76	546.49
$P$ [yr]	5	–
$b$	0	0.49
$R_p$ [ $R_*$ ]	0.0836	0.1216
$\rho_p$ [ $\text{g cm}^{-3}$ ]	0.687	0.223
$\lambda$ [ $^\circ$ ]	0	–
$r_{in}$ [ $R_p$ ]	1.527	–
$r_{out}$ [ $R_p$ ]	2.170	–
$i_r$ [ $^\circ$ ]	60	–
$\theta$ [ $^\circ$ ]	26.7	–

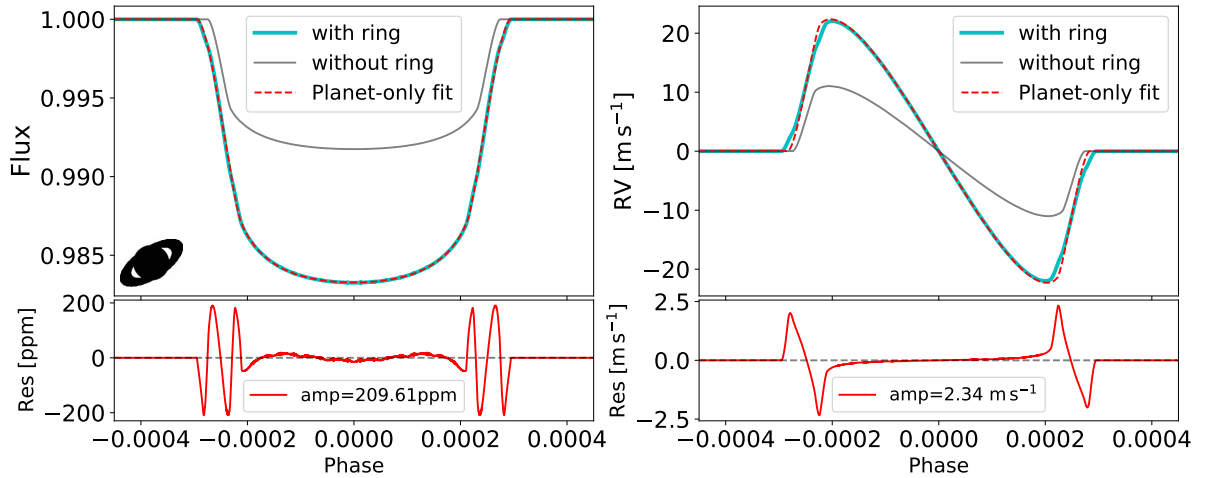


Figure 3.2: Transit light-curve (left) and RM signal (right) of a Saturn-like ringed planet (cyan) compared to the same planet without rings (gray). The planet-only fit of the ringed planet signals are shown in red and the residuals in the bottom panels. Adapted from (Akisanmi et al., 2018).

ratio) between the recovered parameters ( $\rho_*$ ,  $\rho_p$ ,  $b$ ) and the true values are used to create contour plots shown in Fig. 3.3.

In all the contour plots, blue regions indicate orientations where there isn't much variation between the ringed planet and planet-only models. This is usually close to edge-on orientations ( $i_r \simeq 90^\circ$ ) where the rings do not block stellar light. The red regions

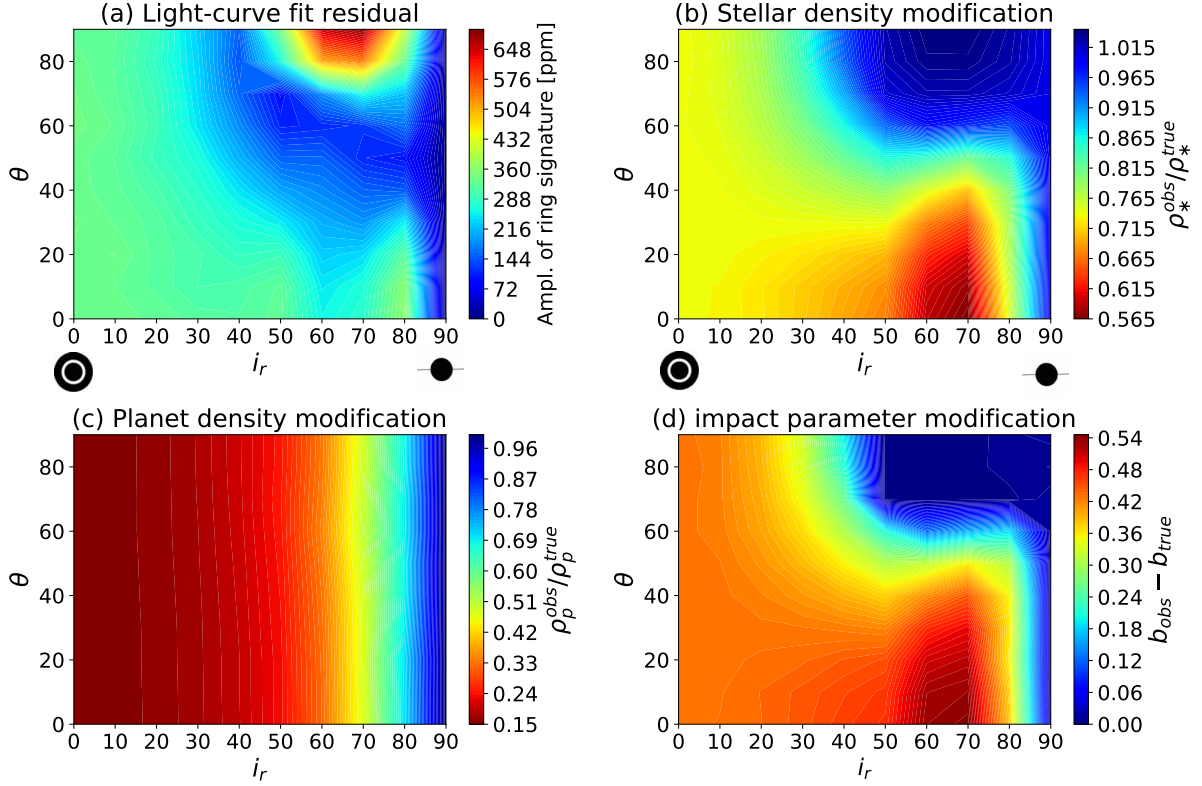


Figure 3.3: Contour plots showing variation in different derived (observed) parameters when the light-curves of a ringed planet with different ring orientations is fitted with a planet-only model. **(a)**: The amplitude of the ring signature at different ring orientations. **(b)**: The ratio of the observed stellar density to the true density. **(c)**: The ratio of observed planet density to the true values. **(d)**: The difference between the observed impact parameter and the true values.

indicate orientations where the variations are most significant. The contour plot for the planet density contour only varies with  $i_r$  but shows that the derived planet density is always underestimated  $\rho_p^{obs}/\rho_p^{true} < 1$  for  $i_r \neq 90^\circ$ . The interesting consequence of this is that planets discovered with anomalously low densities can be “masquerading” ringed planets and thus can be good targets for probing the presence of rings.

In the next section, I investigate the possibility that a planet with an anomalously low density can be a ringed planet.

## 3.5 Rings around Low-Density Planets

This section was originally published as: **Akinsanmi, B.**, Santos, N. C., Faria, J. P., Oshagh, M., Barros, S. C. C., Santerne, A., & Charnoz, S.; *Can planetary rings explain the extremely low density of HIP 41378 f?*; *A&A*, 635, L8 (2020).

### 3.5.1 Introduction

As shown in the previous section, extremely low density planets provide a unique and unexplored planet class to search for the presence of rings (Piro and Vissapragada, 2020). Such planets have been referred to as “super-puffs”. Examples of detected super-puffs are Kepler-51 *b*, *c* and *d* (Masuda, 2014) and Kepler-79 *d* (Jontof-Hutter et al., 2014) all with derived densities that are below  $0.1 \text{ g cm}^{-3}$ . However, due to their faint host stars, their transits light-curves have low signal-to-noise making them very challenging to investigate the transit signature of rings.

Interestingly, the *K2* mission observed the bright star HIP 41378 ( $K=7.7$  mag) during two campaigns (C5 and C18) showing that the star hosts at least 5 transiting planets (Vanderburg et al., 2016). Particularly, the outermost planet, HIP 41378 *f*, was found to have a period of 542 days and an RV measured mass of  $12 \pm 3 M_{\oplus}$  (Santerne et al., 2019). Combining this mass with the derived planetary radius of  $9.2 \pm 0.1 R_{\oplus}$  gives an anomalously low planetary density of  $\sim 0.09 \text{ g cm}^{-3}$  (Table 3.2) which puts it in the class of super-puffs.

It is thus interesting to investigate the possibility that the low density of HIP 41378 *f* can be due to the presence of planetary rings. Its large semi-major axis of  $\sim 1.4$  AU makes it particularly interesting in the search for rings as they can be similar to the ringed objects in the solar system which all orbit far from the Sun. As discussed in §3.2.1, planets orbiting at large distances from their host stars are less influenced by the tidal forces of the star allowing them have large enough Hill radii to support stable rings. Furthermore, the rings of such planets are able to have a wide variety of orientations that can favour their detection (Schlichting and Chang, 2011). The orbit of HIP 41378 *f* is consistent with an eccentricity of zero (Santerne et al., 2019) which is also favourable for hosting stable rings (§3.2.1) as it ensures a constant stellar tidal influence.

Table 3.2: Parameters of HIP 41378 star and planet  $f$  (Lund et al., 2019; Santerne et al., 2019).

Parameter [unit]	Symbol	Value
Stellar mass [ $M_{\odot}$ ]	$M_*$	$1.160 \pm 0.04$
Stellar radius [ $R_{\odot}$ ]	$R_*$	$1.273 \pm 0.02$
Stellar density [ $\rho_{\odot}$ ]	$\rho_*$	$0.563 \pm 0.01$
Effective temperature [K]	$T_{\text{eff}}$	$6320^{+60}_{-30}$
Stellar rotation velocity [ $km s^{-1}$ ]	$\nu \sin i_*$	$5.6 \pm 0.5$
Planet period [days]	$P$	542.08
Transit time [BJD]	$t_0$	2457186.91
Planet mass [ $M_{\oplus}$ ]	$M_p$	$12 \pm 3$
Planet radius [ $R_{\oplus}$ ]	$R_p$	$9.2 \pm 0.1$
Planet density [ $g cm^{-3}$ ]	$\rho_p$	$0.09 \pm 0.02$
Inclination [ $^{\circ}$ ]	$i_p$	$89.97 \pm 0.01$
Semi-major axis	$a/R_*$	$231.1 \pm 0.8$
Equilibrium temperature [K]	$T_{\text{eq}}$	$294^{+3}_{-1}$

### 3.5.2 Approach

To investigate the ringed planet hypothesis, I perform Bayesian model comparison by computing the evidence (recall §2.2.1) for the planet-only and ringed planet scenarios given the observational data from the  $K2$  mission. The planet-only model has  $R_p$ ,  $a/R_*$ ,  $i_p$ ,  $u_1$  and  $u_2$  as free parameters while the ringed planet model additionally has  $r_{\text{in}}$ ,  $r_{\text{out}}$ ,  $i_r$  and  $\theta$ .

#### Transit data

The star HIP 41378 was observed in long-cadence mode (LC;  $\sim 30$  mins) during  $K2$  C5 and then in short-cadence mode (SC;  $\sim 1$  min) in C18. The light-curves of HIP 41378 were reduced using the K2SFF pipeline (Vanderburg and Johnson, 2014; Santerne et al., 2019) without significant modification of the in-transit data. Searching for ring signatures in light-curves require high time resolution data so the analyses was performed on the C18 SC light-curve of HIP 41378  $f$  (1933 transit data points) and the consistency of the result is checked with the C5 light-curve. A cursory fit of a spherical planet transit model to the light-curve (Fig. 3.4) reveals no visual sign<sup>2</sup> of the characteristic residual

<sup>2</sup>Although some artifacts of the reduction process can be noticed in the C18 light curve of HIP 41378  $f$ , further correction was avoided to prevent removing possible ring features.

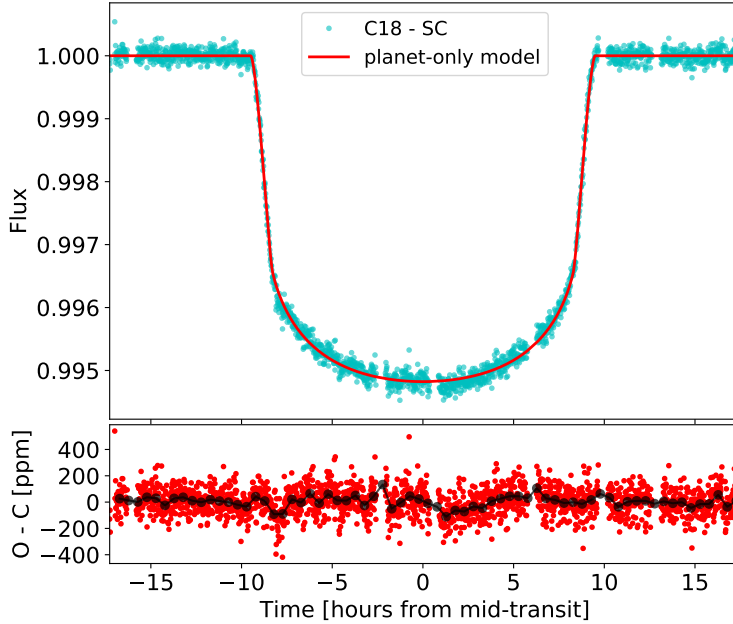


Figure 3.4: C18 short-cadence data (cyan points) of HIP 41378 *f* and the spherical planet transit model fit (red line). The residual (red points) of the fit and its 30 min binned points are shown in the bottom panel.

ingress and egress anomalies that can be caused by the presence of rings<sup>3</sup> (Fig. 3.2; Akin-sanmi et al. 2018). However, it has been shown that these ring signals can be masked if  $r_{\text{in}}$  is sufficiently close to the planet surface (Ohta et al., 2009). The lack of discernible ingress/egress signature in the residual could also imply that any possible ring around the planet, capable of producing the observed transit depth, must be densely packed and opaque else the transition between the less opaque ring and completely opaque planet would have left a significant imprint during ingress and egress. Therefore, the putative ring is assumed to be completely opaque.

### Model priors

To calculate the evidence of each model given the C18 SC data, it is important to define appropriate priors on the parameters of the models since the evidence is very sensitive to their values. The prior on  $a/R_*$ , is obtained using Eq. 1.8 with values of the planetary period and the stellar density (Table 3.2). A careful selection of priors for the stellar limb darkening coefficients is necessary since their effect is prominent at ingress/egress where ring signatures can also manifest. The quadratic LDCs ( $u_1, u_2$ ) were first interpolated from Claret and Bloemen (2011) using parameters of the host star (Lund et al., 2019). Thereafter, a better estimate of their values was obtained from the joint transit fitting

<sup>3</sup>Recall from §2.3.2 that even when the amplitude of a sought-after feature is below the noise level of the observation, it is still possible for model comparison to prefer the model with the feature over the simpler model.

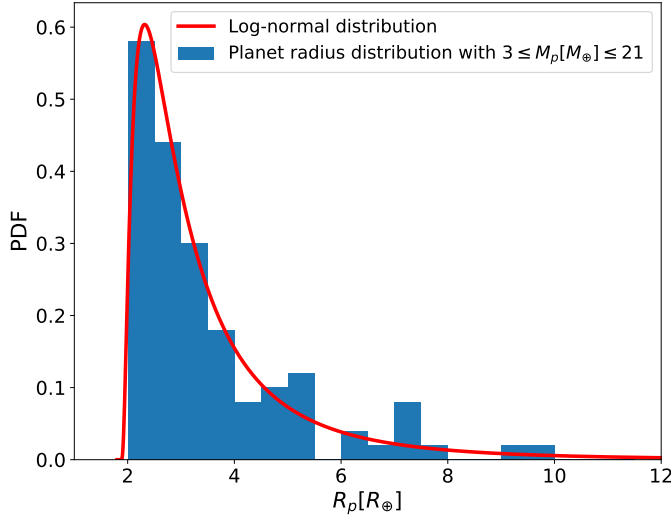


Figure 3.5: Radius distribution of planets with masses within  $3\sigma$  of the mass of HIP 41378 *f* (obtained from NASA exoplanet archive) and fitted log-normal distribution used as prior on  $R_p$ .

of the other planets in this system (excluding planet *f*). The resulting values and associated uncertainties were then used as priors in both the planet-only and ringed planet models (see Table 3.3). The planet eccentricity was kept fixed at zero as derived from RV observations in Santerne et al. (2019).

To define priors for the planetary radius  $R_p$ , the radius distribution of detected planets<sup>4</sup> was used but selecting only planets with masses within  $3\sigma$  of the mass of HIP 41378 *f*. This broad distribution is used because it spans a wide range of planetary radii including those of the aforementioned super-puff planets making it suitable as prior for the planet-only and ringed planet models. Given the mass, HIP 41378 *f* is expected to be a gaseous planet so planets with radii below  $2 R_\oplus$  were removed to avoid those with rocky compositions (Marcy et al., 2014). The resulting radius distribution was found to be well-represented by a log-normal distribution (Fig. 3.5) which was then used as the prior on  $R_p$  in both models.

To obtain priors for the outer ring radius,  $r_{\text{out}}$ , we recall that rings are only stable within the Roche radius of the planet (Eq. 3.2). Therefore, the possible rings around this planet must have  $r_{\text{out}} \leq R_{\text{Roche}}$ . However, the underlying planet density  $\rho_p$  and ring density  $\rho_r$  required to calculate  $R_{\text{Roche}}$  are unknown. The main rings of the solar system’s giant planets are within their respective planet’s Roche radius which does not vary much between planets and is found to be generally around  $2-3 R_p$  (Charnoz et al., 2018b). The upper limit is adopted which means that the possible rings around this planet is assumed to also be within  $R_{\text{Roche}} = 3 R_p$ . Assuming that the rings can possibly extend from the

<sup>4</sup><https://exoplanetarchive.ipac.caltech.edu/>

planet surface, uniform priors from  $1 R_p$  to  $3 R_p$  are adopted for  $r_{\text{out}}$ . Furthermore, since rings must have  $r_{\text{in}} \leq r_{\text{out}}$ , a uniform prior is used for  $r_{\text{in}}$  ranging from  $1 R_p$  to  $r_{\text{out}}$  (the value of  $r_{\text{out}}$  is updated at every iteration of the computation).

As discussed in § 3.2.1, stable rings around a planet requires  $R_{\text{Roche}} < 2/3 R_{\text{Hill}}$ . Using Eq. 3.1 gives  $R_{\text{Hill}} = 180 R_p$  for HIP 41378 *f* implying that it can host stable and long-lived rings. Given that the equilibrium temperature of this planet,  $T_{\text{eq}} \simeq 294$  K, is higher than the sublimation temperature of water ice, the materials of any ring around this planet will need to have higher melting temperatures and densities than ice ( $\rho_r > 1 \text{ g cm}^{-3}$ ). The density of rocky materials vary from  $2 - 5 \text{ g cm}^{-3}$  depending on composition. Therefore, the computation enforced that the proposed solution must have  $\rho_r > 1 \text{ g cm}^{-3}$ .

The projected area of the ring is proportional to the cosine of  $i_r$  as shown in Eq. 3.6, so a prior distribution which is uniform in  $\cos i_r$  is adopted. Finally, an uninformative uniform prior ranging from  $0 - 180^\circ$  is used for the ring obliquity,  $\theta$ .

The derived priors on the parameters of both models are given in Table 3.3. The same priors are used when both models have parameters in common. It should be noted that different assumptions from those stated above regarding the parameters of the models could change the resulting evidence for the models and also lead to a different ring solution. Nevertheless, these priors are adopted as they are physically representative of the current knowledge of planets and rings.

### 3.5.3 Model comparison

The *dynesty* nested sampling tool is used to fit both models to the data to estimate the posterior of the parameters and the log-evidence of the models. The log-evidence from both models is compared using Eq. 2.15. The results are reported in Table 3.3 and the posterior distribution of the parameters from both models are shown in Fig. 3.6.

Comparing the evidence for both models using Eq. 2.15 results in a Bayes factor  $\mathcal{B}_{12} = 1.51$  indicating an anecdotal evidence in favour of the ringed planet model (Table 2.1). Obtaining a value of  $\mathcal{B}_{12}$  so close to unity implies that, given the *K2* C18 SC data and the adopted model priors, the ringed planet scenario is not significantly more probable and only provides a comparable evidence to the planet-only scenario. This is not surprising given that the characteristic ingress/egress transit signatures of rings



Table 3.3: Adopted priors on the models. ‘+’ indicates parameters with the same priors in both models. The median of posterior samples for each model is also given alongside the 68% credible interval.

Parameter	Priors	Planet-only model	Ringed planet model
$R_p [R_\oplus]^+$	$\log \mathcal{N}(0.95, 1.88, 1.09)$	$9.21 \pm 0.01$	$3.7_{-0.2}^{+0.3}$
$a/R_*^+$	$\mathcal{N}(231.07, 0.76)$	$231.6 \pm 0.7$	$231.0 \pm 0.6$
$i_p [^\circ]^+$	$\mathcal{U}(\cos 90, \cos 89.9)$	$89.97 \pm 0.01$	$89.97 \pm 0.01$
$u_1^+$	$\mathcal{N}(0.307, 0.006)$	$0.32 \pm 0.01$	$0.32 \pm 0.01$
$u_2^+$	$\mathcal{N}(0.31, 0.02)$	$0.28 \pm 0.01$	$0.28 \pm 0.01$
$r_{out} [R_p]$	$\mathcal{U}(1.0, 3.0)$	-	$2.6 \pm 0.2$
$r_{in} [R_p]$	$\mathcal{U}(1.0, r_{out})$	-	$1.05_{-0.03}^{+0.05}$
$i_r [^\circ]$	$\mathcal{U}(\cos 90, \cos 0)$	-	$25_{-4}^{+3}$
$\theta [^\circ]$	$\mathcal{U}(0, 180)$	-	$95_{-17}^{+16}$
$\rho_p [g\ cm^{-3}]$	-	$0.09 \pm 0.02$	$1.2 \pm 0.4$
$\log \mathcal{Z}$	-	14952.44	14952.85
$\log \hat{\mathcal{L}}_\Theta$	-	14970.85	14972.60

Recall:  $\mathcal{N}(a, b)$  - Normal prior,  $\mathcal{U}(a, b)$  - Uniform prior,  $\log \mathcal{N}(s, a, b)$  - log-normal prior with shape parameter  $s$  shifted and scaled by  $a$  and  $b$  respectively.

are either absent or well-suppressed in the data making the light-curves of both models similar. It is however interesting that the ringed model has comparable evidence to the planet-only model despite the introduction of 4 extra parameters which increases the prior volume compared to the planet-only model.

As previously mentioned, model comparison using Bayes factor is sensitive to the adopted priors for the models which motivated the selection of priors that are as physical as possible. For example, the adopted prior radius distribution favours smaller planet sizes but this is indeed the case given the measured mass of the planet. Not taking into account the knowledge of radius distribution would lead to a result that favours the planet-only model. Also, deriving the adopted radius distribution from planets with masses within  $1\sigma$  of the mass of HIP 41378  $f$ , instead of  $3\sigma$ , will lead to a prior on  $R_p$  that only favours the ringed planet model.

The resulting ringed planet solution suggests a smaller planetary radius of  $R_p = 3.7_{-0.2}^{+0.3} R_\oplus$

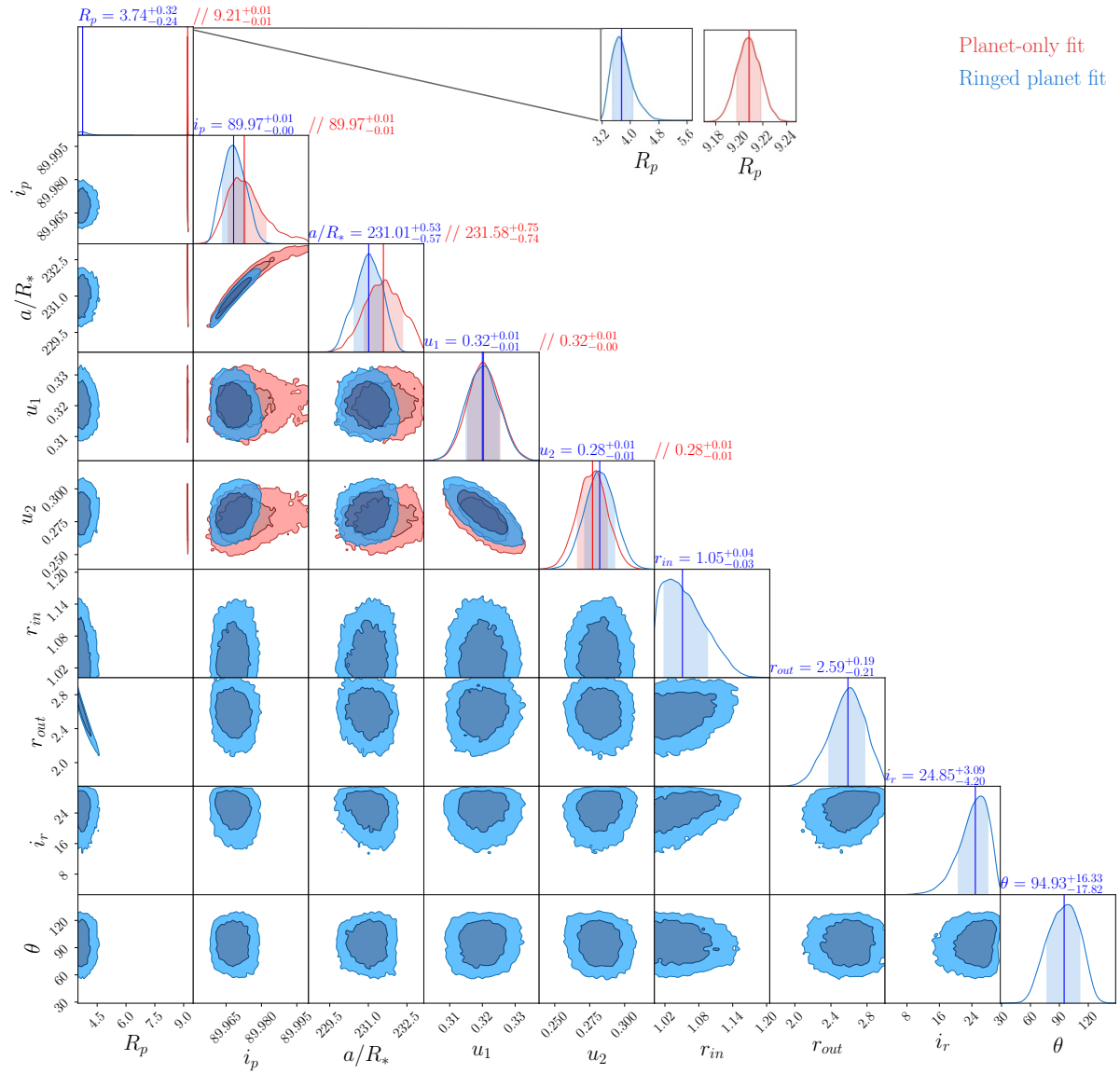


Figure 3.6: Posterior distribution of parameters of the ringed planet (blue) and planet-only models (red). The values on the histograms indicate the median and  $1\sigma$  uncertainties for the parameters of for both models. The shaded regions also correspond to the 68% credible intervals. The  $R_p$  histograms are zoomed in the inset for visibility. Image reproduced from Akinsanmi et al. (2020).

which is in the radius range obtained using mass-radius prediction tools such as `forecaster`<sup>5</sup> ( $3.3 \pm 1.4 R_{\oplus}$ ) and `bem`<sup>6</sup> ( $3.8 \pm 0.4 R_{\oplus}$ ). Combining this radius with the planet mass gives a higher planetary density of  $\rho_p = 1.2 \pm 0.4 \text{ g cm}^{-3}$  similar to that of Uranus ( $1.27 \text{ g cm}^{-3}$ ). The associated ring begins close to the planet surface with  $r_{\text{in}} = 1.05 R_p$  and extends to  $r_{\text{out}} = 2.59 R_p$ . Although Saturn’s fairly transparent D ring also begins close to the planet at  $1.11 R_p$ , it is unclear if dense opaque rings can have such proximity to the planet.

The density of the possible ring materials that can be sustained within the obtained  $r_{\text{out}}$  can be calculated by setting  $r_{\text{out}} = R_{\text{Roche}}$  in Eq. 3.2. A value of  $\rho_r = 1.08 \pm 0.3 \text{ g cm}^{-3}$  is obtained with 95% upper limit of  $1.63 \text{ g cm}^{-3}$  which is denser than water ice but not as dense as typical rocky ring materials. The plausibility of such low density ring particles is questionable at the planet’s equilibrium temperature. Although porous rocky materials can have such low densities (below  $2 \text{ g cm}^{-3}$ ) as measured for some asteroids (Carry, 2012), the possible formation scenario for such a ring is unknown.

Given the adopted model priors, the best ringed planet solution indicates a ring inclination  $i_r = 25^\circ$  which allows sufficient ring projected area to match the observed transit depth. The 95% upper limit on  $i_r$  is  $30^\circ$ . So for randomly oriented ring inclinations, the statistical probability of finding a ring with  $i_r$  lower than  $30^\circ$  is  $\mathcal{P} = 1 - \cos(30^\circ) \simeq 13\%$  which is high considering that the probability of transit for this planet is only  $\sim 0.5\%$ .

It is possible to determine the plane in which the putative ring lies by computing the ratio of the Laplace radius to the Roche radius,  $R_L/R_{\text{Roche}}$ , given in Eq. 3.5. Assuming  $J_2$  values in the range of the solar system giant planets (0.003 - 0.15), we obtain  $R_L/R_{\text{Roche}} > 1.7$  implying that the plane of the possible ring around this planet will align with the equatorial plane of the planet (Schlichting and Chang, 2011). Since the ring solution indicates a ring tilted by  $\theta \simeq 95^\circ$  from the orbital plane, it implies that the planet’s equatorial plane is also  $95^\circ$  from the orbital plane similar to Uranus ( $97.86^\circ$ ).

The fit to the data using the best parameters from both models is shown in Fig. 3.7. It is seen from the root-mean-square of the residuals that both models provide comparable fit to the data. This indicates that, the possible ring around this planet emulates well the signal of a planet-only model thereby making it difficult to distinguish between both models. As a consistency check, we performed a fit of both models to the *K2* C5 LC light

<sup>5</sup>[github.com/chenjj2/forecaster](https://github.com/chenjj2/forecaster) (Chen and Kipping, 2017)

<sup>6</sup>[github.com/soleneulmer/bem](https://github.com/soleneulmer/bem) (Ulmer-Moll et al., 2019)

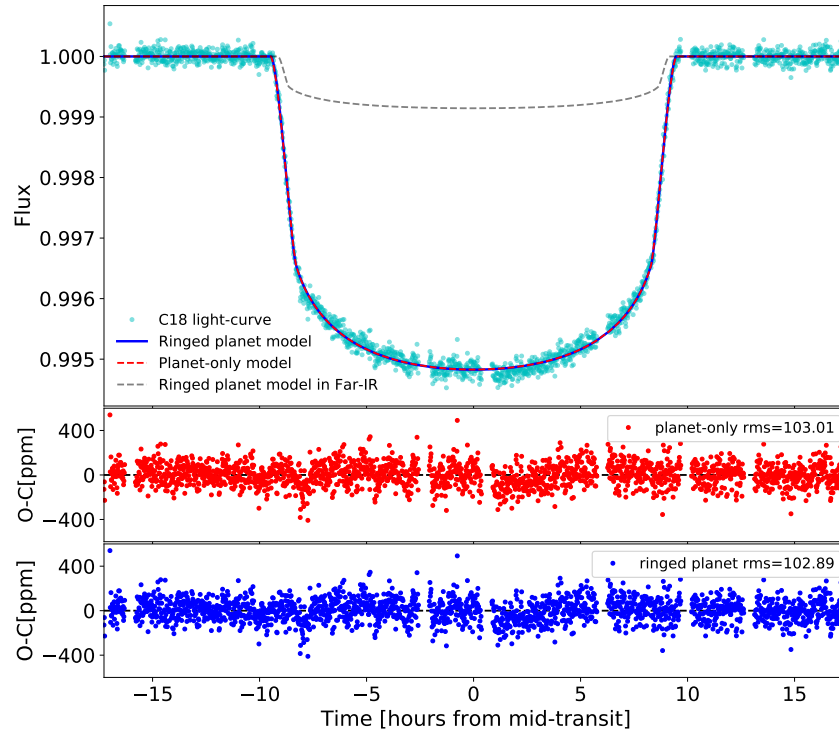


Figure 3.7: Fit of the planet-only (red dashed line) and the ringed planet (blue solid line) to the C18 SC data (cyan points). The residuals of same colour are also shown with the rms in ppm. Also plotted in the top pane (in grey) is the predicted light-curve when the ringed planet transit is observed in the far-infrared where rings are expected to be transparent.

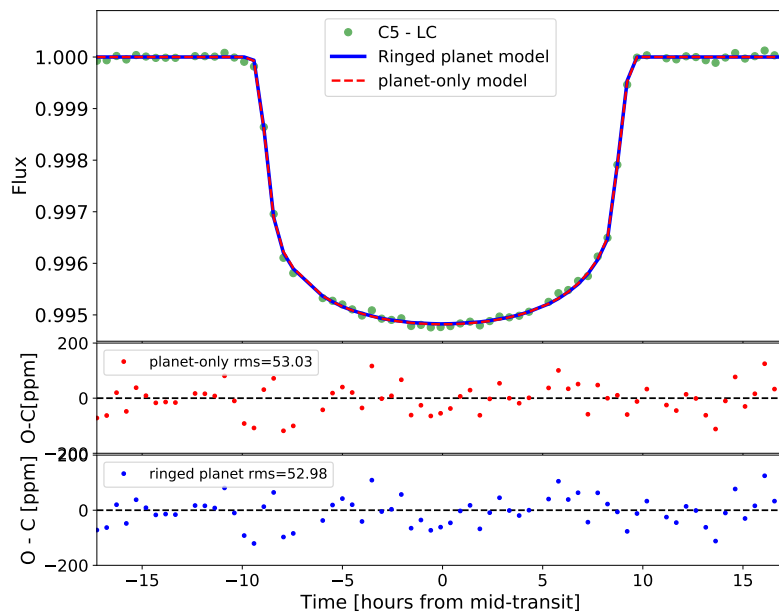


Figure 3.8: Fits of the planet-only model (red dashed line) and the ringed planet model (blue solid line) to the C5 LC data (green points). The residuals of same colour are also shown with the root-mean-square (rms) value in ppm.

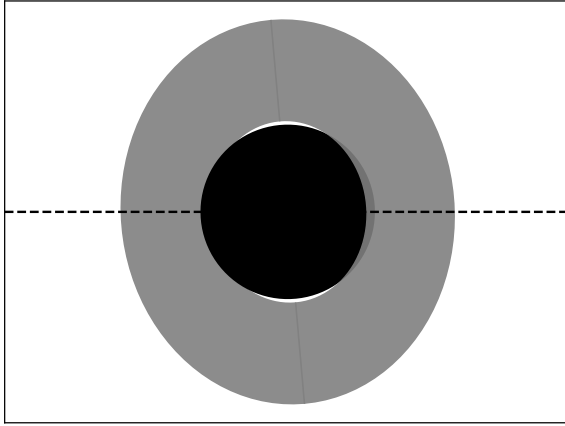


Figure 3.9: Schematic of the ringed planet solution with  $i_r = 25^\circ$  and  $\theta = 95^\circ$ . The dashed line indicates the transit chord.

curve (see Fig. 3.8) and found that the resulting values of the parameters agree with our results from the C18 light curve within  $1\sigma$ . A schematic of the ringed planet solution is shown in Fig. 3.9.

### 3.5.4 Discussion and conclusion

The results show that the *K2* light-curve of HIP 41378 *f* can be fitted by a smaller planet with opaque rings which additionally explains the planet’s unusually low density. Nevertheless, other phenomena may also be invoked to explain this anomalous radius/density. For instance, the observed large radius can be due to the planet having a small core and an extended atmosphere, possibly composed of hydrogen. Such hydrogen-rich atmospheres that can significantly increase the radius of a planet are expected to be possible for Super-Earths with masses up to  $10 M_\oplus$  (Miller-Ricci et al., 2009). For example, Adams et al. (2008) found that an atmosphere with 10% the mass of a planet can cause its radius to increase by up to 60%. This is especially so if the atmosphere is undergoing hydrodynamic loss (outflows) due to the planet’s low surface gravity (Wang and Dai, 2019). These outflows carry dust to high altitudes (enhancing the opacity of the atmosphere) which inflates the observed radius of the planet and even leads to featureless transmission spectra when probing the atmospheres. However, these outflows seem to affect planets with masses much lower than  $10 M_\oplus$  (Ohno and Tanaka, 2021) which have weak gravitational wells and so it is not clear if they can occur in higher mass planets like HIP 41378 *f*.

Several studies have also provided some explanations for the radius inflation of exoplanets mostly pointing to the correlation between the radius inflation and the level of radiation it receives from the star (Lopez and Fortney, 2016). For a particular star, the planets in close proximity will generally receive a higher stellar insolation and be more

inflated than those further out. At the distance of 1.4 AU, HIP 41378 *f* receives only a low level of irradiation that is not sufficient to significantly puff it up as observed. Although young planets (<10 Myrs) are also expected to be inflated due to retained internal heat from their formation, this might not explain the case of HIP 41378 *f* as it is estimated to be 3.1 Gyrs old (Lund et al., 2019) and expected to have cooled off.

Besides focusing on the enlarged radius, it is necessary to check the possibility that the derived mass for the planet is not underestimated. The induced RV signal amplitude,  $\sim 1\text{m/s}$ , of the planet is at the level of the instrumental stability and thus the derived mass could be influenced by unknown systematics (Santerne et al., 2019). However, a larger planetary mass is unlikely as it would cause larger RV amplitudes which would have been easier to detect. Further RV observations of this target using high precision spectrographs has been advocated for in order to refine the planetary mass (Santerne et al., 2019).

Having considered these non-exhaustive alternatives, one can conclude that the ring hypothesis presents, at least, a possible option to explain the observed low density. Further observations will be necessary to confirm/characterise the ring scenario. Transmission spectroscopy can be useful in probing the nature or presence of such rings as their opacity might vary with wavelength depending on the composition and density of the ring materials. However, solar occultations of Saturn’s main rings have revealed featureless transmission spectra with the ring materials being almost completely opaque at visual and near-infrared wavelengths (Nicholson et al., 2008). At far-infrared (FIR) wavelengths, the rings should be optically thinner and we might expect to measure a shallower transit corresponding to a smaller planetary radius. The predicted light-curve of the ringed planet at FIR wavelength (where the ring might be transparent) is also shown in Fig 3.7.

As the Bayesian evidence for the ringed planet model is only comparable to that of the planet-only model, it is difficult to categorically ascertain the reality of these rings as they mimic well the light-curve of a planet-only model. Thus, we are only able to say, given the data, that the ring hypothesis presents one plausible explanation for the inferred low density of the planet. The ringed planet scenario also poses a challenge regarding the possibility of hosting low density/porous ring materials at the planet’s high equilibrium temperature. This planet will benefit from future transit observations to validate its true nature. Transit observations with higher precision (using *HST* or *JWST*) will be

necessary to identify ingress/egress signatures which will be useful in constraining the parameters of the possible ring and the underlying planet radius.

# Chapter 4

## Tidal Deformation of Planets

Following the detection of the first hot-Jupiter, 51 Peg b, several other similar planets with short orbital periods have been detected and there has been large motivation to study their origins and characteristics (Dawson and Johnson, 2018; Fortney et al., 2021). Short period giant planets are interesting because their high transit probability and stellar proximity allows to measure both their radii and masses giving estimates of their bulk densities. Their short periods also makes them very interesting targets for atmospheric studies through transit spectroscopy and phase curve observations (Kreidberg, 2018b; Parmentier and Crossfield, 2018).

An even more distinct class of these short period planets are called Ultra-Hot Jupiters (UHJs). These planets orbit very close to their host stars with periods less than 1–2 days. Due to this proximity, they are subjected to intense tidal forces from their stars which deforms them i.e., their shapes depart from the usual spherical approximation used to describe planets. The shape of a planet can have an discernible effect on the observed transit light-curve. As such, it is possible to detect the tidal deformation of a planet from high-precision transit light-curves. Furthermore, since the response of a planet to a perturbing potential depends on the its internal mass distribution, detecting tidal deformation gives insight into the interior structure of the planet which is described by an intrinsic property of the planet called the *second fluid Love number*  $h_f$ .

This chapter deals with the detection of tidal deformation and measurement of  $h_f$  from transit light-curves. I start with the importance of measuring  $h_f$  and then present a model and tool to simulate the transit light-curve of a tidally deformed planet parameterised on the Love number. Afterwards, I discuss the detectability of tidal deformation and estimation of  $h_f$  considering the precision of different instruments and also highlight



potentially interesting targets.

This chapter was originally published as: **Akinsanmi, B.**, Barros, S. C. C., Santos, N. C., Correia, A. C. M., Maxted, P. F. L., Boué, G., & Laskar, J.; *Detectability of shape deformation in short-period exoplanets*; *A&A*, V621 (2019).

## 4.1 Planetary interiors and Love numbers

As mentioned in Chapter 1, measurement of the mass and radius of a planet, obtained from RV and transit observations respectively, yields an estimate of the mean density which allows distinguishing rocky planets from their gas rich counterparts. However, as different combinations of mass and radius can result in the same mean density, mass and radius measurements are not sufficient to uniquely constrain the interior structure of the planet. A common method for gleaning planetary interiors involve comparing the mass and radius estimates of the planet to density profiles on theoretical mass-radius curves (Zeng and Sasselov, 2013; Gettel et al., 2016; Sotin et al., 2007). The density profiles are derived from the thermodynamic properties (equation of state) of constituent materials in the different layers (e.g core, mantle and atmosphere in three-layer models) of the planet (Grasset et al., 2009; Zeng and Sasselov, 2013). Detailed interior characterisation of a planet requires computing a large number of possible interior models that could fit the measured mass and radius (Fortney et al., 2007; Sotin et al., 2007). Nonetheless, the solution can be degenerate, producing multiple interior models that match the observations (Dorn et al., 2015, 2017). Therefore, additional constraints are necessary to reduce model degeneracy. Elemental abundances from the host star (e.g. Fe/Si and Mg/Si) have been proposed to alleviate model degeneracy and constrain the compositions of super-Earths (Dorn et al., 2015; Brugger et al., 2017; Adibekyan et al., 2021; Santos et al., 2017).

Estimate of the fluid Love numbers of a planet can also provide direct constraints on the interior structure since they depend on the radial density distribution within the planet (Love, 1911; Kramm et al., 2011). The Love numbers  $h_n$  and  $k_n$  (with degrees  $n \geq 2$ ) were introduced by Love (1911) to characterise the response of a planet to perturbing potentials (e.g., tidal or rotational). They are dimensionless quantities that depend on the interior properties of the planet such as the radial density distribution, viscosity, and rigidity. Particular emphasis is placed on the second-degree Love numbers  $h_2$  and  $k_2$  since the higher degrees are less sensitive to the interior structure. The Love number  $h_2$

describes the radial displacement,  $\Delta R$ , of the planet surface due to the perturbing potential  $V_p$  while  $k_2$  describes the induced potential,  $V_{ind}$ , at the planet surface in response to the perturbation. They are given by:

$$\Delta R = h_2 V_p / g, \quad (4.1)$$

and

$$V_{ind} = k_2 V_p \quad (4.2)$$

where  $g$  is the average surface gravity of the planet. The derivations of the different Love numbers are given e.g., in Love 1911; Sabadini and Vermeersen 2004; Kramm et al. 2011; Kellermann et al. 2018; and Correia et al. 2014.

For a planet in hydrostatic equilibrium, the interior behaves as a fluid and the Love numbers only depend on the radial density distribution (Correia et al., 2014). In this case, the notation is changed (following Correia 2014) to  $h_f$  and  $k_f$  to denote the *second fluid Love numbers* for radial deformation and potential respectively. For a planet in hydrostatic equilibrium, the fluid Love numbers are related as  $h_f = k_f + 1$  (Sterne, 1939; Correia et al., 2014). The magnitude of  $h_f$  depends on the distribution of mass within the planet and can be thought of as a measure of the central condensation of a body (Kramm et al., 2011, 2012). It has physical values ranging from 1 to 2.5 where the maximum  $h_f = 2.5$  corresponds to a homogeneous body (like asteroids) and  $h_f = 1$  implies a highly differentiated body with most of its mass condensed in a relatively small core such as FGK stars. However, a body that is not in hydrostatic equilibrium can have  $h_f < 1$ .

The second fluid Love numbers thus provides strong constraints on interior structure models that could break the degeneracies between bulk composition and interior differentiation of the planet (Ragozzine and Wolf, 2009). For example, Baumeister et al. (2020) showed that including fluid Love number measurement as input to interior structure models significantly reduces the number of possible configurations for the interior. Love number estimates and constraints on the interior of Solar system planets are obtained from spacecraft and probe measurement of their gravitational moments and rotation. For example, using gravitational moment measurements from the *Cassini* spacecraft, Lainey et al. (2017) estimated Saturn's Love number as  $k_f = 0.39$  (i.e.  $h_f = 1.39$ ) whereas *Juno* spacecraft was used to obtain a value of  $k_f = 0.565$  for Jupiter (Durante et al., 2020) indicating a lower core mass fraction (more homogeneous) than Saturn.

Estimating the Love number for exoplanets however requires more indirect measurements. One method that has been employed is through observations of the apsidal precession of a planet’s eccentric orbit due to non-spherical planet shape and general relativistic effects (Sterne, 1939; Ragozzine and Wolf, 2009). Apsidal precession means that the argument of periastron  $\omega$  changes with time which can be observed through RV measurements. The precession also leads to changes in the transit epoch that is observed as TTVs. Both observations, independently or combined, can be used to derive the apsidal motion constant which is equal to half the value of  $k_f$ . (Sterne, 1939; Ragozzine and Wolf, 2009; Csizmadia et al., 2019). However, measuring apsidal motion requires long baseline of observation and assumptions about the planet rotation rate. Using RV observations spanning  $\sim 5$  years, Csizmadia et al. (2019) estimate  $k_f = 0.62_{-0.19}^{+0.55}$  for the hot Jupiter WASP-18Ab. A unique orbital configuration of HAT-P-13b (eccentric orbit due to highly eccentric outer companion) also allowed measurement of its Love number from precession (Buhler et al., 2016). The other method is by measuring the changes induced in the transit light-curve due to the non-spherical shape of the planet. The later method is investigated in this following sections.

## 4.2 Effects of tidal deformation

A non-spherical planet shape can lead to deviations from the standard transit light-curve morphology described in Chapter 1 (Seager and Hui, 2002; Carter and Winn, 2010a,b). Assuming planet sphericity in the typical transit light-curve analysis allows a spherical radius  $R_{\text{sph}}$  to be obtained. However, Leconte et al. (2011) showed that  $R_{\text{sph}}$  underestimates the true planetary radius when the planet is deformed due to tidal or rotational forces. As a result, the derived planetary density will overestimate the true value. Based on the Roche approximation (Chandrasekhar, 1969), Burton et al. (2014) provided density corrections for several short-period planets expected to be tidally deformed.

Tidal deformation is especially significant for planets orbiting close to the Roche limits of their host stars where the tidal influence is greatest. A number of ultra-hot Jupiters have such close orbits that they are on the verge of tidal disruption (e.g., Gillon et al. 2014; Delrez et al. 2016). For some of these planets, theoretical models (e.g. by Budaj 2011 and Leconte et al. 2011) are used to estimate the planet shape and correct the derived spherical radii and densities for the expected deformation (e.g., Southworth et al. 2015; Delrez et al. 2016, 2018). However, these models make assumptions about

the interior structure of the planet and so the actual equilibrium shape of the planet might differ from the model. Therefore, observational measurements of the shape of such planets, from transit light-curve, are necessary to infer the true extent of deformation and provide better estimates of the planetary radii.

## 4.3 Modelling tidal deformation

### 4.3.1 Planet shape model

Correia (2014) formulated an analytical model to calculate the shape of a deformed planet based on the second fluid Love number  $h_f$ . The model, being parameterized by  $h_f$ , allows for the interior structure of the planet to dictate how it deforms in response to the perturbing potential. The planet is described by a triaxial ellipsoid centred at the origin of a Cartesian coordinate. As shown in Fig. 4.1, the semi-principal axes  $(r_1, r_2, r_3)$  of the ellipsoid are aligned with the  $X, Y, Z$  axes of the coordinate system, respectively.

The equilibrium shape and mass distribution of a planet depends on the forces acting on it, namely the planet's self gravity, perturbing centrifugal potential due to its rotation and tidal potential from the star. Tidal evolution of a close-in planet leads to an equilibrium configuration (Hut, 1980) characterised by a circularised orbit, synchronous rotation and zero obliquity (equator aligns with orbital plane). The rotation of the planet about the  $Z$ -axis leads to rotational deformation (oblateness) such that  $r_1 = r_2 > r_3$ . Similarly, the synchronous rotation causes the semi-principal axis  $r_1$  of the planet to always points towards the star leading to a tidal deformation along  $r_1$ , so that  $r_1 > r_2 = r_3$ .

Therefore, the combined effect of rotation and tides leads to a triaxial planet shape with  $r_1 < r_2 < r_3$  as observed in several satellites in the solar system. For a synchronously rotating planet, the magnitude of the tidal deformation is 3 times that of rotation (Murray and Dermott, 2000; Ragozzine and Wolf, 2009) implying that the shapes of close-in planets are mostly affected by tidal forces. Farther away from the stars, significant planet rotation makes rotational oblateness more dominant. This scenario is investigated in Chapter 5.

For the triaxial ellipsoid, the radius of a sphere that will enclose the same volume as

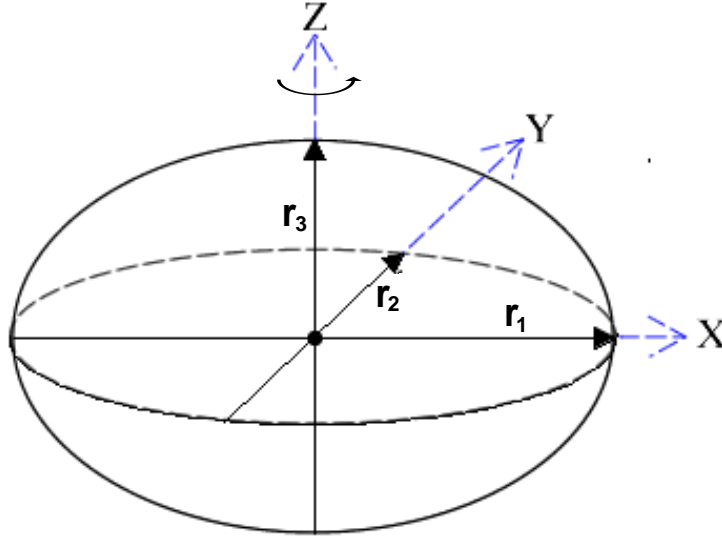


Figure 4.1: Schematic of triaxial ellipsoid centred on the origin of the Cartesian coordinate system  $(X, Y, Z)$  with sky-plane  $YZ$ . The positive  $X$ -axis points radially towards the star,  $Z$  is parallel to the orbit normal (planet rotation axis), while  $Y$  is along the planet orbit.

the ellipsoid can be defined so that

$$R_v = (r_1 r_2 r_3)^{1/3}. \quad (4.3)$$

According to the formulation by Correia (2014), the semi-principal axes are related as  $r_1 = r_2(1 + 3q)$  and  $r_3 = r_2(1 - q)$  where  $q$  is an asymmetry parameter. From Eq. 4.3,  $r_2$  can be written as a function of  $R_v$ , to first order in the parameter  $q$ , as

$$r_2 \simeq R_v \left( 1 - \frac{2}{3}q + \dots \right), \quad (4.4)$$

so that

$$r_1 = r_2(1 + 3q) \simeq R_v \left( 1 + \frac{7}{3}q \right) \quad (4.5)$$

and

$$r_3 = r_2(1 - q) \simeq R_v \left( 1 - \frac{5}{3}q \right). \quad (4.6)$$

The asymmetry parameter  $q$  depends on  $h_f$  as

$$q = \frac{h_f M_*}{2 M_p} \left( \frac{R_v}{a} \right)^3. \quad (4.7)$$

As seen from Eqs. 4.4 – 4.6, the asymmetry parameter  $q$  relates the semi-principal axes

of the ellipsoid and thus quantifies the deformation of the planet. Maximum deformation (hence maximum  $q$ ) is attained for a given planet when it orbits at the stellar Roche radius  $R_{\text{Roche}}$ . Similar to Eq. 3.2, the Roche radius can be re-written for the star as

$$R_{\text{Roche}} = 2.46 R_* \left( \frac{\rho_*}{\rho_p} \right)^{1/3} = 2.46 R_v \left( \frac{M_*}{M_p} \right)^{1/3}. \quad (4.8)$$

Substituting  $a = R_{\text{Roche}}$  in Eq. 4.7 gives

$$q_{\text{max}} = \frac{h_f}{2 \times 2.46^3}. \quad (4.9)$$

Therefore, for a homogeneous body with  $h_f = 2.5$ , we have  $q_{\text{max}} \simeq 0.0839$ . The equilibrium shape of a planet therefore depends on its radius, its second fluid Love number  $h_f$ , planet-to-star mass ratio planet  $M_p/M_*$ , and also the distance from the planet to the star,  $a$ . Figure 4.2 shows how tidal deformation becomes negligible with distance from the star (in units of its Roche radii) for a given body with  $h_f = 2.5$  and Jupiter-like  $h_f = 1.5$ . We see that far away from the star, irrespective of the value of  $h_f$ , the planet does not deform ( $q \simeq 0$ ) and so its shape remains largely spherical ( $r_1 \simeq r_2 \simeq r_3$  from Eqs. 4.4–4.6). In general, Eq. 4.7 shows that tidal deformation is more relevant for large planets orbiting very close to the Roche radii of their stars.

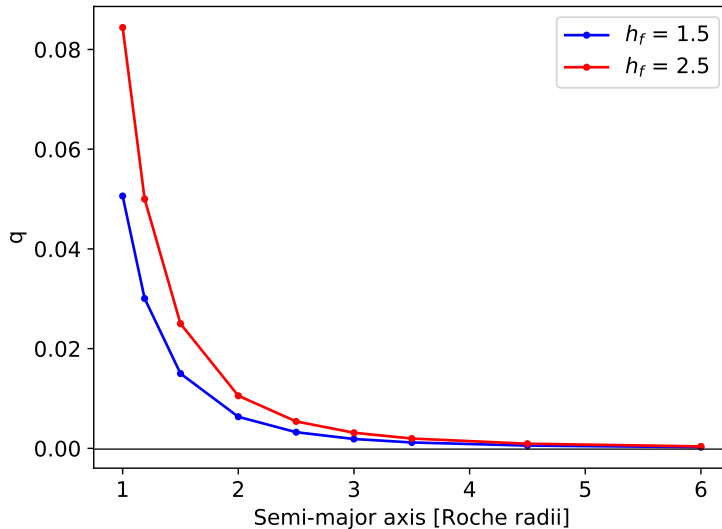


Figure 4.2: Quantification of tidal deformation as a function of distance to the star for two different  $h_f$  values.

### 4.3.2 Identifying suitable candidates for deformation

The radial deformation  $\Delta R$  of a planet is calculated as the difference between the longest semi-axis of the ellipsoid ( $r_1$ ) and its volumetric radius  $R_v$ . Using Eq. 4.5 we have that:

$$\begin{aligned}\Delta R &= r_1 - R_v \\ &= R_v (1 + 7q/3) - R_v \\ &= R_v \times 7q/3.\end{aligned}\tag{4.10}$$

Similarly, the percentage radial deformation of a planet can be obtained from

$$\mathcal{D}_R = \Delta R/R_v \times 100\%.\tag{4.11}$$

Planets with the highest  $\Delta R$  will provide the best chance at detecting deformation. Therefore, Eq. 4.10 can be used to identify the planets expected to be significantly deformed. To this end, parameters for confirmed exoplanets were obtained from NASA Exoplanet Archive<sup>1</sup>. Taking the quoted radius for each planet as the volumetric radius of the ellipsoid  $R_v$  and assuming  $h_f = 1.5$ , the values of  $q$ ,  $\Delta R$ , and  $\mathcal{D}_r$  were calculated. Table 4.1 shows the planets with  $\mathcal{D}_R > 5\%$ . As expected, the largest deformation is obtained for close-in planets. Their orbital distances range from 1.01 – 1.4 times the Roche radius of their stars. The detectability of tidal deformation in these targets will depend on their induced amplitudes and the precision of their transit observations.

### 4.3.3 Transit model

To model the transit light-curve of a deformed planet, it is necessary to have a transit model that accurately projects the ellipsoidal planet onto the sky-plane, calculates the overlap area between the planet and the star, and then return the integrated flux as a function of time. The `ellc` transit tool (Maxted, 2016) was found to be ideal for this purpose. It was originally developed to generate and analyse the light-curves of eclipsing binaries or transiting planets allowing different non-spherical shapes for the objects. Given its appropriateness, I modified `ellc` to incorporate the above shape model by Correia (2014) as a new subroutine in FORTRAN but accessed with python functions calls. The modified version<sup>2</sup> allows the generation of transit light-curve of a tidally deformed planet parameterised by the Love number.

<sup>1</sup><https://exoplanetarchive.ipac.caltech.edu/>

<sup>2</sup>Available on github [github.com/tundeakins/ellc](https://github.com/tundeakins/ellc)

Table 4.1: Confirmed planets with expected radial deformation greater than 5%. WASP-103b is highlighted to ease referencing.

Planet	$P$ [d]	$m_V$	$i_p$ [ $^\circ$ ]	b	$R_v$ [ $R_J$ ]	$R_v$ $R_*$	$M_p/M_*$	$a/R_*$	$a/R_{\text{Roche}}$	q	$\Delta R$	$\mathcal{D}_R$ [%]
<sup>(1)</sup> WASP-12b	1.09	11.6	83.52	0.34	1.937	0.120	0.00098	3.005	1.01	0.049	0.0136	11.4
<sup>(2)</sup> WASP-19b	0.79	12.2	78.78	0.68	1.392	0.143	0.00113	3.514	1.04	0.045	0.0149	10.4
<sup>(3)</sup> WASP-121b	1.27	10.5	87.6	0.16	1.865	0.131	0.00084	3.747	1.09	0.039	0.0118	9.0
<sup>(4)</sup> WASP-103b	0.93	12.4	88.2	0.09	1.596	0.116	0.00116	3.012	1.11	0.037	0.0100	8.6
<sup>(5)</sup> HAT-P-32b	2.15	11.4	88.98	0.08	1.98	0.149	0.00057	5.332	1.21	0.028	0.0098	6.6
<sup>(6)</sup> WTS-2b	1.02	16.0	83.55	0.58	1.363	0.187	0.00130	5.318	1.26	0.025	0.0109	5.8
<sup>(7)</sup> WASP-76b	1.81	9.5	88	0.14	1.83	0.109	0.00060	4.102	1.29	0.023	0.0059	5.4
<sup>(8)</sup> HAT-P-65b	2.61	13.1	84.2	0.46	1.89	0.104	0.00042	4.568	1.33	0.022	0.0053	5.0

References: (1)Chakrabarty and Sengupta (2019); (2)Wong et al. (2016); (3)Delrez et al. (2016); (4)Southworth and Evans (2016); (5)Wang et al. (2019); (6)Birkby et al. (2014); (7)West et al. (2016); (8)Hartman et al. (2016).

The projected shape of the ellipsoid on the stellar disk is an ellipse whose dimensions vary due to rotation of the ellipsoid with phase (*see* Fig. 4.3). Therefore, the projected area (cross-section) of the planet varies during transit. It should be noted that the shape correction model by Budaj (2011) does not account for the varying ellipsoidal cross-section during transit. This observational effect thus makes our transit model a more complete model in extracting the planet shape from transit observations.

In addition to the usual transit parameters described in Section 2.2, the modified transit model includes  $h_f$  and the planet-to-star mass ratio  $M_p/M_*$  as inputs. Furthermore, the radius of the planet is replaced with the ellipsoid’s volumetric radius  $R_v$ . Therefore, by fitting the ellipsoidal planet model to the transit observation, all the parameters of the transit can be obtained, including the shape of the planet. In particular, rather than obtaining the usual transit radius  $R_{\text{spr}}$  from spherical planet models, we instead obtain  $R_v$  and  $h_f$  which are used to calculate the ellipsoidal planet dimensions  $r_1, r_2, r_3$  (from Eqs. 4.3–4.6) that provides the best fit to the observation. In fitting the ellipsoidal model, estimates of the stellar and planetary masses are required which can be obtained from e.g., asteroseismology and RV observations, respectively. Actually from RV observations, we only obtain  $M_p \sin i_p$  (see Eq. 1.3) but the ellipsoidal model transit fit can estimate  $i_p$  within each iteration to obtain the true planet-to-star mass ratio.



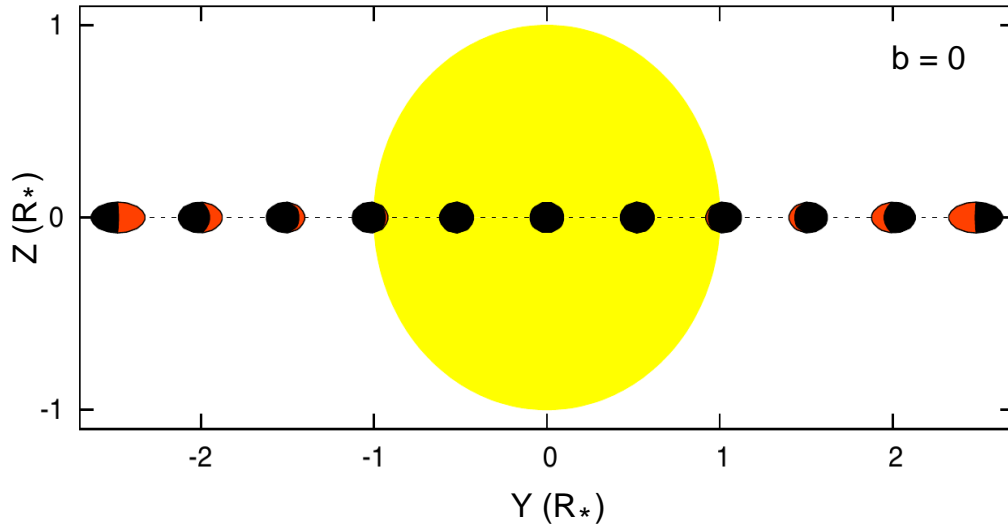


Figure 4.3: Illustration of the varying projected area of the ellipsoid with phase. Image adapted from Correia (2014).

#### 4.3.4 Test case: WASP-103 b

To illustrate the capability of `e11c` to generate transit light-curves of ellipsoidal planets, I take the case of WASP-103 b. It is an ultra-hot Jupiter ( $P = 0.925$  d) reported to be on the edge of tidal disruption (Gillon et al., 2014) which makes it an ideal candidate to detect deformation. The parameters of WASP-103 b, according to Southworth and Evans (2016), are given in Table 4.1. It is assumed to be on the edge of tidal disruption due to its semi-major axis of only 1.1 times its stellar Roche radius. Taking the quoted radius as the volumetric radius of the ellipsoid, I simulated the light-curve of the ellipsoidal planet for different values of  $h_f$  and compare it to the spherical planet light-curve with the same parameters. Quadratic LDCs of  $u_1, u_2 = 0.5393, 0.1299$  were obtained for the visible band using LDTk with stellar parameters given in Gillon et al. (2014).

The comparison of the different simulated light-curves is shown in Fig. 4.4a. We see that the light-curve of the ellipsoidal model changes noticeably for different values of  $h_f$  and also compared to the spherical case. The ellipsoidal planet transits are different from the spherical case because only a small cross-section of the ellipsoidal planet is projected during transit which leads to shallower transit. Figure 4.4b shows the projected area of the planets normalised to the area of the spherical planet. The projected area of the

ellipsoid varies during transit and is smaller than that of the spherical planet of the same volume. The maximum projected area of the ellipsoid during transit occurs just after ingress (second contact) after which the area reduces towards mid-transit due to the long semi-axis  $r_1$  being rotated away (Fig. 4.3). The mid-transit phase has the smallest ellipsoidal cross-section of  $r_2 r_3 \simeq R_v^2 (1 - 7q/3)$  which is less than the cross-section  $R_{\text{spr}}^2$  if the planet were spherical. Therefore, if a spherical planet model is used to fit the transit light-curve of an ellipsoidal planet, the spherical radius  $R_{\text{spr}}$  derived will be smaller than the actual volumetric radius  $R_v = (r_1 r_2 r_3)^{1/3}$  of the ellipsoid in order to match the lower transit depth (see Fig. 4.5). This is in agreement with the result from Leconte et al. (2011) thereby validating the deformed planet light-curve generated with the modified `ellc`. The difference in transit depth as  $h_f$  varies in Fig. 4.4 is due to the fact that higher  $h_f$  for the same planet causes more deformation, which leads to an even smaller projected area.

The modified `ellc` allows for a case where  $h_f = 0$  to imply no deformation to the planet. In such a case, the ellipsoidal planet model is equivalent to that of a spherical planet and they produce the same light-curve with  $R_v = R_{\text{spr}}$ . This is useful because it allows the use of the same model to explain both a deformed and a spherical planet. As seen in Fig. 4.4, the ellipsoidal light-curve when  $h_f = 0$  is the same as the spherical planet light-curve generated using `batman`.

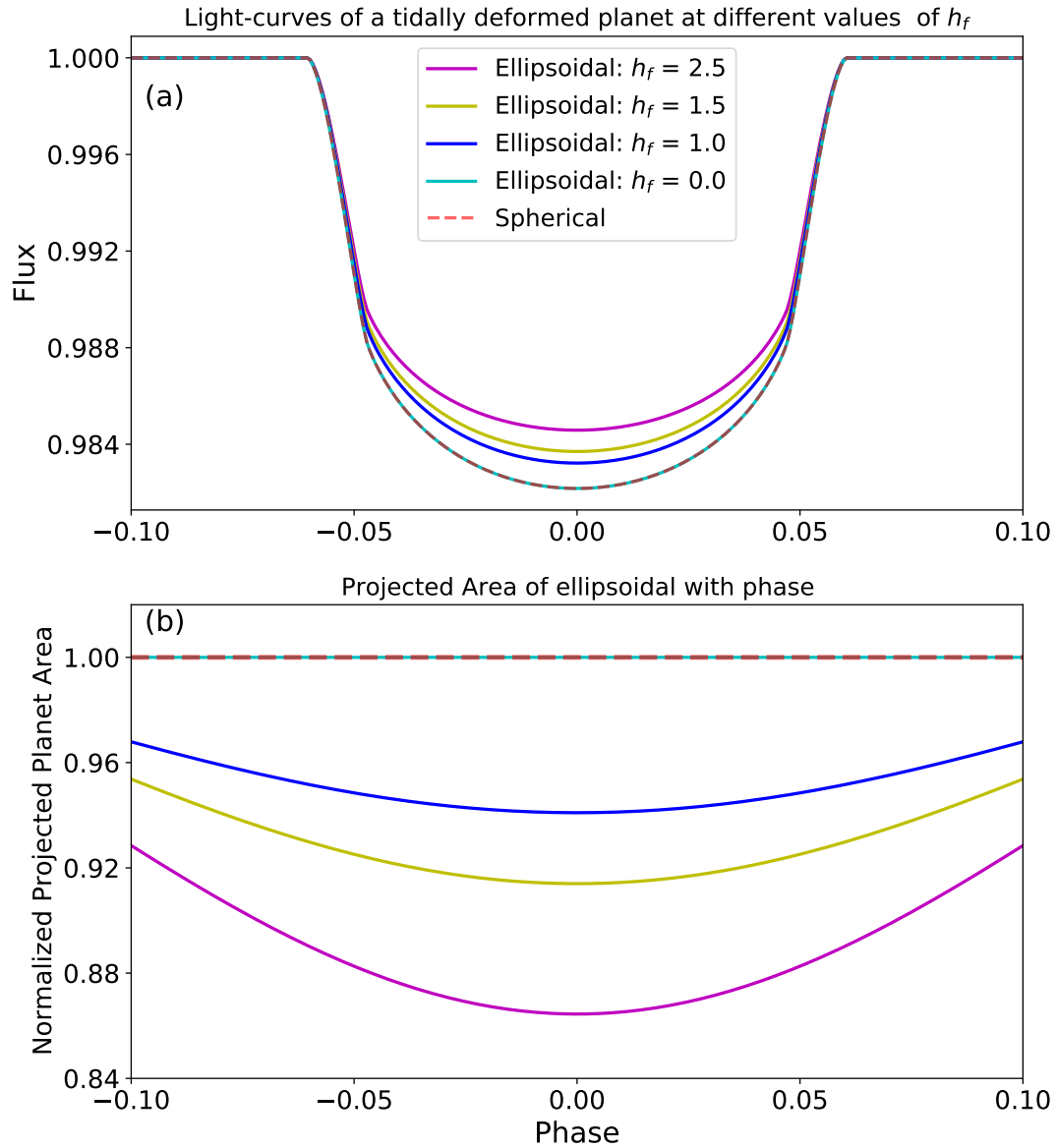


Figure 4.4: **(a)**: Comparison of ellipsoidal model light-curves of different  $h_f$  values with spherical model light-curve for WASP-103b. **(b)**: Normalised projected area of the planet as a function of orbital phase.

### 4.3.5 The signature of deformation in transit light-curves

Following the illustrative example in defined in Chapter 2, the observable signature of planet deformation is the residual between the deformed planet’s light-curve and the best-fit spherical model. To show the signature of deformation, the light-curve of deformed WASP-103b was simulated using the ellipsoidal model with parameters given in Table 4.1 and  $h_f = 1.5$ . A chi-square fit to the simulated light-curve is then performed using a spherical planet model.

The result of the fit is shown in Fig. 4.5. The spherical planet parameters derived from the fit (shown in the plot labels) are systematically incorrect as they adjust to mimic the signature of deformation. In this case, using a spherical planet model leads to underestimation of the true radius by 4% which leads to overestimating the density by 12%. However, the assumption of sphericity for a deformed planet affects not only the derived radius but also the other transit parameters, and models that adjust only the radius and density (e.g. Budaj, 2011; Burton et al., 2014) are incomplete.

The residuals from fit show that the signature of deformation manifests in two regions. The first is at ingress (and egress) owing to oblateness ( $r_2 > r_3$ ) of the planet as identified in previous studies (e.g. Seager and Hui, 2002; Barnes and Fortney, 2003). This occurs because the deformed planet begins transit before the fitted spherical planet and they block different amounts of stellar light during ingress (and egress) phases. A second prominent feature is seen as a bump centred on the mid-transit phase due to the varying star eclipsed area caused by the rotation of the ellipsoid as it transits (Fig. 4.4b). This second feature is as a result of tidal deformation which was not accounted for in the previous studies mentioned but manifests in our model due to full projection of the ellipsoidal shape as it rotates with phase (Correia, 2014).

I perform the same spherical fit to the deformed light-curve of the planets in Table 4.1. The residuals are shown in Fig. 4.6. We see that the amplitude of deformation is just around 50 ppm for the best-case scenarios. WASP-103 b, WASP-12 b and WASP-121 b have the largest amplitudes and thus present the best possibility of detecting tidal deformation.

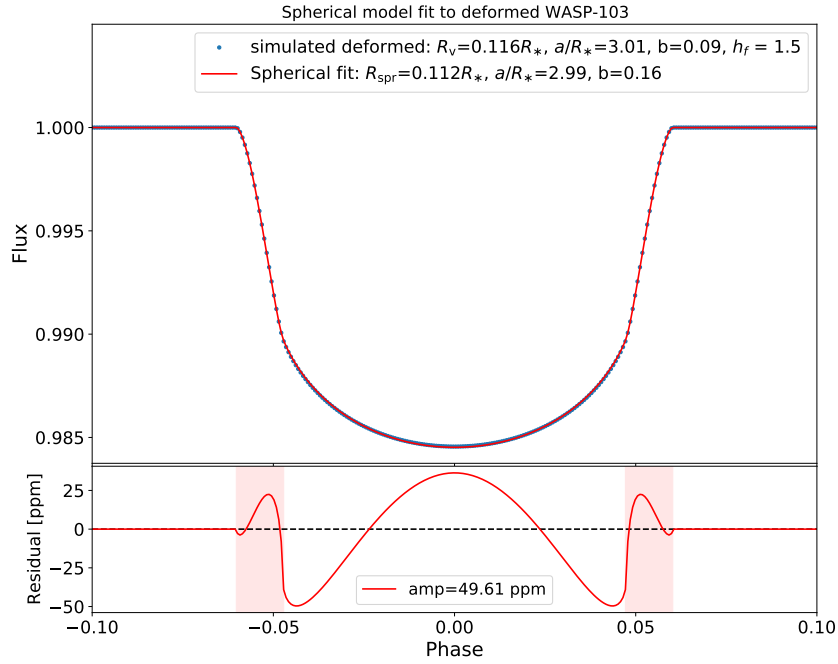


Figure 4.5: Spherical planet model fit to the simulated light-curve of deformed WASP-103b. The residuals represent the signature of tidal deformation in this planet with amplitude (amp) quoted as the maximum absolute residual. The shaded regions in the residual plot indicate the transit ingress and egress phases.

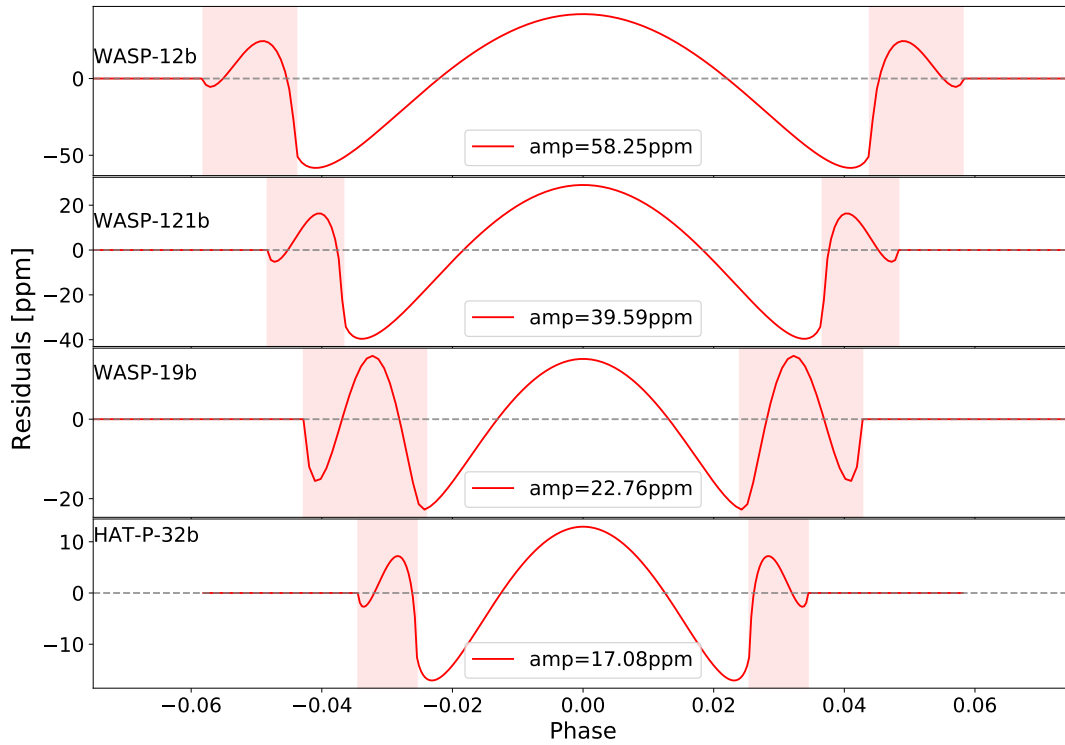


Figure 4.6: Deformation signature and amplitude of different short-period planets.

## 4.4 Detectability of planet deformation and measurement of planet Love number

The residuals of the spherical model fit to the light curve of a deformed planet is informative in detecting deformation as it reveals that the spherical model does not fully explain the observation. However, some of the deformation-induced effects have been absorbed into the fit since the spherical model attempts to adjust its parameters to better fit the data. Therefore, to correctly estimate the planet transit parameters, the ellipsoidal model can be used to fit the transit observation. In doing so, one obtains a value for the Love number that best fits the observation, if there is enough precision in the data. The benefit of this approach is that we can fit the ellipsoidal model to any transit observation and, by the value of  $h_f$  recovered, ascertain if planet deformation is detectable or not. If we cannot detect the deformation or the planet is not deformed, we get  $h_f \approx 0$  which as shown in Fig. 4.4 is equivalent to the fit of a spherical planet model.

Therefore, detectability of tidal deformation using the ellipsoidal model relies on the ability to recover a non-zero value of  $h_f$  with statistical significance from a fitting process. Despite being able to infer deformation with the detection of  $h_f \gg 0$ , it is necessary to have  $h_f \geq 1$  with some significance where the values give actual physical interpretation to planets.

To illustrate the detectability, the transit light-curve of deformed WASP-103b was again simulated with one-minute cadence using its parameters from Table 4.1 with  $h_f = 1.5$  and same quadratic LDCs as before. Gaussian noise of different levels was added to the simulated data to emulate separate observations with different photometric precisions. I then investigated how well the value of  $h_f$  can be recovered and at what noise level it would be impossible to distinguish between the light-curve of a spherical planet and that of a deformed planet. This is important to know the instrumental precision required to detect deformation in close-in planets.

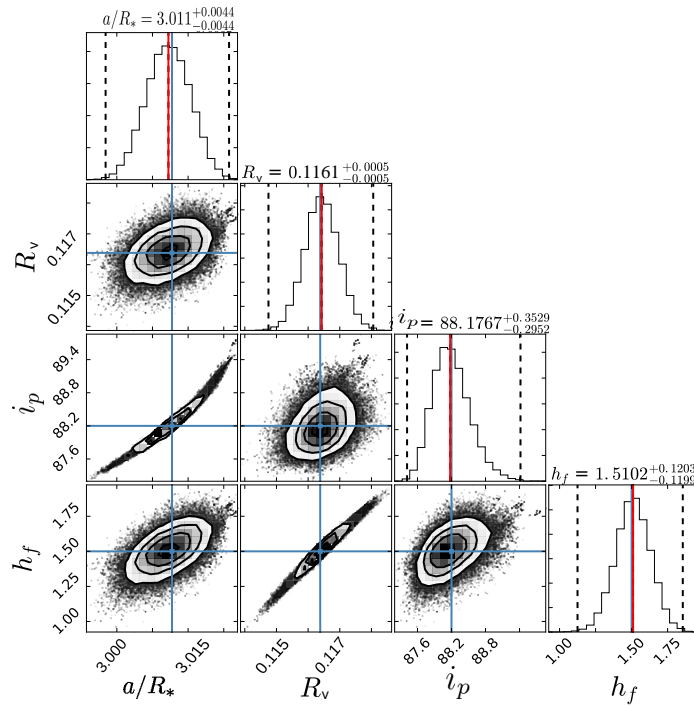
An MCMC was performed to estimate the transit parameters and their uncertainties using `emcee`. The prior distributions on the model parameters are given in Table 4.2. The LDCs are kept fixed here while in the next section the impact of limb darkening is assessed by varying the LDCs. The corner plot in Fig. 4.7 shows the posterior distribution of the parameters when noise levels of 30 ppm and 100 ppm are added to the simulated observation. Fig. 4.7a shows that at a noise level of 30 ppm,  $h_f$  is accurately recovered and

Table 4.2: Adopted priors in MCMC fit of simulated light-curve of deformed WASP-103 b. The quadratic LDCs,  $u_1$  and  $u_2$ , are fixed.

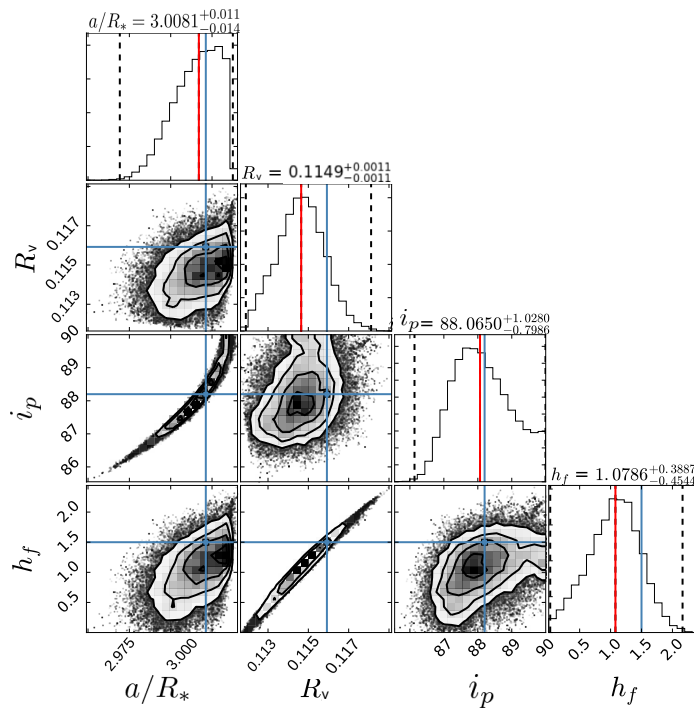
Parameters	Value	Prior
$R_v [R_*$ ]	0.116	$\mathcal{U}(0.05, 0.15)$
$a/R_*$	3.012	$\mathcal{U}(2.5, 3.5)$
$i_p [^\circ]$	88.2	$\mathcal{U}(70, 90)$
$h_f$	1.5	$\mathcal{U}(0, 2.5)$
$u_1$	0.5343	–
$u_2$	0.1299	–

with  $\sim 3\sigma$  significance above 1, indicating that the planet is indeed deformed. However, at a noise level of 100 ppm the median of the distribution suggests a deformed planet, but because its width encompasses  $h_f = 0$  (spherical model), planet deformation cannot be asserted (Fig. 4.7b). In both corner plots, a very strong positive correlation is seen between  $R_v$  and  $h_f$  and this is due to the fact that a higher  $h_f$  leads to more deformation and a shallower transit so  $R_v$  increases to compensate for the observed transit depth. Breaking the degeneracy between these parameters requires precise transit observations.

Figure 4.8 shows the detectability plot summarising the results for the different noise levels added to the observation. We see that the significance of  $h_f$  detection above 1 reduces as the noise level of the observation increases. For instance, at 50 ppm noise level,  $h_f$  samples are well above zero, implying that the ellipsoidal model provides a better fit than the spherical model. However, the samples with  $h_f < 1$  do not represent physical values for a planet expected to be in hydrostatic equilibrium but the detection still gives  $\sim 95\%$  of the samples above 1. Beyond 50 ppm, fitting the observation with a spherical model becomes increasingly more probable. With noise levels as high as 100 ppm, the spherical and ellipsoidal models produce comparable fits.



(a)



(b)

Figure 4.7: Posterior distributions of parameters of the simulated deformed WASP-103 b. (a): with 30ppm/min noise added. (b): with 100ppm/min noise added. Red lines indicate the median for each parameter posterior while the blue lines indicate the simulated values. Dashed lines indicate the 68% credible intervals.



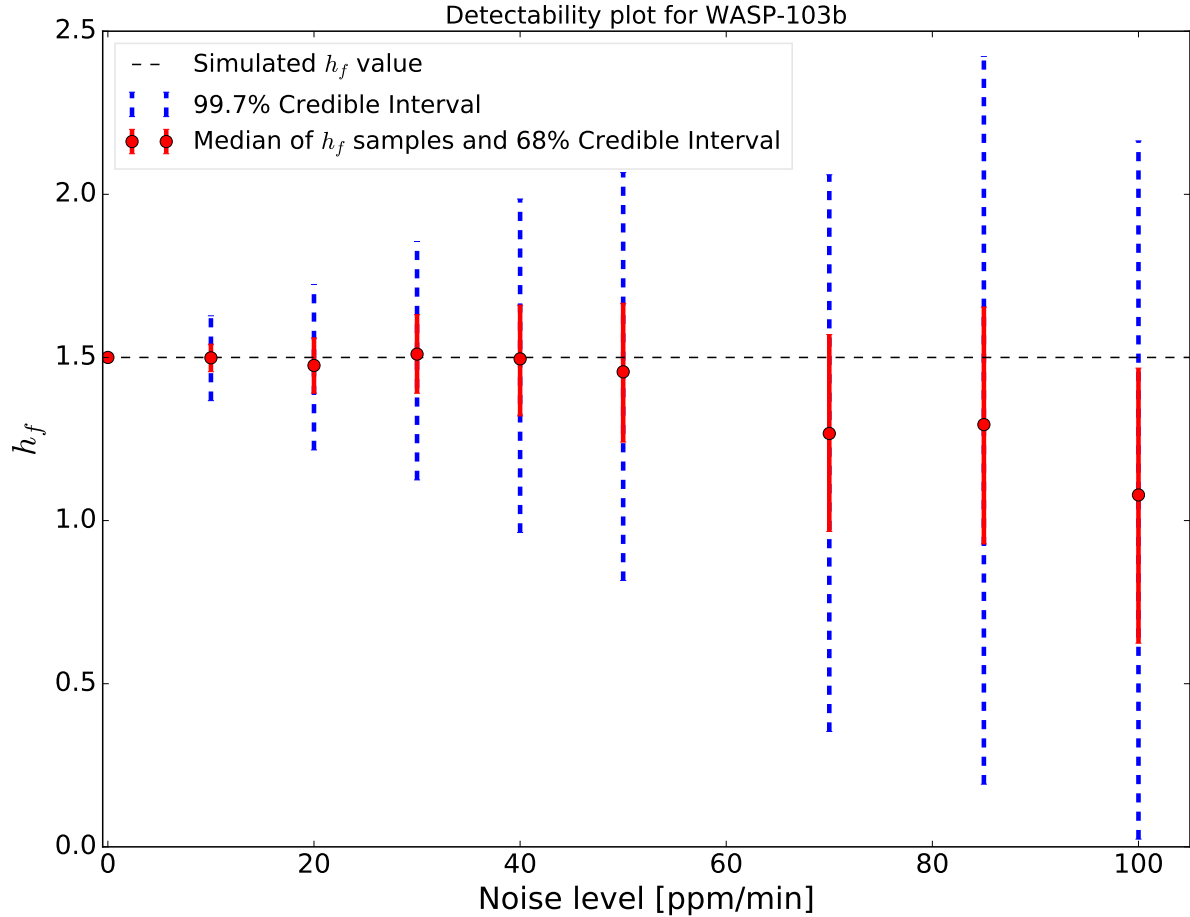


Figure 4.8: Detectability of deformation in WASP-103b considering different noise levels. The black dashed line is the simulated  $h_f$  value. The points are the median of the  $h_f$  samples at each noise level. The red error bars indicate the 68% credible interval ( $\simeq \pm 1\sigma$ ) while the blue error bars indicate the 99.7% credible interval ( $\simeq \pm 3\sigma$ ).

## 4.5 Discussion

The results show that noise levels below 30 ppm offer the best chance at detecting deformation for our test case of WASP-103b since we retrieve  $h_f$  with  $\geq 3\sigma$  significance above 1. However at 50 ppm, 84% of the recovered  $h_f$  samples are still in physical values expected for planets in hydrostatic equilibrium. Therefore, we could set this as a more relaxed detection limit for deformation in this planet.

A photometric precision of 50 ppm/min is not yet attainable using current observational instruments. Table 4.3 compares the photometric precision attainable by *CHEOPS* and *PLATO* for stars of different magnitudes. For our case system, WASP-103 is a twelfth-magnitude star and the theoretical photometric precision of *CHEOPS* for this

star is 855 ppm/min. Attaining a reduced photon noise level of 50 ppm/min for this star using *CHEOPS* requires  $\sim 293$  transit observations of WASP-103b. For WASP-121b, whose deformation can also be detected at 50 ppm/min noise level, *CHEOPS* precision for its tenth magnitude star is 319 ppm/min (Table 4.3) thereby requiring only 40 transit observations to detect its deformation. Although information from the *CHEOPS* consortium indicates that WASP-121 might not be in the visibility region, new interesting planet candidates with short period orbits may still be detected by *TESS* or found in future surveys targeting bright stars, such as *PLATO*. For these planets around stars brighter than  $m_V = 9$ , photon noise levels as low as 150 ppm/min can be expected with *CHEOPS* and  $< 62$  ppm/min with *PLATO* (Table 4.3) and thus require fewer transits to reach the 50 ppm limit needed to detect planet deformation.

Even for the brightest stars, *TESS* has photometric precisions  $> 464$  ppm/min<sup>3</sup> which is not sufficient for detecting deformation. Observations with the forthcoming *JWST* will be immensely beneficial as it is expected to attain photon-noise floor below  $\sim 60$  ppm on its NIRCam and NIRSpec instrument amongst others (Beichman et al., 2014). Attainment of this noise level implies that only one transit observation will be required in order to detect tidal deformation in a suitable short-period planet. Unfortunately, interesting short-period planets expected to be significantly deformed were not found within the original *Kepler* survey field which would have provided several transit observations of any found target. The WFC3 instrument on the *HST* achieved a noise level of 172 ppm (103 secs) for observations of WASP-103 (Kreidberg et al., 2018). Therefore, with  $< 15$  transits of WASP-103b using *HST*, the required precision of 50 ppm/min can be attained.

Different astrophysical or observational factors can still affect the detectability of deformation, some of which are mentioned below.

### Temporal resolution

The above analysis was performed using one-minute cadence for the simulated observations to enable good resolution of the ingress and egress phases which have short durations especially for these short-period planets. A longer cadence than this reduces the precision with which  $h_f$  and other parameters are recovered if there are no sufficient points within the ingress/egress phases. A longer cadence however allows for longer exposures which improves the precision of the observations and can favour detecting deformation.

---

<sup>3</sup><https://heasarc.gsfc.nasa.gov/cgi-bin/tess/webtess/wtv.py>

Table 4.3: Number of transits required to reach 50ppm/min noise level with *CHEOPS* and *PLATO* for different stellar magnitudes. Noise levels of *CHEOPS* were obtained from *CHEOPS* science team (or at this [link](#)) and that for *PLATO* was converted to ppm/min from Rauer et al. (2014)

CHEOPS			PLATO		
$m_V$	Noise/min	# transits	$m_V$	Noise/min	# transits
6.5	150 ppm	9	8	62 ppm	2
8	186 ppm	14	10	209 ppm	17
10	319 ppm	40	11	263 ppm	28
12	855 ppm	293	13	619 ppm	153

A trade-off has to be made between temporal resolution and the required precision. Observations with 2-minute exposure time or binning still allows proper retrieval of  $h_f$  with comparable precision whereas longer exposures smear out the deformation signal making the detection challenging.

### Orbital inclination

The inclination of the orbit plays a role in the signature of deformation. Lower inclinations indicate a shorter transit duration so the effects referred to in residuals of Fig. 4.5 and § 4.3.5 will be shorter in time, making them more difficult to temporally resolve, especially at the ingress and egress phases. In addition, a longer transit duration allows the projected ellipse area to vary more (longer phase rotation of ellipsoid) making the light-curve more markedly different from that of the spherical planet thereby leading to a higher-amplitude bump around mid-transit (*see also* Fig. A.1 in Correia 2014). The effects of deformation in light curves is maximal at an inclination of  $90^\circ$  where  $h_f$  is recovered with the best precision.

### Effects of limb darkening

As shown in Fig. 4.5, the signature of deformation is prominent at ingress and egress phases with a bump centred around the mid-transit phase. The stellar limb-darkening affects light curves similarly in these regions as we saw in Chapter 2 so it is important to investigate its impact on detection of tidal deformation. Limb darkening has been shown to affect parameter estimates depending on how they are treated in the fitting procedure (see e.g. Espinoza and Jordán, 2015; Neilson et al., 2017; Csizmadia et al., 2019). Common methods involve either fixing the LDCs to theoretical values from stellar inten-

sity profiles from atmospheric modelling or fitting them with the other transit parameters (usually with priors based on the theoretical values). Therefore, I investigated the impact of the LDCs on the recovery of  $h_f$  from the light curve. This test was performed using the 50 ppm noise level simulation in two ways and the results are summarised in Table 4.4.

First, the LDCs are fixed to incorrect values that are slightly different from the true values used to generate the simulated observation. Fixing the LDCs to incorrect values that are smaller than the true values results in a damping of the deformation signal and lower  $h_f$  values than those simulated are recovered. When the values are fixed at values up to 0.01 smaller than the true values, the entire  $h_f$  distribution is consistent with zero and a spherical planet shape is inferred. On the other hand,  $h_f$  values are amplified when LDCs are fixed at values higher than the true values. For LDC values fixed at 0.015 higher than the true values, the recovered  $h_f$  distribution is one-sided with its peak at the maximum  $h_f$  value of 2.5. In the latter case, we can probably infer that the planet is deformed but cannot ascertain the extent of deformation due to inaccurate estimation of  $h_f$ . The result from fixing the LDCs implies that wrong values can prevent the detection of tidal deformation. In practice, fixing the LDCs are discouraged (see arguments in e.g. Csizmadia et al., 2012; Espinoza and Jordán, 2016; Csizmadia, 2018) since it is necessary to propagate the uncertainties (or ignorance) of the stellar intensity profiles to the other parameters. Furthermore, different theoretical values for the LDCs can be obtained from the different methods of fitting the stellar model intensity profiles making it difficult to choose the accurate LDCs.

The other attempt was include the LDCs in the fitted parameters to the 50 ppm noise level simulation. I adopt Gaussian priors centred on the true LDC values and a width of  $\sigma = 0.01$ . The posterior shows a wide  $h_f$  distribution centred close to the true value but with a large width of  $\sim 0.4$  (Fig. 4.9a) making it difficult to ascertain planet shape even though it suggests deformation. A correlation can be seen between  $h_f$  and  $u_1$  which is perhaps responsible for long tail towards lower  $h_f$  values. However, when tighter priors (e.g., the derived uncertainties on the LDCs from LDTk) are imposed on the LDCs,  $h_f$  is well-recovered to strongly infer deformation (Fig. 4.9b). The result from the fitting the LDCs reveals that there exists a correlation between the LDCs and  $h_f$  such that precise priors on the LDCs will enhance the estimation of  $h_f$ . Therefore it is necessary to obtain the best possible theoretical estimate of the LDCS in order to detect tidal deformation.

To combat the poor outlook of fitting with quadratic LDCs, other limb darkening

Table 4.4: Results of LDC tests and  $h_f$  values recovered.

LDC tests	Values $[u_1, u_2]$	$h_f$ recovered
Fixed at 0.01 below	$[0.5243, 0.1199]$	$0.12^{+0.11}_{-0.08}$
Fixed at 0.015 higher	$[0.5493, 0.1449]$	$2.44^{+0.04}_{-0.06}$
Gaussian priors	Mean= $[0.5343, 0.1299]$ , $\sigma=[0.01, 0.01]$	$1.56^{+0.34}_{-0.51}$
Gaussian priors	Mean= $[0.5343, 0.1299]$ , $\sigma=[0.0012, 0.0027]$	$1.59^{+0.16}_{-0.17}$

laws (defined in §1.2.2) can be used. It has been shown that the quadratic law is unable to model the complex intensity profile observed in stars (Espinoza and Jordán, 2015; Kipping, 2016; Maxted, 2018). The non-linear law (four parameter law Eq. 1.14) is the most accurate law to describe limb darkening but its several parameters makes it challenging to use in fitting procedures. Alternatively, the power-2 limb darkening law (Eq. 1.13) has been recommended for the analysis of transit light curves as it has been shown to provide remarkable agreement between stellar atmospheric models and observations, particularly for cool stars (Morello et al., 2017; Maxted, 2018). The transformation of the two parameters of the power-2 law in Maxted (2018) minimises the correlation between them which allows faster sampling during fitting and provides better parameter estimates. The fitting process can attempt different LDC laws so that the law with the best match to the observation and that produces the least errors on the derived parameters will be preferred. Certainly, a model comparison approach between the adopted limb darkening laws would be useful in selecting the most appropriate one.

Observations at longer wavelengths where the impact of limb darkening is minimised will dramatically favour detection too. In this sense, combining the expected precision of *JWST* and observation in the infrared will provide the best opportunity for measuring  $h_f$  in the near future.

### Other noise sources

Our simulations considered the ideal situation where only photon (white) noise is present thereby allowing easy scaling of the noise with the number of observations/transits. However, in practice, other sources of noise (Pont et al., 2006) will impact the estimates given above and act to increase the number of transits required to detect deformation. These other noise sources can be from instrumental effects (e.g., satellite jitter and thermal instability) and also from astrophysical sources such as stellar activity (occulted

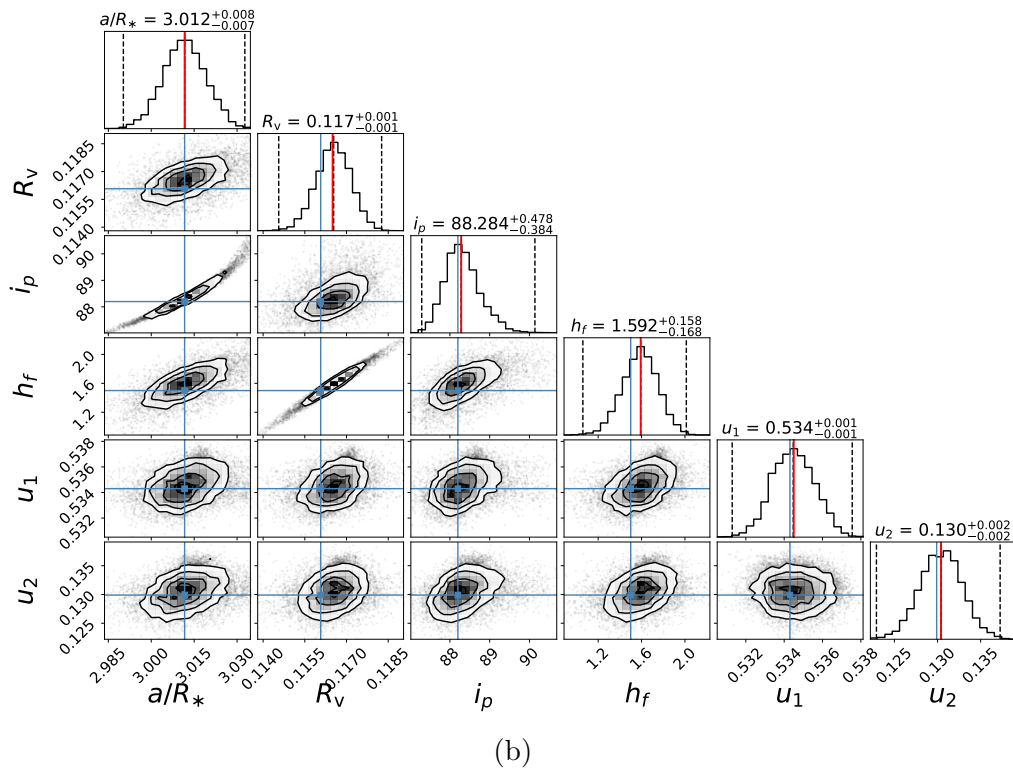
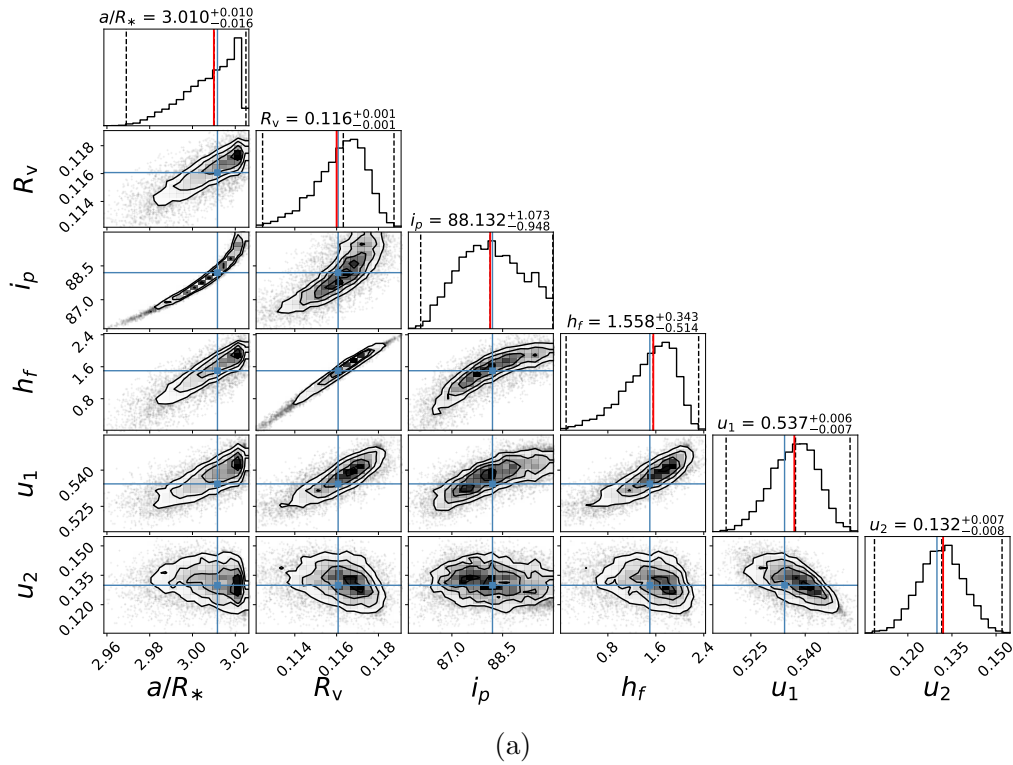


Figure 4.9: Posterior distributions of parameters when fitting the LDCs. (a): with Gaussian priors of width  $\sigma=0.01$  on the LDCs. (b): with Gaussian priors of tighter width from LDTk.

or unocculted active regions Oshagh et al. (2013a)), stellar oscillations and granulation (Chiavassa et al., 2017). These effects always have to be mitigated in transit analysis (Oshagh, 2018b; Barros et al., 2014a) but will still impact the detectability of shape deformation. Recent developments in Gaussian process analysis also provide a method for tackling astrophysical noise (e.g., Foreman-Mackey et al. 2017; Faria et al. 2020; Pereira et al. 2019).

## 4.6 Summary and related works

Short-period planets, especially within two Roche radii from the host star, suffer from extreme tidal forces causing their shapes to depart from sphericity in a way that is difficult to detect in transit observations. With the increasing observational precision of near-future instruments, detecting deformation becomes more feasible as planet shape will have a higher impact on the observed transit light curves. I demonstrated the detectability of deformation for WASP-103b, which is one of the most deformed planets, but found that accurate treatment of limb darkening is necessary to reliably detect deformation. As Love number describes how a planet deforms in response to perturbing potentials, it was used as a measure of deformation in the planet. Detecting and measuring planet deformation provides more accurate estimations of the radius and density of these planets as opposed to the estimates derived from spherical models or corrections calculated from only expectation of deformation. Additionally, measuring the Love number provides information about the interior structure of the planet which Baumeister et al. (2020) showed allows to rule out several possible interior models for a planet.

Furthermore, the analysis showed that the instrumental precision needed to detect tidal deformation is  $\leq 50$  ppm which can be attained by *CHEOPS* with about 293 transits for WASP-103b and 15 transits by *HST*. More recent estimates using larger planetary radius and planet-to-star ratio measurements from obtained by Delrez et al. (2018) increases the expected amplitude of deformation signature to  $\sim 60$  ppm (from 49 ppm showed in Fig. 4.5). This reduces the the number of transits required to detect it. For instance, the required number of *CHEOPS* transit observations reduces to 190.

As part of the *CHEOPS feature.characterisation* working group, we have obtained several transits of WASP-103b to test the possibility of detecting its deformation. The actual observations reveal that we indeed need a large number of transit observations. However, our recent efforts combine the available *CHEOPS* transit with high precision

transits from *Spitzer* and *HST* which significantly improves our chances of detecting the deformation. We submitted a *JWST* proposal to observe WASP-103 b but it was unfortunately not granted.

It is worth mentioning that a recent work by Hellard et al. (2020) used two transit observations from the *HST/STIS* to place weak constraints of  $1.39 \pm 0.8$  on the  $h_f$  value of WASP-121 b. This was done by measuring the same deformation signal described in this work from the light-curves. They add that further observations are necessary for better constrain  $h_f$ . This further goes to show the possibility of measuring the deformation from very precise light-curves.



# Chapter 5

## Exoplanetary Oblateness

Planets attain non-spherical equilibrium shapes as a result of different forces acting upon them such as tidal and centrifugal forces. In Chapter 4, we saw that the effect of tidal deformation is most significant for tidally-locked close-in planets. For fast rotating planets, the centrifugal acceleration is more dominant causing a reduction of the effective gravitational acceleration at the equator compared to the pole. This leads to an equatorial bulge referred to as oblateness (Seager and Hui, 2002). It is possible to probe the planet oblateness from transit observations as they can cause observable deviations from standard transit signals.

This chapter deals with the measurement of exoplanet oblateness from transit observations. First, I introduce the relevance of measuring oblateness and then describe the transit tool adopted for modelling the transit light-curve and RM signal of oblate planets. Afterwards, I validate the tool by confirming results from previous photometric studies and then show the effect of oblateness on RM signals. Furthermore, I compare the detectability of oblateness from RM signals to that from light-curves and then discuss the prospects of combining both measurements for a more precise measurement of oblateness. The capability of different observing instruments for detecting oblateness is also investigated. Finally, I identify some interesting targets and probe for oblateness in their transit light-curves.

This chapter was originally published<sup>1</sup> as: **Akinsanmi, B.**, Barros, S. C. C., Santos, N. C., Oshagh, M., & Serrano, L. M.; *Constraining the oblateness of transiting exoplanets with photometry and spectroscopy*; *MNRAS*, 497, 3, 3484 (2020).

---

<sup>1</sup>Ongoing work on probing oblateness in confirmed planets is however briefly presented in the last section (§5.6)

## 5.1 Introduction

The oblateness of a body is defined by the flattening (or oblateness) parameter  $f$  which is defined as (e.g., Barnes and Fortney 2003; Carter and Winn 2010a)

$$f = \frac{R_{eq} - R_{pol}}{R_{eq}}, \quad (5.1)$$

where  $R_{eq}$  and  $R_{pol}$  represent the equatorial and polar radii of the planet respectively<sup>2</sup>.

Since oblateness is as a result of planet rotation, its measurement can provide information about the rotation rate of an exoplanet and also its internal density structure. These can in turn shed valuable insight into the planet's formation and evolution (Lissauer, 1995; Li and Lai, 2020), as well as its atmospheric circulation and dynamics (Kaspi and Showman, 2015). The solar system planets have different rotation periods and oblateness indicating diverse formation and evolutionary histories (Laskar and Robutel, 1993). Saturn, having one of the fastest rotation with a period of only 10.7 hrs, has the highest oblateness of  $f = 0.098$  (i.e., its polar radius is 9.8% smaller than its equatorial radius). Although Saturn rotates slightly slower than Jupiter, it has a significantly lower density which allows its rotation induce a higher oblateness than in Jupiter (with  $f = 0.065$ ).

Measuring exoplanet oblateness is challenging as the induced effects in transit signals have low amplitudes. Previous studies investigated the photometric difference between the transit light-curve of an oblate planet and the corresponding spherical planet (e.g., Seager and Hui 2002; Barnes and Fortney 2003; Carter and Winn 2010a). They showed that the amplitude of the oblateness-induced signal for a giant planet, with Saturn-like oblateness and planet-to-star radius ratio of 0.1, is just around 100 ppm for the best case transit geometry. However, the amplitude increases by factor of a few for larger planets. Zhu et al. (2014) searched for oblateness signals in Kepler light-curve data and obtained a tentatively high oblateness of 0.22 for the brown dwarf Kepler-39b although they could not validate the consistency of the measurement across different subsets of the data. Later work by Biersteker and Schlichting (2017) did not detect the oblateness of Kepler-39b but put loose constraints on the oblateness of Kepler-427b. Therefore, measuring the oblateness of planets remains challenging. For very precise transit signals, assuming sphericity for an oblate planet would lead to systematic errors in the determination of the transit parameters (Barnes and Fortney, 2003).

---

<sup>2</sup>These are the same as  $r_2$  and  $r_3$  in the case of a triaxial ellipsoid seen in Chapter 4. However, here  $r_1 = r_2 > r_3$  since tidal deformation is negligible.

This work complements the previous studies by investigating, for the first time, the signature of planet oblateness in the spectroscopic RM signal.

## 5.2 Modelling oblate planet transits

Studying the transit effects of rings revealed that the projected shape of a planet with a continuous opaque ring extending directly from the planet surface (so that there is no gap between them) will mimic the projected shape of an oblate planet; if the ring is appropriately inclined with respect to the sky plane (Barnes and Fortney, 2004; Akısanmi et al., 2018). As such, the SOAP3.0 ringed planet tool, described in the Chapter 3, can be used to simulate the expected photometric light-curve and spectroscopic RM signal of an oblate planet<sup>3</sup>.

As depicted in Fig. 5.1, the projected shape of an oblate planet can be obtained using the ring planet model by first setting a core planet with a negligibly small radius (e.g. 10% of the required  $R_{eq}$ ; this is necessary since the inner and outer ring radii are in units of a core planet). A circular opaque ring starting at the surface of the core planet is then added with outer radius  $r_{out}$  extending out to the equatorial radius of the oblate planet to be modelled. Oblateness of the entire projected figure (core planet + ring) can be obtained by inclining the ring away from sky plane by  $i_r = \cos^{-1}(1 - f)$  which imitates a reduced radius at the poles compared to the equator. As  $i_r$  increases, the total projected figure becomes more oblate ( $f$  increases). The obliquity,  $\theta$ , of the ring also corresponds to the obliquity of the oblate planet defining the projected angle between its equatorial plane and the orbital plane. It ranges from  $-90^\circ$  to  $+90^\circ$  (equivalent to  $0 - 180$  used in Chapter 3) with positive angles measured anti-clockwise from the transit chord and negative angles measured clockwise.

We can defined the the mean radius of an oblate planet as

$$\bar{R}_p = \sqrt{R_{eq}R_{pol}} = R_{eq}\sqrt{1 - f}, \quad (5.2)$$

so that for  $f = 0$ ,  $R_{eq} = R_{pol}$  and the mean radius of the oblate planet is same as the radius of a spherical planet. The maximum possible value of  $f$  that can be attained by

---

<sup>3</sup>Although there might be some slight differences in using a ringed planet model to emulate the projected shape of oblate planets, it serves as a sufficient approximation and produces desired results consistent with previous studies.

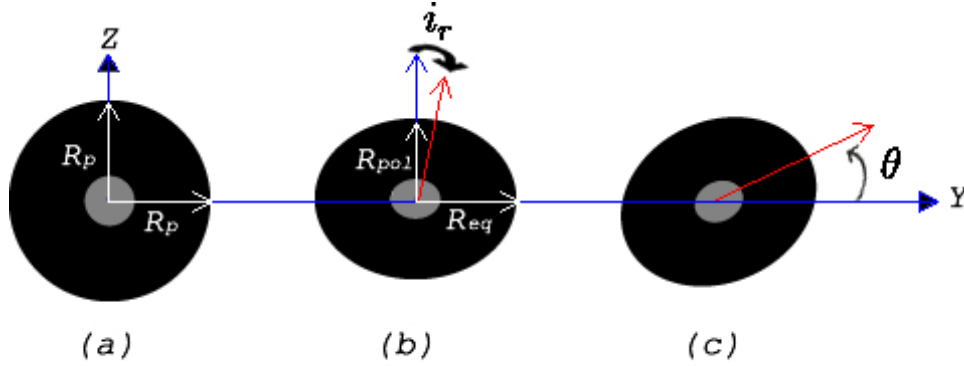


Figure 5.1: Illustration of the ring planet model used to describe an oblate planet. The small core planet is represented in gray and the ring in black, both of which are opaque. (a) shows the projection of a spherical planet with total radius  $R_p$  modelled with a circular face-on ring around a smaller ( $0.1 R_p$ ) core planet. (b) shows the ring now inclined away from sky plane  $YZ$  by an angle  $i_r = 36.87^\circ$ . This models an oblate planet with exaggerated  $f = 0.2$  making  $R_{pol} < R_{eq}$ . (c) shows the oblate planet now tilted from the orbital axis  $Y$  by an obliquity angle  $\theta = +30^\circ$ .

a planet is at the rotational break-up limit when the centrifugal acceleration balances the gravitational acceleration at the equator and this is at  $f \simeq 0.5$  (Carter and Winn, 2010a).

The oblateness ( $f$ ) is related to the the rotation period ( $P_{rot}$ ) of the planet by

$$P_{rot} = 2\pi \sqrt{\frac{R_{eq}^3}{GM_p(2f - 3J_2)}}, \quad (5.3)$$

where  $J_2$  represents the quadrupole moment of the planet (Carter and Winn, 2010a). This equation shows that  $f$  is inversely proportional to the rotation period and density ( $\rho_p \approx M_p/R_{eq}^3$ ) of the planet, so the effect of oblateness will be most significant for gaseous planets with short rotation periods. However, note that  $f$  and  $\theta$  measured from transit light-curves are not the true planet oblateness and obliquity but their projection on the sky plane since they are derived from the projected shape of the transiting planet (an ellipse). This means that the transit-derived values of  $f$  and  $\theta$  will always be lower limits on the true values. This, in turn, implies that only an upper limit on  $P_{rot}$  can be obtained (Seager and Hui, 2002; Carter and Winn, 2010a). Thus, measuring oblateness tells us that a planet is rotating faster than  $\Omega = 2\pi/P_{rot}$ .

### 5.3 Oblateness-induced signature

Previous studies compared the transit light-curve of an oblate planet to that of a spherical planet and showed that the oblateness signal manifests itself at the ingress and egress phases (e.g., Carter and Winn 2010a; Zhu et al. 2014). The oblateness-induced signal is a geometrical effect and is obtained as the residuals from fitting the transit observation of an oblate planet with a spherical planet model. The signal arises mostly due to difference in contact times at the stellar limb (ingress and egress) between the transiting oblate planet and the corresponding spherical planet. Also, an asymmetry is introduced between the ingress and egress phases for non-zero planet obliquity which cannot be accounted for by a spherical planet transit (Seager and Hui, 2002; Barnes and Fortney, 2003). Since the geometry of a transiting planet is the same when taking photometric and spectroscopic transit measurements, the signature of oblateness should also be present in transit RM signals.

To illustrate the oblateness signature in light-curves and RM signals and to validate *SOAP3.0* for oblateness studies, we follow the work of Carter and Winn (2010a) which analysed seven *Spitzer* transit observations of the giant planet HD 189733b in an attempt to put constraints on its oblateness. The planet was selected due to its large size, bright host star and availability of precise *Spitzer* data. The planet has the following parameters: planet-to-star mean radius ratio  $\bar{R}_p = 0.15463 R_*$  ( $1.13 R_{\text{Jup}}$ ),  $a/R_* = 8.81$ ,  $b = 0.68$  and  $P = 2.22$  days (Torres et al., 2008). The host star is of K2 spectral type with V-magnitude  $m_V = 7.7$ , radius  $R_* = 0.75 R_\odot$  and  $v \sin i_* = 3.5 \text{ km s}^{-1}$ . Before analysing the *Spitzer* data, they calculated the theoretical oblateness signal amplitude expected for HD 189733 b by simulating its photometric light-curve assuming two different scenarios: (1) Saturn-like oblateness of  $f = 0.098$  and projected obliquity  $\theta = 45^\circ$ , and (2) a more realistic lower oblateness of  $f = 0.003$  (expected for the tidally-locked planet from Eq. 5.3) and  $\theta = 0^\circ$ .

*SOAP3.0* was also used to simulate the oblate planet light-curve and RM signal of this planet. The light-curve was generated with *Spitzer* cadence of 2 minutes using quadratic LDCs of [0.076, 0.034] in the *Spitzer* infrared band as given in Carter and Winn (2010a). The RM signal was generated with an integration time of 4 mins<sup>4</sup> which, for real observations, will help reduce the amplitude of stellar noise in this star as recommended in

---

<sup>4</sup>This integration time is similar to the 5 mins exposures of *HARPS* archival RM observations of HD 189733b used by Triaud et al. 2009; Wyttenbach et al. 2015.

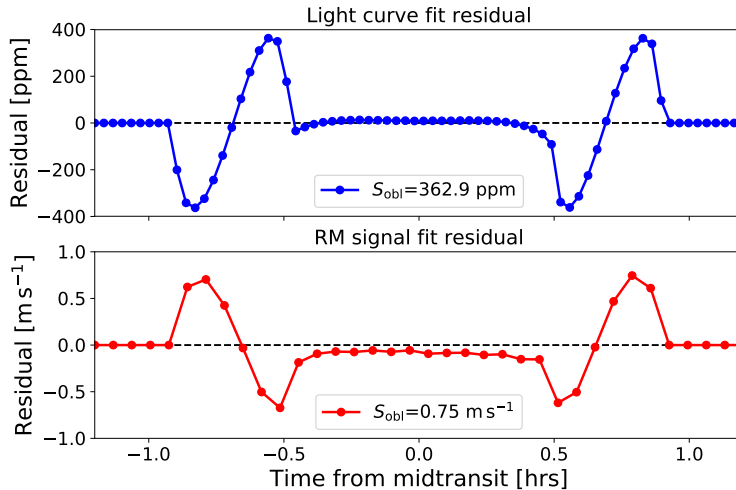


Figure 5.2: Oblateness-induced signatures obtained as the residuals from fitting the simulated oblate planet transit signals (top: light-curve, bottom: RM signal) of HD 189733b assuming projected quantities  $f = 0.098$  and  $\theta = 45^\circ$ .

Chaplin et al. (2019) for K-dwarfs. LDCs were obtained for the star in the visible band using Claret and Bloemen (2011) LD tables while a value of  $\lambda = 0^\circ$  was assumed (close to the value of  $0.85^\circ$  derived in Triaud et al. 2009). The oblate planet light-curve and also its RM signal are then fitted with spherical planet models.

Fig. 5.2 shows the residuals (oblate - spherical) from both the light-curve and RM signal fits of scenario 1 which assumed Saturn-like oblateness. The amplitudes ( $S_{\text{obl}}$ ) of the residuals from both signal fits are quoted. The residuals show that the signature of oblateness is concentrated at the transit ingress and egress<sup>5</sup>. The residuals from fitting the oblate transit signals of the tidally-locked scenario is not visible on the scale shown in Fig. 5.2 ( $1.8 \text{ ppm}$  and  $0.01 \text{ m s}^{-1}$ ) confirming that oblateness of tidally-locked planets cannot be detected (§5.3.1).

For the Saturn-like oblateness scenario, the residuals obtained from the light-curve fit is in agreement, in shape and amplitude, with the photometric result obtained in Carter and Winn (2010a) for this planet (see their Figure 1). The oblateness-induced signature in the RM signal, shown here for the first time, has an amplitude  $S_{\text{obl}} = 0.75 \text{ m s}^{-1}$  whereas the *ESPRESSO* spectrograph is capable of attaining instrumental RV precisions up to  $0.1 \text{ m s}^{-1}$ . Using the *ESPRESSO* Exposure Time Calculator (ETC)<sup>6</sup>, a theoretical *ESPRESSO* RV precision of  $0.31 \text{ m s}^{-1}$  was estimated for observation of this star with 4-minute exposure time using the high resolution (UT1; 140,000) mode<sup>7</sup>. Taking into

<sup>5</sup>Chapter 6 will discuss possible ways to distinguish the induced signals of the different features which all manifest in the ingress and egress.

<sup>6</sup>[www.eso.org/observing/etc](http://www.eso.org/observing/etc) - Version P105.6

<sup>7</sup>Note: In simulating the aforementioned RM signal, this *ESPRESSO* resolution was used to calculate

account the rotational velocity broadening which degrades the quality factor of the spectra with respect to its non-rotating counterpart, the RV precision for this star degrades by a factor of 1.8 to  $\sim 0.56 \text{ m s}^{-1}$  (calculated by interpolating between values in Table 2 of Bouchy et al. 2001). This RV precision can be improved if the data is phase folded over an increased number of transit observations ( $n$ ) as it scales in the photon noise limit with  $1/\sqrt{n}$ . Assuming seven observed transits (number of *Spitzer* transits analysed in Carter and Winn 2010a), a better RV precision of  $\sim 0.2 \text{ m s}^{-1}$  would be achieved which is much lower than the spectroscopic oblateness amplitude of this system. Moreover, RM measurements of longer period planets can be obtained with longer exposure times that provide a higher RV precision such that several transit observations are not necessarily needed.

Although the analysis assuming Saturn-like oblateness is simply illustrative (for a tidally locked planet), it hints that *ESPRESSO* RM measurements of “relevant” systems with transiting planets could allow reasonable constraints to be placed on planet oblateness in addition to those from light-curve analysis. This possibility will be further investigated in this work with suitable considerations discussed in §5.3.1 and §5.3.2.

### 5.3.1 Tidal interaction

Figure 5.2 showed the signature of oblateness in the photometric light-curve and spectroscopic RM signal for a short period planet. However, short period planets such as HD 189733 b have short tidal evolution timescales so they are expected to already have circularised orbits and synchronised rotations such that the rotation period  $P_{rot}$  becomes equal to the orbital period  $P$  (Guillot et al., 1996). Such short period planets cannot have significant rotation-induced oblateness since their rotations will be too slow (Seager and Hui, 2002). Indeed, Carter and Winn (2010a) did not detect oblateness in this planet after analysing the *Spitzer* data.

Strong tidal interaction also affects the obliquity of short period planets by driving the value of  $\theta$  to zero at the same short timescale for attaining rotation synchronisation (Peale, 1999). Avoiding stellar tidal interaction then imposes the requirement for long period orbits to ensure rapid planet rotation for significant oblateness. Seager and Hui (2002) and Carter and Winn (2010b) showed that a Jupiter-mass planet orbiting a Solar

---

the FWHM of the CCF which was additionally broadened to account for macro-turbulence (convection) using calibration equation from Doyle et al. (2014).

twin star at a distance of  $\sim 0.2$  AU ( $P \simeq 30$  days) will have tidal synchronisation timescale of  $\sim 10$  Gyrs (which is greater than the age of most host stars) so that the planet is not expected to have spun down and can therefore have significant rotation.

### 5.3.2 Spin precession

The spin axis of an oblate planet will precess due to the gravitational torque exerted on the planet by the host star. The effect of spin precession on transit signals is that the orientation of the oblate planet changes with time and so does its projection. This leads to variations in the light-curve and RM signal shapes between transit observations. Such variations can complicate efforts to measure the ingress and egress oblateness signature since combining successive transits might average out the subtle signal. However, a Jupiter or Saturn-like planet with  $P \simeq 30$  days is expected to have precession period of  $\sim 50$  yrs (Carter and Winn, 2010b) which is too long to be observed within a few transit observations of the planet. For example, the spin axis of a  $P = 30$  days planet will precess by a negligible  $1.8^\circ$  in 3 successive transit observations thereby allowing the phase folding of data to probe oblateness.

Although some studies (e.g., Carter and Winn, 2010b; Biersteker and Schlichting, 2017)) have illustrated the possibility of detecting oblateness due to spin precession for  $P < 30$  days, we investigate here the case of planets with  $P \geq 30$  days for which significant rotation induced oblateness is expected and spin precession is negligible.

## 5.4 Detecting oblateness

### 5.4.1 Identifying optimal transit geometry

The oblateness signature depends on the obliquity of the planet ( $\theta$ ) and the inclination of its orbit ( $i_p$  or  $b$ ). It is useful to identify combinations of these two parameters that are optimal for detecting oblateness. Although the value of  $\theta$  is unknown a-priori for planets, an understanding of how it affects the oblateness detectability is important as it can be used to estimate the maximum theoretical oblateness signal expected for a planet and thus aid in target selection. While previous works (e.g., Barnes and Fortney 2003; Zhu et al. 2014) have identified  $\theta - b$  parameter combinations with the highest photometric oblateness signal amplitude, the focus here is to understand how the spectroscopic signal amplitude varies in comparison to the precision of new spectrographs like *ESPRESSO*.



Table 5.1: Adopted system parameters of the hypothetical long period oblate planet.

Parameter	$\bar{R}_p [R_*$	$a/R_*$	$P$ [d]	$\lambda$ [°]	$f$	$m_V$	$q_1$	$q_2$	$v \sin i_*$ [km s <sup>-1</sup> ]
Value	0.1546	70.75	50	0.0	0.098	7.7	0.5151	0.3872	5.0

To investigate this, a hypothetical system is considered with parameters similar to the HD 189733 system except that the Jupiter-sized planet now orbits at a longer period of 50 days (based on considerations from §5.3.1 and §5.3.2) and the star rotates slightly faster with  $v \sin i_* = 5 \text{ km s}^{-1}$ . As before, a projected planet oblateness of  $f = 0.098$  is assumed and quadratic LDCs for this star in the visual band is obtained from Claret and Bloemen (2011) but re-parameterized as  $[q_1, q_2]$  following Kipping (2013a). The full adopted parameters for the simulated system is given in Table 5.1.

SOAP3.0 is used to generate theoretical transit signals (light-curves and RM signals) for the adopted oblate planet on a grid of obliquity ( $\theta$ ) and impact parameter ( $b$ ) values with a total of 42 combinations (excluding grazing transits since their ingress/egress are undefined). The transit durations and ingress (egress) durations of the transit signals vary with  $b$ . From  $b = 0$  to 0.8, the transit durations decrease from  $\sim 6.3$  to  $\sim 4.5$  hrs whereas the ingress (egress) durations increase from  $\sim 55$  to  $\sim 90$  mins. Therefore, transits at higher impact parameters will allow better temporal sampling of oblateness induced features due to their longer ingress and egress durations. The light-curves were simulated with 2-min integration time (or binning) similar to *TESS* observations but applicable to other photometric instruments to increase the attained precision of each measurement. On the other hand, the RM signals were simulated with a slightly longer integration time of 8 mins<sup>8</sup> which enables *ESPRESSO* reach a higher RV precision of  $0.22 \text{ m s}^{-1}$  while still providing good temporal resolution of the ingress and egress of this planet. Other spectrographs (like *HARPS* installed on a smaller 3.6 m telescope) are not capable of reaching such precision within this short integration time. To attain the same precision as *ESPRESSO*, *HARPS* will require  $\sim 30$  mins integrations which will not allow enough data points to probe oblateness signatures at ingress and egress.

A spherical planet model is then used to fit the oblate planet light-curve and RM

<sup>8</sup>Spectroscopic transit observations usually require longer integrations than the photometric because spectrographs lose photons due to slit losses, stray light, and scattered light and so require longer time to collect more photons (Oshagh, 2018a). Long integrations are also used to average out and reduce stellar RV noise. We note also that longer period planets can have longer integrations/binning which should be chosen such that the ingress and egress are still well sampled.

signal of each parameter combination to obtain the amplitude,  $S_{\text{obl}}$ , of the residuals (at ingress/egress). The free parameters in the light-curve fit were  $R_p$ ,  $a/R_*$ ,  $b$ ,  $q_1$ , and,  $q_2$  while the RM signal fit additionally had  $v \sin i_*$  and  $\lambda$ .

Figure 5.3 shows the contour plots generated using the residual amplitudes from fitting the different transit signals. It represents the amplitude of observable oblateness-induced signal,  $S_{\text{obl}}$ , at each parameter combination. The contours are shown only for positive  $\theta$  angles as the pattern is symmetric about  $\theta = 0$ . In both contour plots, a similar trend is seen showing that the amplitude of photometric and spectroscopic oblateness signal is lowest (yellow regions) at zero obliquity across all impact parameters. This implies that the best-fit spherical model can easily emulate the light-curve and RM signal of the oblate planet by adjusting its fit parameters thereby making it difficult to detect oblateness at these orientations. However, at higher obliquities, the amplitude increases with impact parameter due to asymmetry between ingress and egress of the oblate planet transit signal that cannot be easily emulated by a spherical model. The oblateness signal reaches its peak amplitude at points around  $\theta = 45^\circ$ ,  $b = 0.7$  (dark blue regions) in agreement with the results of earlier photometric studies (e.g., Seager and Hui 2002; Carter and Winn 2010a) but confirmed here to be same in spectroscopy. The contour plot is nearly symmetric about the vertical  $45^\circ$  line with the exception of a few orientations around  $b$ ,  $\theta = 0, 90^\circ$ .

The impact of the spin-orbit angle ( $\lambda$ ) on the spectroscopic oblateness signal amplitude can also be assessed. For the yellow regions in Fig. 5.3 with low oblateness signal amplitudes (i.e. orientations with  $\theta \approx 0^\circ$  and those with  $b \approx 0$ ), the obtained spectroscopic oblateness signal amplitudes can increase for planets with spin-orbit misalignment (i.e.  $\lambda \neq 0$ ). For example, the spectroscopic oblateness amplitude at the orientation  $\theta = 0^\circ, b = 0.2$  is only  $0.05 \text{ m s}^{-1}$  (Fig. 5.3) when  $\lambda = 0^\circ$  but significantly increases to  $0.61 \text{ m s}^{-1}$  for  $\lambda = 30^\circ$ . In contrast, this orientation has a photometric oblateness amplitude of only 3 ppm irrespective of  $\lambda$ . The orientations in the yellow regions can thus be more favorable for detecting oblateness in spectroscopy than in photometry. Fig. 5.4 shows the variation of the spectroscopic oblateness amplitude with  $\lambda$  at orientations with  $\theta = 0^\circ$  and also orientations with  $b = 0$ .

In summary, Fig. 5.3 shows that the oblateness-induced signal is more prominent, in photometry and spectroscopy, for oblique planets at high impact parameters particularly for the points around  $\theta = 45^\circ$ ,  $b = 0.7$  (optimal transit orientation) which provides the

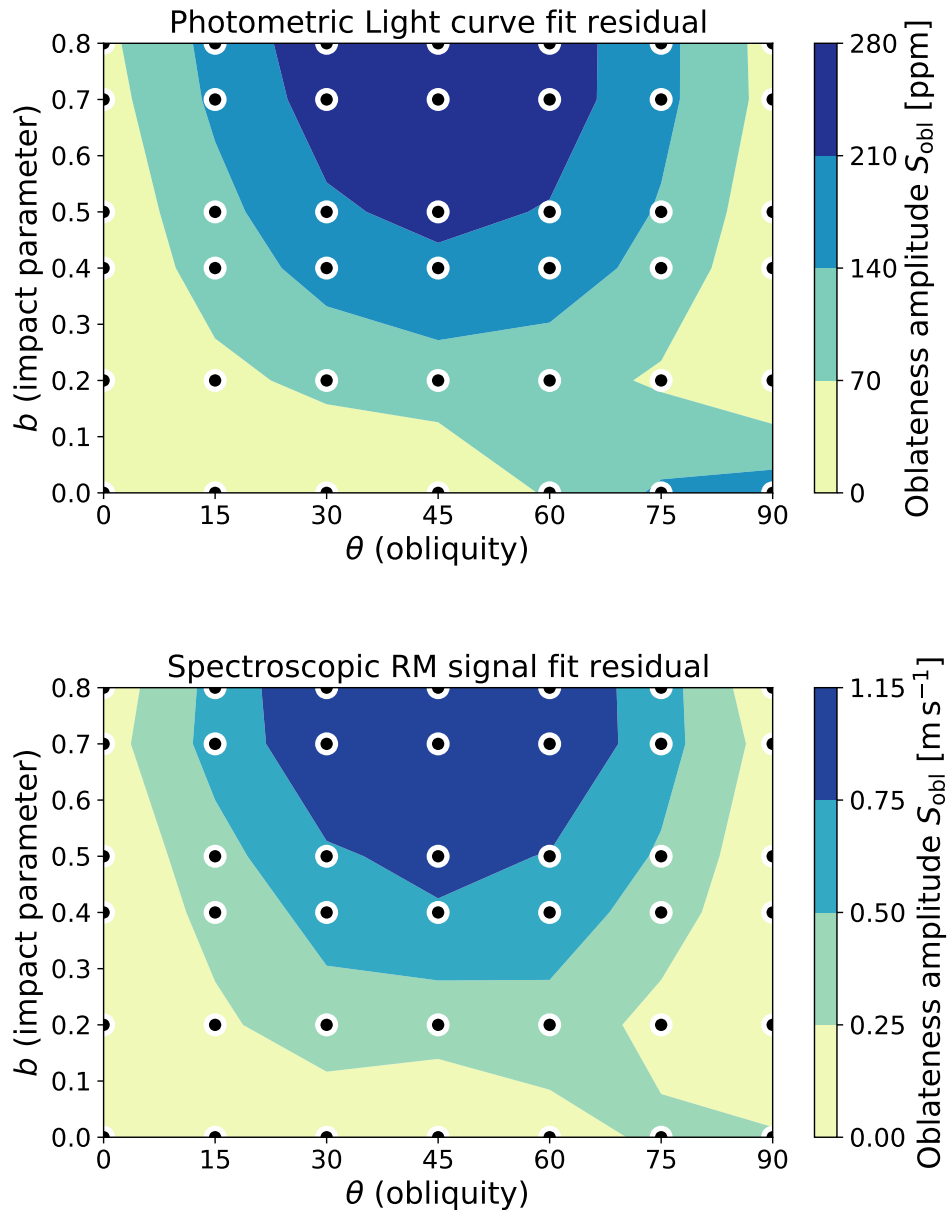


Figure 5.3: Contour plots showing amplitude,  $S_{\text{obl}}$ , of observable oblateness-induced signal. The plots are generated from fitting 42 oblate planet transit signals of different  $\theta - b$  combinations with a spherical planet model. Top: Contour from light-curve fit residuals. Bottom: Contour from RM signal fit residuals with  $\lambda = 0$ . Black circles indicate the parameter combinations of the signals from which the residual amplitudes were obtained.

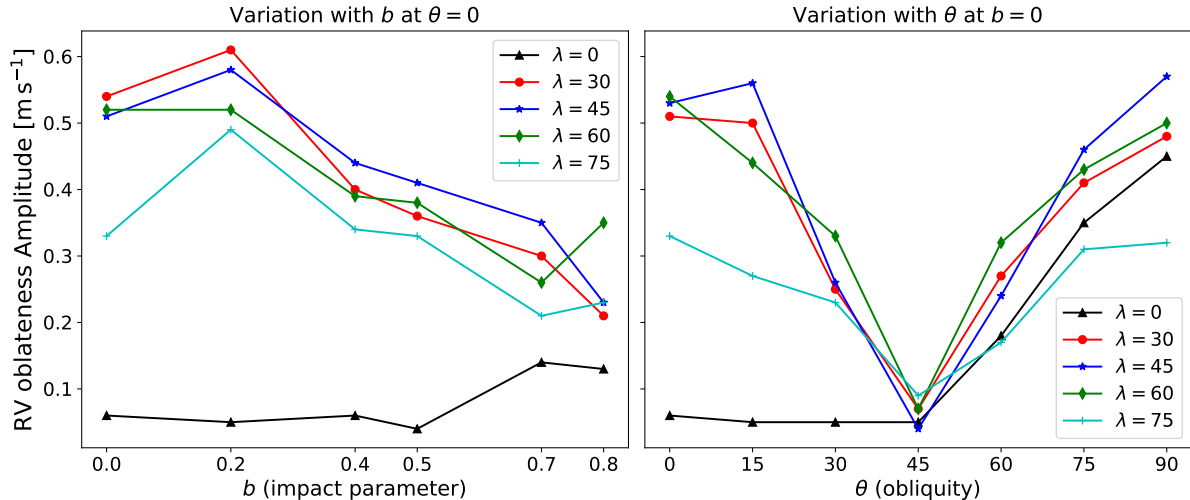


Figure 5.4: Variation of RV oblateness amplitude at different values of spin-orbit angle ( $\lambda$ ). Left: Amplitude variation with  $b$  at  $\theta = 0$ . Right: Amplitude variation with  $\theta$  at  $b = 0$ .

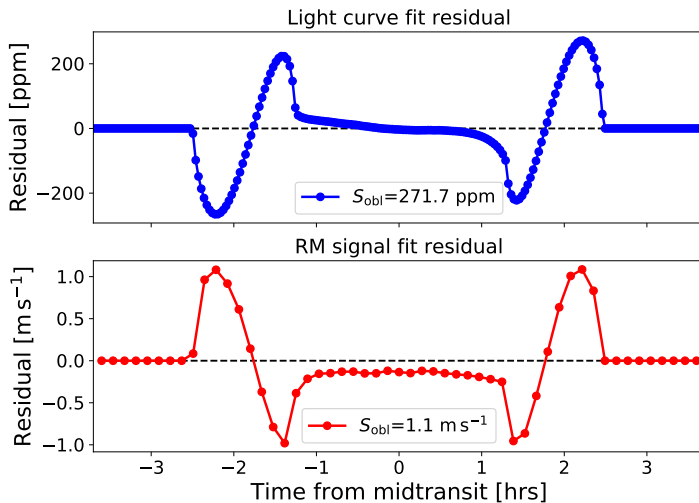


Figure 5.5: Oblateness-induced signal obtained from fitting simulated oblate planet of  $\theta=45^\circ$ ,  $b=0.7$  with spherical planet model. Top: light-curve fit residual. Bottom: RM signal fit residual.

best opportunity to measure oblateness. The residual from the fit of this orientation is shown in Fig. 5.5 with photometric and spectroscopic oblateness amplitudes of  $\sim 272$  ppm and  $1.1 \text{ m s}^{-1}$ , respectively.

The amplitude of the photometric and spectroscopic oblateness-induced signal for a particular parameter combination ( $\theta, b$ ) scales with the oblateness and planet radius as  $\sim (f/0.098) (\bar{R}_p/0.1546)^2$  (Barnes and Fortney, 2003). Therefore, planets with larger planet-to-star radius ratios will have larger oblateness signatures for the same projected oblateness. For the same planet, the spectroscopic oblateness amplitude ( $S_{\text{obl}}^{\text{sp}}$ ) was found to additionally scale with the projected stellar rotational velocity following the

relation

$$S_{\text{obl}}^{\text{sp.}} \propto \left( \frac{v \sin i_*}{5 \text{ km s}^{-1}} \right) \left( \frac{f}{0.098} \right) \left( \frac{\bar{R}_p/R_*}{0.1546} \right)^2. \quad (5.4)$$

## 5.4.2 Oblateness detectability

Detecting planet oblateness implies obtaining a measurement for the parameter  $f$  by fitting a transit observation, of sufficient precision, with an oblate planet model. Recovering  $f \simeq 0$  implies that a spherical planet model is a better fit to the observation than an oblate planet model. Detecting oblateness thus requires that  $f$  is recovered with accuracy and statistical significance above zero from the fitting process.

To illustrate the photometric and spectroscopic detectability of oblateness, the transit signals (light-curve and RM) of the hypothetical oblate planet (Table 5.1) was simulated at the determined optimal orientation ( $\theta = 45^\circ$ ,  $b = 0.7$ ) which have oblateness amplitudes of 272 ppm and  $1.1 \text{ m s}^{-1}$  (Fig. 5.5). As before, the light-curve and RM signal were simulated with cadences of 2 mins and 8 mins, respectively. Random Gaussian (white) noise of different levels,  $N$ , was added to the simulated transit signals. We then investigated how well we can recover  $f$  and at what noise level it would be difficult to distinguish between the oblate planet and spherical planet transit signals (light-curve and RM). This is useful in order to understand the instrumental precisions required for photometric and spectroscopic detection of oblateness.

A fit to the simulated oblate planet transit signals with noise is then performed, using `emcee` and `SOAP3.0` oblate model, in order to recover the planet’s oblateness and transit parameters along with their uncertainties. The priors on the parameters are given in Table. 5.2. The MCMC was performed with 36 walkers each having 20,000 steps (which was several times the computed auto-correlation time as recommended in `emcee` as a convergence diagnostic). The initial 25% of the steps were then discarded as burn-in.

Figure 5.6 shows the oblateness detectability plot, in photometry and spectroscopy, indicating the median and standard deviations of the recovered  $f$  at different noise levels (average of three MCMC realisations). For oblateness to be confidently detected ( $f$  measured), we require that  $f$  is recovered with  $3\sigma$  significance above zero.<sup>9</sup> It can be seen in the spectroscopic detectability plot (right panel of Fig. 5.6) that  $f$  is detected with  $3\sigma$

---

<sup>9</sup>As a check of the MCMC analysis, it was confirmed that fitting a spherical planet transit signal with an oblate planet model recovers  $f \simeq 0$  at different noise levels.

Table 5.2: Priors on the fitted parameters in the MCMC.  $f$  ranges from zero for a spherical planet model to the maximum possible value of 0.5.  $+$  denotes additional prior parameters used in fitting the RM signals.

Parameter	Prior	Interval
$\bar{R}_p$	Uniform	$\mathcal{U}(0.10, 0.20)$
$b$	Uniform	$\mathcal{U}(0, 1)$
$a/R_*$	Uniform	$\mathcal{U}(80, 120)$
$q_1$	Normal	$\mathcal{N}(0.5151, 0.052)$
$q_2$	Normal	$\mathcal{N}(0.3872, 0.039)$
$\theta$	Uniform	$\mathcal{U}(-90, 90)$
$f$	Uniform	$\mathcal{U}(0.0, 0.5)$
$\lambda$ $+$	Uniform	$\mathcal{U}(-45, 45)$
$v \sin i_*$ $+$	Normal	$\mathcal{N}(5.0, 0.25)$

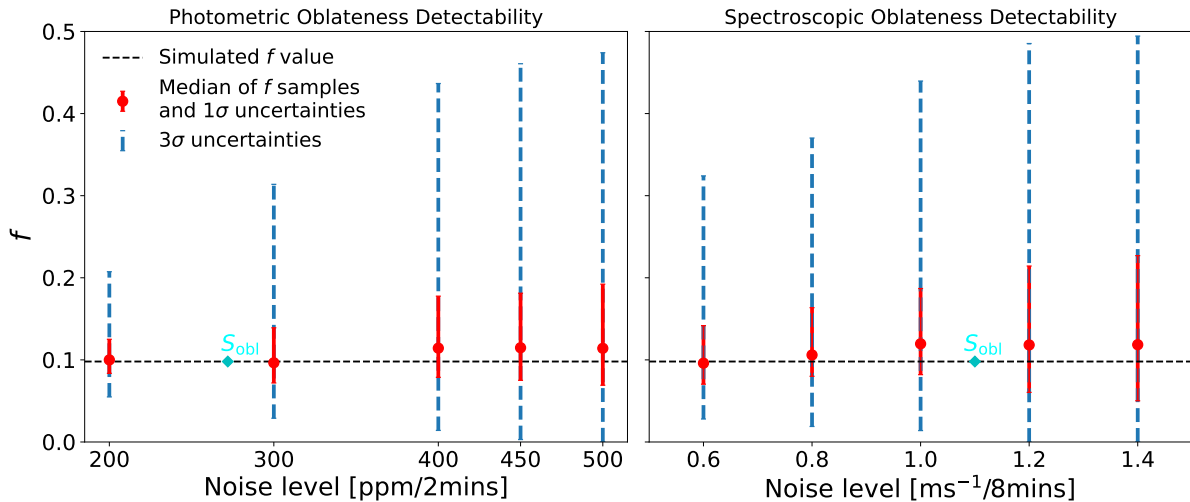


Figure 5.6: Detectability of oblateness in photometry (left) and RV (right) as a function of instrumental noise. The black dashed line is the simulated  $f$  value. The points are the median of the recovered  $f$  samples at each noise level with red errorbars showing the  $1\sigma$  CI and blue errorbars showing  $3\sigma$  CI. The cyan diamonds, labelled  $S_{\text{obl}}$ , indicate the photometric and RV oblateness signal amplitude as obtained in Fig 5.5.

significance for noise levels up to  $1 \text{ m s}^{-1}/8 \text{ mins}$ . At higher noise levels, the distribution of the recovered  $f$  samples include  $f = 0$  at  $3\sigma$  implying that a spherical planet model is also probable. In the photometric detectability plot (left panel of Fig 5.6), a  $3\sigma$  detection is attained for noise levels up to  $400 \text{ ppm}/2 \text{ mins}$ . We note that  $2\sigma$  detection of oblateness can still be attained at higher noise levels (up to  $550 \text{ ppm}$  in photometry and  $1.5 \text{ m s}^{-1}$  in spectroscopy).

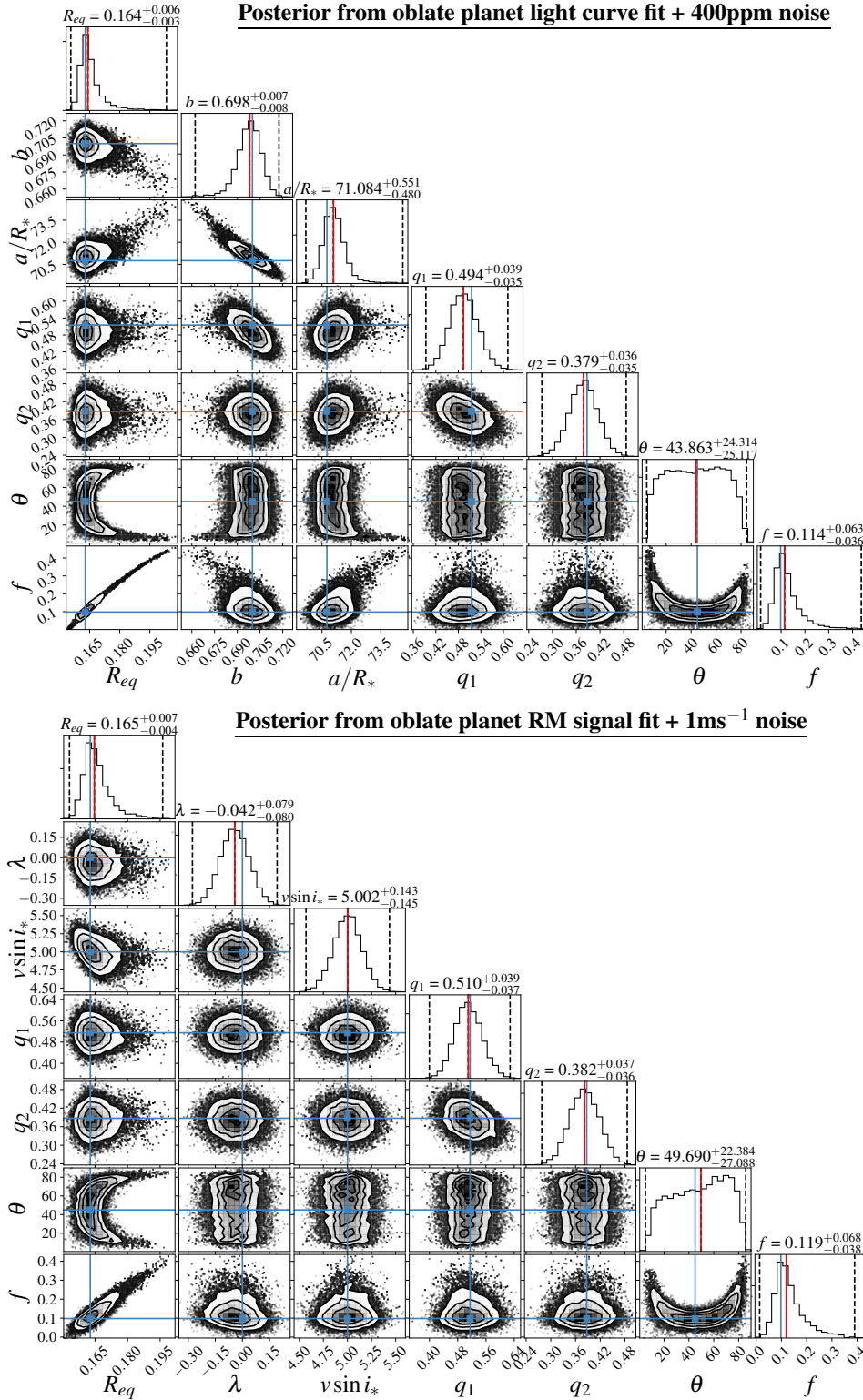


Figure 5.7: Top: Posterior distributions of all parameters from fitting the simulated oblate planet light-curve with 400 ppm noise added. Bottom: Posteriors of some parameters ( $b$  and  $a/R_*$  are not shown for brevity) from fitting of the simulated oblate planet RM signal with  $1 \text{ms}^{-1}$  noise added. The quoted values are the median (also red lines) and  $1\sigma$  CI. The dashed vertical lines indicate the  $3\sigma$  limits while blue lines indicate the true simulated values.

Figure 5.7 shows the posterior distributions of the retrieved parameters at the detectable noise limits (400 ppm noise added to light-curve and  $1 \text{ m s}^{-1}$  added to RM signal). In both cases, we see from the  $f - \theta$  joint distributions that  $\theta$  is not well-constrained and is strongly correlated with  $f$  ( $\theta$  is only better constrained for highly precise transit signals). Figure 5.3 already showed that the amplitude of the oblateness signal is fairly symmetric about  $\theta = 45^\circ$  and reduces as the value of  $\theta$  gets farther from  $45^\circ$ . Therefore, for  $\theta$  values different from  $45^\circ$  in the  $f - \theta$  distribution, the amplitude of oblateness signal reduces and a higher value of  $f$  is needed to fit the observation. The degeneracy between  $f$  and  $\theta$  is responsible for the long tail towards large oblateness in the  $f$  distribution (also seen for all noise levels in Fig. 5.6).

The posterior of the fitted mean radius  $\bar{R}_p$  was converted to  $R_{eq}$  using Eq. 5.2 to show the evidently strong correlation between  $f$  and  $R_{eq}$ ; as the oblateness increases, the equatorial radius gets more elongated compared to the polar radius. It is interesting to see that the LDCs ( $q_1, q_2$ ) are not strongly correlated with  $f$  implying that very precise determination of their values are not required to detect planetary oblateness which is contrary to the case for detecting rings and tidal deformation (Akınsanmi et al., 2018, 2019; Hellard et al., 2019). Indeed when we adopt a non-informative uniform prior of  $\mathcal{U}(0, 1)$  on the LDCs,  $f$  is still similarly recovered but with larger uncertainties. The posteriors from the RM signal MCMC (lower panel in Fig. 5.7) also shows that  $\lambda$  and  $v \sin i_*$  are not correlated with  $f$  implying that planetary oblateness does not affect the accurate retrieval of these parameters from RM signals.

The retrieval of  $f$  from combined analysis of the photometric light-curve and spectroscopic RM signal was also investigated. As seen in Fig. 5.6,  $f$  is not recovered with  $3\sigma$  for noise levels of 450 ppm (added to the light-curve) and  $1.2 \text{ m s}^{-1}$  (added to the RM signal). However, simultaneously fitting both transit signals allows the recovery of  $f$  with  $3\sigma$  significance and with better accuracy as shown in Fig. 5.8 (compared to the Figs. 5.6 and 5.7).



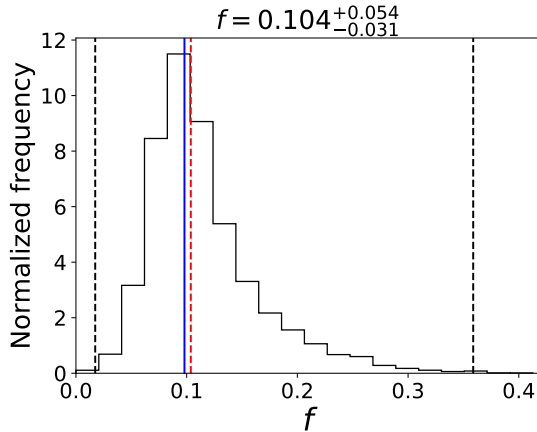


Figure 5.8: Histogram of recovered  $f$  samples from simultaneous MCMC fit of light-curve (with 450 ppm noise) and RM signal (with  $1.2 \text{ m s}^{-1}$  noise). Lines and values are as described in Fig. 5.7.

## 5.5 Discussion and Summary

As shown in Fig. 5.6, white noise levels of 400 ppm in photometry and  $1 \text{ m s}^{-1}$  in spectroscopy are the detectability noise limits required to measure Saturn-like oblateness in our hypothetical HD189733b-like planet (Table 5.1). These detectability limits can be compared with the noise level attainable by different observing instruments for stars of different magnitudes as given in Table 5.3. The theoretical *ESPRESSO* noise levels for  $8 m_V$  and  $10 m_V$  stars, after considering the effect of stellar rotation, are  $0.58 \text{ m s}^{-1}$  and  $1.5 \text{ m s}^{-1}$  per 8 min integrations respectively. The spectroscopic detectability noise limit of  $1 \text{ m s}^{-1}$  is only attainable for  $m_V = 8$  stars which implies that *ESPRESSO* is only capable of detecting the oblateness of planets around bright stars ( $m_V \leq 9$ ), if only one transit is observed. For stars of  $m_V = 10$ , *ESPRESSO* can still constrain the oblateness but with a lesser significance ( $< 2\sigma$ ). In contrast, the photometric detectability noise level of 400 ppm/2min is well attainable by *CHEOPS*, *PLATO* and *JWST* for  $3\sigma$  oblateness detection for planets transiting stars as faint as  $m_V = 12$ . *TESS* is only capable of measuring  $f$  for the brightest stars ( $m_V \leq 8$ ) and with  $\leq 2\sigma$  significance.

In general, we define  $S_{\text{obl}}/N$  as the ratio of the expected oblateness signal amplitude to the observational noise level which can be used to set a baseline for detecting oblateness. A  $3\sigma$  detection of Saturn-like oblateness for our hypothetical planet thus requires  $S_{\text{obl}}/N \geq 0.68$  (i.e. 272 ppm/400 ppm) for photometry and  $S_{\text{obl}}/N \geq 1.1$  (i.e.  $1.1 \text{ m s}^{-1}/1 \text{ m s}^{-1}$ ) for spectroscopy. However, a  $2\sigma$  detection only requires  $S_{\text{obl}}/N$  of 0.5 and 0.73 for photometry and spectroscopy, respectively. Several transits can, of course, be combined to lower noise levels and increase the significance of oblateness detections.

The implication of the  $S_{\text{obl}}/N$  calculation is that the photometric data is more sensi-

Table 5.3: Photon noise level per integration/binning time for stars of  $m_V=8$  and 10 observed with different instruments

Instrument	Noise/time	Noise/time
	@ $m_V = 8$	@ $m_V = 10$
TESS <sup>a</sup>	512 ppm/2 mins	1109 ppm/2 mins
CHEOPS <sup>b</sup>	127 ppm/2 mins	219 ppm/2 mins
PLATO <sup>c</sup>	44 ppm/2 mins	148 ppm/2 mins
JWST (NIRCam) <sup>d</sup>	$\sim 40$ ppm/2 min	72 ppm/2 mins
ESPRESSO <sup>e</sup>	$0.25 \text{ m s}^{-1}/8 \text{ mins}$	$0.65 \text{ m s}^{-1}/8 \text{ mins}$
(@ $v \sin i_* = 5 \text{ km s}^{-1}$ ) <sup>*</sup>	( $0.58 \text{ m s}^{-1}/8 \text{ mins}$ )	( $1.5 \text{ m s}^{-1}/8 \text{ mins}$ )

<sup>a</sup> [heasarc.gsfc.nasa.gov/cgi-bin/tess/webtess/wtv.py](https://heasarc.gsfc.nasa.gov/cgi-bin/tess/webtess/wtv.py)

<sup>b</sup> [cheops.unige.ch/pht2/exposure-time-calculator](https://cheops.unige.ch/pht2/exposure-time-calculator)

<sup>c</sup> Rauer et al. (2014)

<sup>d</sup> Noise floor from Beichman et al. (2014). Also noise estimate from (Hellard et al., 2019).

<sup>e</sup> [www.eso.org/observing/etc](https://www.eso.org/observing/etc). \* The RV noise level increases by a factor of 2.3 for  $v \sin i_* = 5 \text{ km s}^{-1}$  (Bouchy et al., 2001).

tive for detecting oblateness as it is able to recover  $f$  at lower  $S_{\text{obl}}/N$  than in spectroscopy. This is because we are, in general, able to sample light-curves with higher cadence than RM signals thereby providing more information on the ingress/egress anomaly induced by oblateness. Nonetheless, a simultaneous fit of the light-curve and RM allows consistent parameter values to be derived for the system and provides the best recovery of  $f$  both in precision and accuracy. Furthermore, spectroscopic detection of oblateness would provide independent and complementary verification of the oblateness signal which will increase the credibility of any detection.

An additional finding is that the amplitude of photometric and spectroscopic oblateness signal can increase by more than 30% for observations at near-infrared (NIR) wavelengths where limb darkening is less significant. In this case, the stellar limb will be almost as bright as the centre thereby amplifying the difference between the oblate and spherical planet at ingress/egress. Performing the MCMC analyses with LDCs in the NIR band allows recovery of  $f$  with almost twice the precision at visual wavelengths and also more precise determination of  $\theta$ . The NIR instruments (NIRCam or NIRSpec) on the forthcoming *JWST* will be able to leverage on this to detect oblateness with greater ease. Spectrographs operating in NIR such as *NIRPS* (Bouchy et al., 2017), *CARMENES* (Quirrenbach et al., 2016), and *SPIRou* (Donati et al., 2018) can also be beneficial especially for transits across M-dwarfs where the planet-to-star radius ratio can

be target to favour oblateness detection. Furthermore, the effect of stellar activity is minimal in NIR thereby giving a detection advantage to observations with these instruments.

Given that the fast planetary rotation capable of inducing significant oblateness is expected principally from long period planets, ground-based instruments such as *ESPRESSO* will have challenges in continuously observing transits that lasts longer than a single night. At the minimum, the observations would need to cover ingress and egress phases to probe oblateness signature if the phases align with different observation nights. Globally coordinated observations alongside other high-precision spectrographs in strategic sites can help acquire better transit coverage but will require accounting for the offset between the different spectrographs.

### 5.5.1 Summary

Long period giant planets are capable of rapid rotations that can cause significant planetary oblateness. While previous studies have focused on probing oblateness by analysing transit light-curves, the work presented here showed that the oblateness-induced signal can also be observed in high-precision RM signals. Using the test case of a hypothetical HD 189733b-like planet with orbital period of 50 days, we saw that such a planet with Saturn-like oblateness can cause spectroscopic oblateness signatures with large enough amplitudes to be detected by high-precision spectrographs (like *ESPRESSO*). This is especially the case for planets around rapidly-rotating stars where the spectroscopic oblateness signal is amplified. We found that the photometric and spectroscopic oblateness signals are more prominent for high impact parameter transits of oblique planets and for planets with larger planet-to-star radius ratios. Additionally, we found that planet spin-orbit misalignment can cause high amplitude spectroscopic oblateness signals at some transit orientations where the photometric signals are undetectably low. This makes detecting oblateness in RM signals more favorable over light-curves at these orientations.

We showed that the photometric oblateness signal can be detected at lower signal-to-noise ratios than the spectroscopic signal principally due to better temporal resolution of light-curves that allows the ingress and egress oblateness signatures to be well sampled. However, combined analyses of the light-curve and RM signal of a planet can increase the precision and accuracy of oblateness measurement. Therefore, *ESPRESSO* alongside photometric instruments such as *CHEOPS*, *PLATO* and *JWST* will be capable of detect-

ing oblateness in suitable targets. However, stellar noise associated with stellar p-mode oscillation, granulation and activity will be a strong limiting factor to real photometric and spectroscopic determination of oblateness for a given star.

*The next section presents ongoing work on probing the oblateness of confirmed planets. Therefore the results are only preliminary and the analysis are still incomplete.*

## 5.6 Probing for oblateness in light-curves of confirmed planets

### 5.6.1 Target selection

As seen from Eq. 5.3 and discussion in §5.3, the best candidates for measuring oblateness from transit data are giant planets with orbital periods greater than 30 days. These planet have low densities and their relatively large distance from their star’s tidal influence can allow for rapid planetary rotations that cause significant oblateness.

A search for confirmed planets that match this criteria (on NASA Exoplanet Archive and Exoplanet.eu catalogs) revealed 32 candidate planets, most of which are *Kepler* planets. To further select the targets with precise enough data for oblateness detection, we recall from §5.5, that a  $2\sigma$  detection of oblateness requires that the oblateness amplitude  $S_{\text{obl}}$  is at least 0.5 times the noise level  $N$  of the data (i.e.  $S_{\text{obl}}/N \geq 0.5$ ). Therefore, theoretical analysis of these planets was performed by simulating their light-curves conservatively assuming they are twice as oblate as Saturn<sup>10</sup> and then fitting with a spherical planet model to obtain their expected  $S_{\text{obl}}$ . Planets whose phase-folded and adequately binned<sup>11</sup> data permit  $S_{\text{obl}}/N \geq 0.5$  are then selected. Some planets were further excluded due to visible starspot occultations (particularly around ingress/egress where oblateness signal is located) and transit duration variations which will confound efforts to constrain their oblateness. Table 5.4 shows the final list of selected targets and their parameters.

---

<sup>10</sup>this allows the inclusion of planets whose data are not precise enough to detect Saturn-like oblateness but might be sufficient if the planet is more oblate.

<sup>11</sup>such that there are still sufficient data points in ingress and egress to probe oblateness. Further analysis will still use the unbinned data.

Table 5.4: Parameters of selected targets for probing oblateness.  $S_{\text{obl}}$  represents the expected amplitude of oblateness signature if the planets have an exaggerated oblateness of  $f = 0.2$  while  $N$  is the determined out-of-transit noise scatter of the phase-folded and binned light-curves. TOI-216c was added since it is close enough to the  $S_{\text{obl}}/N = 0.5$  cut-off.

Planet	P [d]	$m_V$	$i_p$	$b$	$e$	$\omega$	$a/R_*$	$R_p[R_*]$	$S_{\text{obl}}$ [ppm]	$N$ [ppm]	$S_{\text{obl}}/N$
<sup>(1)</sup> Kepler-167e	1071.23	14.2	89.98	0.233	0.062	201	560.00	0.128	200.81	190	1.05
<sup>(2)</sup> Kepler-302c	127.282	15.7	89.46	0.83	0.000	90	88.66	0.094	195.32	262	0.75
<sup>(3)</sup> Kepler-46b	33.648	15.3	89.04	0.757	0.032	264.2	45.10	0.088	193.35	171	1.13
<sup>(4)</sup> TOI-216c	34.556	12.3	89.83	0.15	0.029	275	53.18	0.124	122.00	288	0.42


References: (1) Kipping et al. (2016); (2) Rowe et al. (2014); (3) Saad-Olivera et al. (2017); (4) Kipping et al. (2019).

### 5.6.2 Light-curve analysis

The light-curves data for each planet was obtained from MAST. The light-curves were pre-processed following the sample description in Chapter 2. Each light-curve was decontaminated and then detrended using either a GP or polynomial fit to the out-of-transit data points. As some of the planets showed strong signs of TTVs, a custom-modified<sup>12</sup> version of `batman` was used to fit and correct the mid-transit time of each transit in the light-curves before stacking them in phase. As the light-curve for most of the targets consists of both SC and LC data, only similar cadence transits were stacked together and then the transit model of the LC data was super-sampled during fitting in order to account for the temporal binning of the observation (Kipping, 2010a). This sampling difference means the scatter in the light-curves are different, so different jitter terms ( $\log \sigma$ ) were used for fitting the SC and LC points.

### 5.6.3 Model Comparison and detection validation

The processed light-curve of each planet is fit with both a spherical planet model and an oblate planet model with `SOAP3.0` and the models are compared. The fits are performed using the `dynesty` to obtain the posterior distribution of the parameters and the log-evidence ( $\log \mathcal{Z}$ ) for each model. The parameters of the models are the same as given in Table 5.2 for transit light-curves. A uniform prior is used on all parameters of the models except the LDCs ( $q_1, q_2$ ) which had normal priors centred on re-parameterised

<sup>12</sup>available on my github 

values from Claret and Bloemen (2011) table and a width of 0.1. Similar priors are used for the common parameters of both models.

A sensitivity check that can be done to ensure that detection of oblateness in a light-curve is not spurious (due to noise in the data) is to inject a spherical planet model into the out-of-transit regions of the light-curve and attempt to fit it with an oblate planet model. The result should give a value of  $f$  that is consistent with 0, implying no oblateness. A higher value of  $f$  would imply that the noise is dominating any detection. A further check, is to split the data into groups and fit separately to verify that any oblateness detection is consistent with several transits and not induced by other systematics or the incorrect stacking of the transits. The result of the analysis on each planet is given below.

### Kepler-46 b:

The *Kepler* data for Kepler-46 b consists of 21 SC transits and 14 LC transits with strong TTVs (Saad-Olivera et al., 2017). The result of the model comparison is summarised in Table 5.5 and the 1D posterior distributions in Fig. 5.9. An oblateness of  $f = 0.173^{+0.167}_{-0.098}$  is obtained corresponding to a  $1.8\sigma$  detection. However, comparing the evidence of the models leads to a Bayes factor of only 1.15 which implies anecdotal evidence in favour of the oblate model (Table 2.1). Therefore, given the *Kepler* data, the oblate model is not significantly more probable than the spherical one. This can be attributed to the fact that the star is faint ( $m_V=15$ ) and so the transit light-curve (Fig. 5.10) is not very precise to prominently identify the transit shape changes due to oblateness. Indeed the posterior of the transit shape parameters do not differ significantly (fig. 5.9). Despite this, it is interesting that the oblate model provides comparable evidence to the spherical model despite the inclusion of 2 extra parameters.

Inputting the  $f=0.173$  in Eq. 5.3 and assuming  $J_2$  of 0.015 similar to Saturn or Jupiter, a rotation period of  $P_{rot} = 4.29 \pm 1.56$  hrs is obtained for the planet which is less than half the rotation period of Saturn (10.7 hrs).

Splitting the observed transits in two groups and independently fitting the oblate model to them gives consistent oblateness value between them. The result is also consistent with the earlier fit to the whole data albeit the detection significance is worsened due to the fewer transits in each group. Injecting a spherical planet model in the data and fitting with an oblate model leads to a measurement of  $f$  that is consistent with 0 within  $1\sigma$  (Fig. 5.9, Table 5.5). These checks indicate that the results from the actual full

Table 5.5: Adopted priors and result of model comparison for Kepler-46b showing the relevant parameters.

Parameter	Priors	Spherical model fit	Oblate model fit	Oblate model fit to Injected spherical model
$\bar{R}_p [R_*$ ]	$\mathcal{U}(0.06, 0.095)$	$0.0818 \pm 0.001$	$0.0820 \pm 0.001$	$0.0817 \pm 0.001$
$a/R_*$	$\mathcal{U}(40, 60)$	$53.4^{+1.7}_{-1.6}$	$53.3^{+2.0}_{-1.4}$	$54.1^{+1.8}_{-1.6}$
$b$	$\mathcal{U}(0.5, 0.85)$	$0.615^{+0.028}_{-0.033}$	$0.615^{+0.026}_{-0.039}$	$0.612^{+0.023}_{-0.043}$
$q_1$	$\mathcal{N}(0.5123, 0.1)$	$0.503^{+0.070}_{-0.057}$	$0.487^{+0.085}_{-0.045}$	$0.482^{+0.068}_{-0.059}$
$q_2$	$\mathcal{N}(0.3790, 0.1)$	$0.374^{+0.057}_{-0.080}$	$0.354^{+0.073}_{-0.064}$	$0.352^{+0.076}_{-0.062}$
$\theta [^\circ]$	$\mathcal{U}(-90, 90)$	–	$-16.9^{+4.4}_{-59.7}$	$-4^{+17}_{-73}$
$f$	$\mathcal{U}(0, 0.5)$	–	$0.173^{+0.167}_{-0.098}$	$0.052^{+0.146}_{-0.052}$
$\log \mathcal{Z}$	–	70510.951	70511.087	–

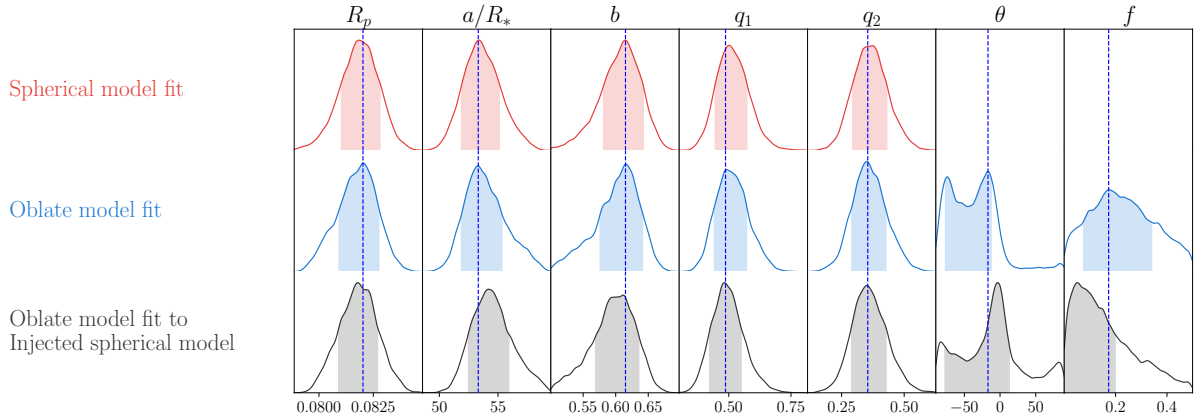


Figure 5.9: Posterior distribution of relevant parameters of the competing models for Kepler-46 b. The blue vertical line indicates the maximum likelihood (ML) solution for the oblate model. The shaded region corresponds to the 68% shortest confidence interval (Andrae, 2010) around the ML estimate.

data are probably not spurious but precise photometric observation is needed to increase the evidence for the oblate model and better constrain oblateness.

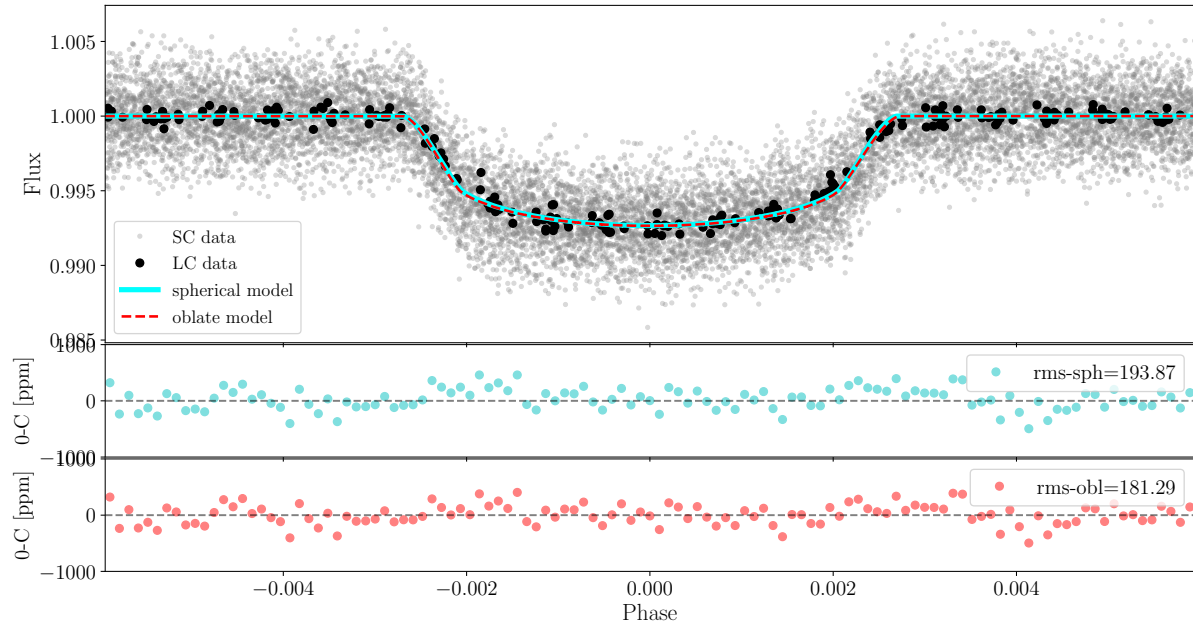


Figure 5.10: Model fits to Kepler-46 b data and the 5 minute binned residuals for both models.

### Kepler-302 c, TOI-216 c, and Kepler-167 e:

Similar analysis as for Kepler-46b was performed on the other planets: Kepler-302 c, TOI-216 c, and Kepler-167 e. The posterior distributions of the oblate model fits indicate a value of  $f$  consistent with zero (Fig. 5.11). In all cases, the Bayes factor is less than 1 in favour of the spherical planet model over the oblate model. However, an oblateness as large as Saturn is not ruled out at the  $1\sigma$  upper limit. More precise data would be required to better constrain the oblateness of these planets.

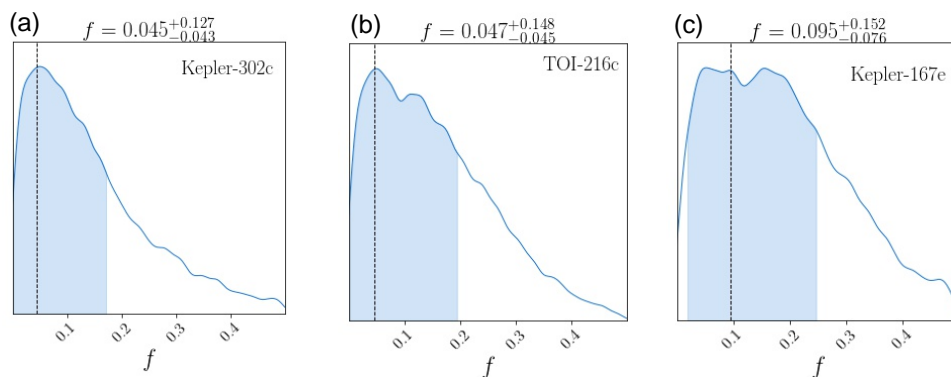


Figure 5.11: 1D posterior distribution of  $f$  for Kepler-302 c, TOI-216 c, and Kepler-167 e.



### 5.6.4 Outlook

The analyses performed in this section shows the challenges involved in detecting oblateness. Most of the identified targets orbit faint stars making it difficult to obtain precise light-curves required to detect oblateness. Further photometric and/or spectroscopic observations would prove useful in better constraining their oblateness. Unfortunately, these targets are not ideal targets for RV follow-up due to their faintness.

The most promising target analysed is Kepler-46 b which shows a hint of oblateness. The oblateness signal was found to be consistent between different groups of transits suggesting a robust detection. Further injection and recovery test also indicate that the noise in the data cannot be responsible for the recovered oblateness. The estimated oblateness suggests a faster rotation rate ( $23.9 \pm 10 \text{ km s}^{-1}$ ) than the planets of the Solar system. However, a similar fast rotation rate of  $25 \text{ km s}^{-1}$  was measured for  $\beta$  Pic b from rotational broadening of CO absorption line in its NIR spectra (Snellen et al., 2014). The fast rotation rate of Kepler-46 b can be as a result of retaining most of its primordial angular momentum.

The null detection of oblateness in Kepler-302 c, TOI-216 c, and Kepler-167 e can be as a result of imprecise data or can imply that the planets have been tidally spun down.

# Chapter 6

## Conclusions

*“Part of the journey is the end.”*

— Tony Stark in *Avengers Endgame* 2019

---

*“But what feels like the end is often just another beginning.”*

This thesis has focused on the challenging search for, what I refer to as, elusive planetary features since they induce only very subtle signatures in the transit signals of the planet. In the last three chapters I have described strategies and tools to facilitate the detection of rings, tidal deformation, and oblateness in transiting exoplanets. In this chapter, I summarise some of the main results and outputs of this thesis and outline some possible future work.

### 6.1 Summary

The first feature investigated in this thesis is exorings and their effects on transit light-curves. I described the SOAP3.0 ringed planet tool which I helped develop and improve during the Ph.D. I incorporated state-of-the-art Bayesian fitting methods (based on `dynesty`) that allowed comparison of models with and without rings. I also included Gaussian Processes (based on `celerite`) allowing to simultaneously model the noise and systematics in the data while fitting the transit signal. Since the presence of rings can inflate the inferred radius of a planet and lead to underestimation of its density, I used SOAP3.0 to model the *K2* light curve of HIP 41378 f showing that rings can proffer a possible explanation for its anomalously low density. However, further observations of this planet is necessary to ascertain its nature. A proposal (in which I was CoI) to observe this target using *HST* was accepted which will allow to further probe the ring scenario.

The second feature investigated is tidal deformation which occurs for planets orbiting close to the Roche limit of their stars. I showed that this deformation can be detected from precise transit light-curves of these planets. This was done by adapting a transit tool with a simple ellipsoidal shape model formulated by Correia (2014). The formulation allows to measure the second order fluid Love number,  $h_f$ , of a planet from fitting the transit observation with the ellipsoidal transit model. The Love number can help constrain the interior structure of a planet. The typical Love number of a Jupiter-like giant planet is around 1.5 (Durante et al., 2020). A lower measured value would suggest a planet with higher core mass whereas a higher value would indicate a more diluted and extended core (Kramm et al., 2011). Although there are other methods that allow the indirect measurement of the Love number (e.g., Batygin et al., 2009; Ragozzine and Wolf, 2009; Csizmadia et al., 2019), they require special planetary configurations such as significant orbital eccentricities, presence of eccentric planetary companions or long observational baseline. The method developed in this thesis is much simpler, requiring only the observation of precise transit light-curves of short period planets.

I used the developed ellipsoidal transit model to select confirmed planets expected to be most deformed showing the amplitudes of their deformation signal. This selection analysis led to the inclusion of one of the prime targets, WASP-103 b, as a priority target in *CHEOPS* Guaranteed Time Observations. The ongoing analysis of the obtained *CHEOPS* light-curves alongside other high precision observations of the target is providing good constraints on its Love number. The result is soon to be submitted for publication by the *CHEOPS feature.characterisation* working group. Due to data protection policy, the information regarding the deformation analyses of this target is not detailed in this thesis.

Lastly, I investigated the detectability of rotation-induced oblateness which I model with the ringed planet tool. I showed that oblateness could be better constrained by combining photometric and spectroscopic transit observations. However, the photometric observations are more sensitive to the induced effects of oblateness primarily due to better temporal resolution attainable for them. Although, RM signals include extra parameters ( $\nu \sin i_*$  and  $\lambda$ ), not relevant in light-curve analysis, that can allow more favorable detection of oblateness in misaligned planets and planets orbiting fast-rotating stars. I further used the tool to identify suitable targets for oblateness detection and probed their archival data. One of the analysed targets, Kepler-46 b showed hint of a

large oblateness of 0.173 indicating a fast rotation rate of  $\sim 24 \text{ km s}^{-1}$  that could have been inherited from the angular momentum of the disk from which it formed (Lissauer, 1995).

All the mentioned features will benefit from precise observations from upcoming instruments such as *PLATO* and *JWST*. The tools developed in this thesis will be useful in characterising the aforementioned features. Furthermore, as the limb darkening affects the detection of these features, observations in the NIR where limb darkening effect is almost negligible would significantly favour their detection.

### 6.1.1 Distinguishing the effects of different features

A common trend noticed with the probed features, is that they all lead to effects that are mostly concentrated at transit ingress and egress phases. One then wonders if it is possible to differentiate between the induced signal from tidal deformation, rings and oblateness.

The ring signature depends on the ring orientation and size of the gap between the planet and ring but is usually distinct from the other signatures as it shows more peaks at ingress and egress (Fig. 3.2; see also Ohta et al. 2009; Akinsanmi et al. 2018). Additionally, an estimate of the planetary density can help distinguish them since a planet with rings will appear larger and cause the planetary density to be underestimated (Zuluaga et al., 2015; Akinsanmi et al., 2020). More importantly, perhaps, rings and oblateness are not expected to be found in ultra-short period planets which are the targets for tidal deformation. Rings around such planets will be dynamically unstable as they will have  $R_{\text{Hill}} \simeq R_{\text{Roche}}$  and even the plane of any possible ring will closely align with the orbital plane, making it undetectable (§3.2.1). Oblateness is also not significant in short period planets as they generally rotate too slowly and the effect of tidal deformation dominates. Lastly, the bump throughout transit (Fig. 4.6) caused by the varying projected area of a tidally deformed planet is not present in the signals from the other features.

Therefore since the features are prominent at different orbital distances from the star, one can be certain about which feature is at play in different scenarios. The more confusing features can be rings and oblateness, which are both expected features of long period planets. However, multi-wavelength observations can help distinguish them since planet shape is not expected to vary with wavelength whereas rings can due to the

dependence of its opacity on wavelength. It is worth noting that rings and oblateness can even be simultaneously present for a planet as we see in Saturn. In this case, it is possible that only the feature with the largest signature will be detectable but the presence of the other will lead to systematic errors on the estimated parameters of the planet and feature. It will be interesting to develop a model that includes both features.

## 6.2 Future Prospects

### 6.2.1 On the search for exorings

Currently, the SOAP3.0 ringed planet model assumes a uniform, opaque ring around the planet. In a conservative sense, this is only similar to Saturn’s B-rings which are the most opaque. However, this does not fully represent our knowledge of the Saturnian ring system which consists of several rings of varying opacities and some gaps between them. Therefore, it would be interesting (or even necessary) to improve the ring model to include ring opacities and also gaps. These improvements will allow modelling the wavelength-dependent effects of rings and searching for rings of different properties around exoplanets. These improvements will introduce new parameters and degeneracies in some of the planet/ring parameters while fitting, so strategies to mitigate this problem will also need to be explored.

The search for exorings can also benefit from the power of machine learning methods which have been gaining traction in the analysis of astronomical datasets (e.g. Baumeister et al., 2020; Rao et al., 2021). Convolutional Neural Networks (CNN) have been shown to be well-suited for pattern recognition and classification problems after training on large datasets (e.g. Osborn et al., 2020; Olmschenk et al., 2021). A CNN can be trained on several thousands of *Kepler/K2/TESS* light-curves with injected ringed and non-ringed planet transit signals to evaluate its classification accuracy. The trained CNN model can then be fed with light-curves from different instruments to identify interesting ringed planet candidates for further analyses or observations where necessary.

Finally, complementary methods for detecting exorings can also be explored. Rings can reveal themselves in phase curves and occultation signals as the reflected light from the planet’s atmosphere can be amplified by the presence of rings (Dyudina et al., 2005; Santos et al., 2015; Sucerquia et al., 2020). The phase-dependent reflected light from rings can produce brightness variations different from a planet alone and can be used

to probe for rings, even around non-transiting planets. Although the effect will be most significant for short period planets, it could help identify silicate rings around planets within the snow-line.

### 6.2.2 Impact of planet shape on atmospheric characterisation

An interesting area of investigation is the impact of tidal deformation on atmospheric characterisation. The sky projected area of a deformed planet displays a sinusoidal variation across the entire orbital phase (see Fig. 6.1). Atmospheric characterisation of ultra-hot Jupiters via phase curve measurements attempt to correct for this tidal deformation effect (e.g. Delrez et al., 2016; Lendl et al., 2017; Kreidberg et al., 2018) using the theoretical calculations from Budaj (2011) and Leconte et al. (2011). However, these corrections are not entirely accurate as they implicitly assume an interior structure for the planet when computing the expected deformation and projected area. An inaccurate correction can bias the night- and day-side temperatures estimated from the phase curve.

With the expected precision of *JWST* data, it will be possible to use an ellipsoidal planet transit model to measure the planets deformation and observationally determine the projected shape of the planet at every phase which accounts for the tidal deformation more accurately. Furthermore, the impact of tidal deformation on transmission spectra can be studied using the ellipsoidal model rather than spherical models. Lendl et al. (2017) suggested that enhanced features in the transmission spectra of WASP-103 b could be due to its deformation but this remains to be understood and can be investigated using the ellipsoidal planet model.

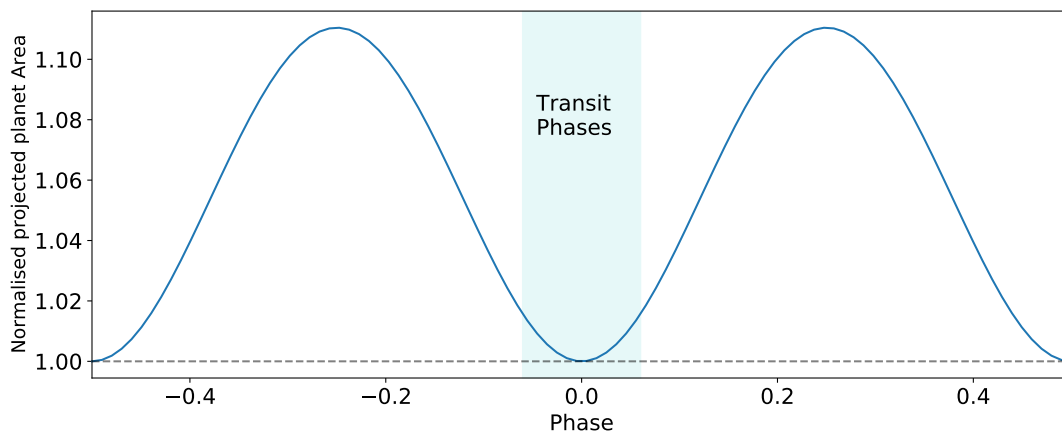


Figure 6.1: Projected area of deformed WASP-103b as a function of orbital phase. The area is normalised to the projected area at mid-transit (zero phase).

# Glossary

$J_2$	Planet second order quadruple moment
$K$	RV semi-amplitude
$M_*$	Stellar Mass
$M_{\text{Jup}}$	Jupiter Mass
$M_{\oplus}$	Earth Mass
$M_p$	Planet Mass
$N$	Noise level of data
$P_{\text{rot}}$	Planet rotation period
$R_p$	Planet radius
$R_L$	Laplace radius
$R_*$	Stellar radius
$R_{\text{Jup}}$	Jupiter Radius
$R_v$	Radius of a sphere that encloses same volume as an ellipsoid $(r_1 r_2 r_3)^{1/3}$
$R_{eq}$	Equatorial radius of an oblate planet
$R_{pol}$	Polar radius of an oblate planet
$S_{obl}$	Amplitude of oblateness signature
$\bar{R}_p$	Mean radius of an oblate planet $\sqrt{R_{eq} R_{pol}}$
$\Delta R$	Radial deformation of a planet due to tides
$\delta$	Transit depth
$\lambda$	Spin-orbit angle from RM signal
$\mathcal{B}_{12}$	Bayes Factor comparing evidence of models 1 and 2
$\mathcal{D}_r$	Percentage deformation of a planet
$\nu$	True anomaly
$\omega$	Argument of periastron
$\rho_p$	Planet density
$\rho_r$	Density of ring materials
$\theta$	Obliquity (of ring or planet)
$a/R_*$	Semi-major axis of planet orbit in units of stellar radii

$b$	Transit impact parameter
$e$	Orbital eccentricity
$f$	Planet oblateness
$h_f$	Planet second fluid Love number
$i_p$	Orbital inclination of planet
$i_r$	Ring inclination
$q$	Asymmetry parameter of a triaxial ellipsoid
$q_1, q_2$	Re-parameterized quadratic LDCs according to (Kipping, <a href="#">2013a</a> )
$r_1$	Equatorial semi-axis of the triaxial ellipsoid pointing towards the star
$r_2$	Equatorial semi-axis of the triaxial ellipsoid along the orbital direction
$r_3$	Polar semi-axis of the triaxial ellipsoid
$r_{\text{in}}$	Ring inner radius
$r_{\text{out}}$	Ring outer radius
$v \sin i_*$	Projected stellar rotational velocity
<b>AU</b>	Astronomical Units
<b>BLS</b>	Box-Least-Square
<b>ESO</b>	European Southern Observatory
<b>GP</b>	Gaussian Processes
<b>LC</b>	long-cadence
<b>LDCs</b>	limb darkening coefficients
<b>LS</b>	Lomb-Scargle
<b>MAST</b>	Mikulski Archive for Space Telescopes
<b>RM</b>	Rossiter-McLaughlin
<b>RV</b>	Radial Velocity
<b>SC</b>	short-cadence
<b>SG</b>	Savitzky-Golay
<b>TTV</b>	transit timing variations



# Bibliography

- Adams, E. R., S Seager, and L Elkins-Tanton (2008). “Ocean Planet or Thick Atmosphere: On the Mass-Radius Relationship for Solid Exoplanets with Massive Atmospheres”. *ApJ* 673.2, pp. 1160–1164. DOI: [10.1086/524925](https://doi.org/10.1086/524925) (Cited on page [55](#)).
- Addison, B. C., C. G. Tinney, D. J. Wright, and D Bayliss (2016). “Spinorbit Alignment for Three Transiting Hot Jupiters: WASP-103b, WASP-87b, and WASP-66b”. *The Astrophysical Journal* 823.1, p. 29 (Cited on page [16](#)).
- Adibekyan, V. et al. (2021). “The Chemical link between stars and their rocky planets” (Cited on page [59](#)).
- Agol, E., J. Steffen, R. Sari, and W. Clarkson (2005). “On detecting terrestrial planets with timing of giant planet transits”. *Monthly Notices of the Royal Astronomical Society* 359.2, pp. 567–579. DOI: [10.1111/j.1365-2966.2005.08922.x](https://doi.org/10.1111/j.1365-2966.2005.08922.x) (Cited on page [12](#)).
- Ahlers, J. P. et al. (2020). “KELT-9 bs Asymmetric TESS Transit Caused by Rapid Stellar Rotation and SpinOrbit Misalignment”. *The Astronomical Journal* 160.1, p. 4. DOI: [10.3847/1538-3881/ab8fa3](https://doi.org/10.3847/1538-3881/ab8fa3) (Cited on page [16](#)).
- Aizawa, M., K. Masuda, H. Kawahara, and Y. Suto (2018). “Systematic search for rings around Kepler planet candidates: Constraints on ring size and occurrence rate”. *arXiv* 155.5, p. 206. DOI: [10.3847/1538-3881/aab9a1](https://doi.org/10.3847/1538-3881/aab9a1) (Cited on page [38](#)).
- Aizawa, M., S. Uehara, K. Masuda, H. Kawahara, and Y. Suto (2017). “Toward Detection of Exoplanetary Rings via Transit Photometry: Methodology and a Possible Candidate”. *The Astronomical Journal* 153.4, p. 193 (Cited on page [38](#)).
- Akinsanmi, B., M. Oshagh, N. C. Santos, and S. C. C. Barros (2018). “Detecting transit signatures of exoplanetary rings using SOAP3.0”. *Astronomy & Astrophysics* 609, A21. DOI: [10.1051/0004-6361/201731215](https://doi.org/10.1051/0004-6361/201731215) (Cited on pages [38](#), [41–44](#), [48](#), [85](#), [98](#), [110](#)).
- Akinsanmi, B. et al. (2019). “Detectability of shape deformation in short-period exoplanets”. *Astronomy and Astrophysics* 621, A117. DOI: [10.1051/0004-6361/201834215](https://doi.org/10.1051/0004-6361/201834215) (Cited on pages [12](#), [98](#)).
- Akinsanmi, B. et al. (2020). “Can planetary rings explain the extremely low density of HIP 41378f?” *Astronomy & Astrophysics* 635, p. L8. DOI: [10.1051/0004-6361/202037618](https://doi.org/10.1051/0004-6361/202037618) (Cited on pages [42](#), [52](#), [110](#)).

- Alonso, R. et al. (2004). “TrES-1: The Transiting Planet of a Bright K0 V Star”. *The Astrophysical Journal* 613.2, pp. L153–L156. DOI: [10.1086/425256](https://doi.org/10.1086/425256) (Cited on page 9).
- Anderson, D. R. et al. (2015). “THE WELL-ALIGNED ORBIT OF WASP-84b: EVIDENCE FOR DISK MIGRATION OF A HOT JUPITER”. *The Astrophysical Journal* 800.1, p. L9. DOI: [10.1088/2041-8205/800/1/19](https://doi.org/10.1088/2041-8205/800/1/19) (Cited on page 14).
- Andrae, R. (2010). “Error estimation in astronomy: A guide” (Cited on page 105).
- Arkhyrov, O. V., M. L. Khodachenko, and A. Hanslmeier (2021). “Revealing peculiar exoplanetary shadows from transit light curves”. *Astronomy and Astrophysics* 646, A136. DOI: [10.1051/0004-6361/202039050](https://doi.org/10.1051/0004-6361/202039050) (Cited on page 38).
- Auvergne, M. et al. (2009). “The CoRoT satellite in flight: Description and performance”. *Astronomy and Astrophysics* 506.1, pp. 411–424. DOI: [10.1051/0004-6361/200810860](https://doi.org/10.1051/0004-6361/200810860) (Cited on page 9).
- Bakos, G., J. Lázár, I. Papp, P. Sári, and E. M. Green (2002). “System Description and First Light Curves of the Hungarian Automated Telescope, an Autonomous Observatory for Variability Search”. *Publications of the Astronomical Society of the Pacific* 114.799, pp. 974–987. DOI: [10.1086/342382](https://doi.org/10.1086/342382) (Cited on page 9).
- Barnes, J. W. and J. J. Fortney (2003). “Measuring the Oblateness and Rotation of Transiting Extrasolar Giant Planets”. *The Astrophysical Journal* 588.1, pp. 545–556. DOI: [10.1086/373893](https://doi.org/10.1086/373893) (Cited on pages 30, 70, 84, 87, 90, 94).
- Barnes, J. W. and J. J. Fortney (2004). “Transit Detectability of Ring Systems around Extrasolar Giant Planets”. *The Astrophysical Journal* 616.2, p. 1193 (Cited on pages 38, 43, 85).
- Barragán, O. and D. Gandolfi (2017). *Exotrending: Fast and easy-to-use light curve detrending software for exoplanets* (Cited on page 23).
- Barros, S. C. C. et al. (2014a). “Revisiting the transits of CoRoT-7b at a lower activity level”. *A&A* 569, A74. DOI: [10.1051/0004-6361/201423939](https://doi.org/10.1051/0004-6361/201423939) (Cited on page 81).
- Barros, S. C. C. et al. (2020). “Improving transit characterisation with Gaussian process modelling of stellar variability” (Cited on page 21).
- Barros, S. C. et al. (2014b). “SOPHIE velocimetry of Kepler transit candidates”. *Astronomy and Astrophysics* 561, p. 1. DOI: [10.1051/0004-6361/201323067](https://doi.org/10.1051/0004-6361/201323067) (Cited on page 10).
- Batygin, K., P. Bodenheimer, and G. Laughlin (2009). “Determination of the interior structure of transiting planets in multiple-planet systems”. *Astrophysical Journal* 704.1 PART 2, p. L49. DOI: [10.1088/0004-637X/704/1/L49](https://doi.org/10.1088/0004-637X/704/1/L49) (Cited on page 109).
- Baumeister, P. et al. (2020). “Machine-learning Inference of the Interior Structure of Low-mass Exoplanets”. *The Astrophysical Journal* 889.1, p. 42. DOI: [10.3847/1538-4357/ab5d32](https://doi.org/10.3847/1538-4357/ab5d32) (Cited on pages 60, 81, 111).

- Beichman, C. et al. (2014). “Observations of Transiting Exoplanets with the James Webb Space Telescope ( JWST )”. *Publications of the Astronomical Society of the Pacific* 126.946, p. 1134 (Cited on pages [10](#), [76](#), [100](#)).
- Benz, W. et al. (2020). “The CHEOPS mission”. *Experimental Astronomy* 51.1, pp. 109–151. DOI: [10.1007/s10686-020-09679-4](#) (Cited on page [9](#)).
- Biersteker, J. and H. Schlichting (2017). “Determining Exoplanetary Oblateness Using Transit Depth Variations”. *The Astronomical Journal* 154.4, p. 164. DOI: [10.3847/1538-3881/aa88c2](#) (Cited on pages [84](#), [90](#)).
- Birkby, J. L. et al. (2014). “WTS-2 b: A hot Jupiter orbiting near its tidal destruction radius around a K dwarf”. *Monthly Notices of the Royal Astronomical Society* 440.2, pp. 1470–1489. DOI: [10.1093/mnras/stu343](#) (Cited on page [66](#)).
- Boisse, I, X Bonfils, and N. C. Santos (2012). “SOAP. A tool for the fast computation of photometry and radial velocity induced by stellar spots”. *\aap* 545, A109. DOI: [10.1051/0004-6361/201219115](#) (Cited on page [41](#)).
- Bonfanti, A. et al. (2021). “CHEOPS observations of the HD 108236 planetary system: a fifth planet, improved ephemerides, and planetary radii”. *Astronomy & Astrophysics* 646, A157. DOI: [10.1051/0004-6361/202039608](#) (Cited on pages [17](#), [21](#)).
- Bonfils, X. et al. (2013). “The HARPS search for southern extra-solar planets: XXXI. the M-dwarf sample”. *Astronomy and Astrophysics* 549, A109. DOI: [10.1051/0004-6361/201014704](#) (Cited on page [5](#)).
- Borucki, W. J. et al. (2010). “Kepler planet-detection mission: Introduction and first results”. *Science* 327.5968, pp. 977–980. DOI: [10.1126/science.1185402](#) (Cited on pages [3](#), [9](#)).
- Bouchy, F, F Pepe, and D Queloz (2001). “Fundamental photon noise limit to radial velocity measurements”. *\aap* 374, pp. 733–739. DOI: [10.1051/0004-6361:20010730](#) (Cited on pages [89](#), [100](#)).
- Bouchy, F et al. (2017). “Near-InfraRed Planet Searcher to Join HARPS on the ESO 3.6-metre Telescope”. *The Messenger* 169, pp. 21–27. DOI: [10.18727/0722-6691/5034](#) (Cited on page [100](#)).
- Braga-Ribas, F. et al. (2014). “A ring system detected around the Centaur (10199) Chariklo”. *Nature* 508.1, pp. 72–75. DOI: [10.1038/nature13155](#) (Cited on pages [36](#), [37](#)).
- Broeg, C et al. (2013). “CHEOPS: A transit photometry mission for ESA’s small mission programme”. *EPJ Web of Conferences*. European Physical Journal Web of Conferences 47. Ed. by R. Saglia, p. 03005. DOI: [10.1051/epjconf/20134703005](#) (Cited on page [9](#)).
- Brown, T. M., D. Charbonneau, R. L. Gilliland, R. W. Noyes, and A. Burrows (2001). “Hubble Space Telescope TimeSeries Photometry of the Transiting Planet of HD 209458”. *The Astrophysical Journal* 552.2, pp. 699–709. DOI: [10.1086/320580](#) (Cited on page [9](#)).

- Brugger, B., O. Mousis, M. Deleuil, and F. Deschamps (2017). “Constraints on Super-Earth Interiors from Stellar Abundances”. *The Astrophysical Journal* 850.1, p. 93. DOI: [10.3847/1538-4357/aa965a](https://doi.org/10.3847/1538-4357/aa965a) (Cited on page 59).
- Budaj, J (2011). “The Reflection Effect in Interacting Binaries or in Planet-Star Systems”. *The Astronomical Journal* 141.2, p. 59 (Cited on pages 61, 66, 70, 112).
- Buhler, P. B. et al. (2016). “DYNAMICAL CONSTRAINTS ON THE CORE MASS OF HOT JUPITER HAT-P-13B”. *The Astrophysical Journal* 821.1, p. 26. DOI: [10.3847/0004-637x/821/1/26](https://doi.org/10.3847/0004-637x/821/1/26) (Cited on page 61).
- Burton, J. R. et al. (2014). “TIDALLY DISTORTED EXOPLANETS: DENSITY CORRECTIONS FOR SHORT-PERIOD HOT-JUPITERS BASED SOLELY ON OBSERVABLE PARAMETERS”. *The Astrophysical Journal* 789.2, p. 113. DOI: [10.1088/0004-637x/789/2/113](https://doi.org/10.1088/0004-637x/789/2/113) (Cited on pages 61, 70).
- Cabrera, J., M. F. Jiménez, A. G. Muñoz, and J. Schneider (2018). *Special Cases: Moons, Rings, Comets, and Trojans*, pp. 3433–3450. DOI: [10.1007/978-3-319-55333-7\\_{\\\_}158](https://doi.org/10.1007/978-3-319-55333-7_{\_}158) (Cited on page 16).
- Cameron, A. C. (2012). “Extrasolar planets: Astrophysical false positives”. *Nature* 492.7427, pp. 48–50. DOI: [10.1038/492048a](https://doi.org/10.1038/492048a) (Cited on page 10).
- Carry, B (2012). “Density of asteroids”. *Planetary and Space Science* 73.1, pp. 98–118. DOI: [10.1016/j.pss.2012.03.009](https://doi.org/10.1016/j.pss.2012.03.009) (Cited on page 53).
- Carter, J. A. and J. N. Winn (2009). “Parameter estimation from time-series data with correlated errors: A wavelet-based method and its application to transit light curves”. *Astrophysical Journal* 704.1, pp. 51–67. DOI: [10.1088/0004-637x/704/1/51](https://doi.org/10.1088/0004-637x/704/1/51) (Cited on page 27).
- (2010a). “Empirical constraints on the oblateness of an exoplanet”. *Astrophysical Journal* 709.2, pp. 1219–1229. DOI: [10.1088/0004-637x/709/2/1219](https://doi.org/10.1088/0004-637x/709/2/1219) (Cited on pages 40, 61, 84, 86–89, 92).
- (2010b). “The detectability of transit depth variations due to exoplanetary oblateness and spin precession”. *Astrophysical Journal* 716.1, pp. 850–856. DOI: [10.1088/0004-637x/716/1/850](https://doi.org/10.1088/0004-637x/716/1/850) (Cited on pages 61, 89, 90).
- Chakrabarty, A. and S. Sengupta (2019). “Precise Photometric Transit Follow-up Observations of Five Close-in Exoplanets: Update on Their Physical Properties”. *The Astronomical Journal* 158.1, p. 39. DOI: [10.3847/1538-3881/ab24dd](https://doi.org/10.3847/1538-3881/ab24dd) (Cited on page 66).
- Chandrasekhar, S (1969). *Ellipsoidal figures of equilibrium* (Cited on page 61).
- Chaplin, W. J., H. M. Cegla, C. A. Watson, G. R. Davies, and W. H. Ball (2019). “Filtering Solar-Like Oscillations for Exoplanet Detection in Radial Velocity Observations”. *AJ* 157.4, p. 163. DOI: [10.3847/1538-3881/ab0c01](https://doi.org/10.3847/1538-3881/ab0c01) (Cited on page 88).
- Charbonneau, D., T. M. Brown, D. W. Latham, and M. Mayor (2000). “Detection of Planetary Transits Across a Sun-like Star”. *The Astrophysical Journal* 529.1, pp. L45–L48. DOI: [10.1086/312457](https://doi.org/10.1086/312457) (Cited on pages 7, 9).

- Charbonneau, D. et al. (2005). “Detection of Thermal Emission from an Extrasolar Planet”. *The Astrophysical Journal* 626.1, pp. 523–529. DOI: [10.1086/429991](https://doi.org/10.1086/429991) (Cited on page 9).
- Charnoz, S., R. M. Canup, A. Crida, and L. Dones (2018a). “The Origin of Planetary Ring Systems”. *Planetary Ring Systems*. Vol. 2. Cambridge University Press, pp. 517–538. DOI: [10.1017/9781316286791.018](https://doi.org/10.1017/9781316286791.018) (Cited on page 37).
- Charnoz, S., A. Crida, and R. Hyodo (2018b). *Rings in the Solar System: A Short Review*. Vol. 4. 1, pp. 375–394. DOI: [10.1007/978-3-319-55333-7\\_{\\\_}54](https://doi.org/10.1007/978-3-319-55333-7_{\_}54) (Cited on pages 37, 39, 49).
- Chen, G et al. (2020). “Detection of Na in WASP-21b’s lower and upper atmosphere”. *Astronomy and Astrophysics* 642. DOI: [10.1051/0004-6361/202038661](https://doi.org/10.1051/0004-6361/202038661) (Cited on page 21).
- Chen, J. and D. Kipping (2017). “Probabilistic Forecasting of the Masses and Radii of Other Worlds”. *ApJ* 834.1, p. 17. DOI: [10.3847/1538-4357/834/1/17](https://doi.org/10.3847/1538-4357/834/1/17) (Cited on page 53).
- Chiavassa, A et al. (2017). “Measuring stellar granulation during planet transits”. *Astronomy & Astrophysics* 597, A94. DOI: [10.1051/0004-6361/201528018](https://doi.org/10.1051/0004-6361/201528018) (Cited on page 81).
- Claret, A (2000). “A new non-linear limb-darkening law for LTE stellar atmosphere models: Calculations for  $-5.0 \leq \log[M/H] \leq +1$ ,  $2000 \leq T_{\text{eff}} \leq 50000$  K at several surface gravities”. *Astronomy and Astrophysics* 363.3, pp. 1081–1090 (Cited on page 11).
- Claret, A and S Bloemen (2011). “Gravity and limb-darkening coefficients for the Kepler, CoRoT, Spitzer, uvby, UBVRIJHK, and Sloan photometric systems”. *\aap* 529, A75. DOI: [10.1051/0004-6361/201116451](https://doi.org/10.1051/0004-6361/201116451) (Cited on pages 11, 48, 88, 91, 104).
- Correia, A. C. M. (2014). “Transit light curve and inner structure of close-in planets”. *\aap* 570. DOI: [10.1051/0004-6361/201424733](https://doi.org/10.1051/0004-6361/201424733) (Cited on pages 60, 62, 63, 65, 67, 70, 77, 109).
- Correia, A. C., G. Boué, J. Laskar, and A. Rodríguez (2014). “Deformation and tidal evolution of close-in planets and satellites using a Maxwell viscoelastic rheology”. *Astronomy and Astrophysics* 571, pp. 1–16. DOI: [10.1051/0004-6361/201424211](https://doi.org/10.1051/0004-6361/201424211) (Cited on page 60).
- Csizmadia, S., H Hellard, and A. M. Smith (2019). “An estimate of the  $k_2$  Love number of WASP-18Ab from its radial velocity measurements”. *Astronomy and Astrophysics* 623. DOI: [10.1051/0004-6361/201834376](https://doi.org/10.1051/0004-6361/201834376) (Cited on pages 61, 77, 109).
- Csizmadia, S. et al. (2012). “The effect of stellar limb darkening values on the accuracy of the planet radii derived from photometric transit observations”. *Astronomy & Astrophysics* 549, A9. DOI: [10.1051/0004-6361/201219888](https://doi.org/10.1051/0004-6361/201219888) (Cited on pages 12, 78).
- Csizmadia, S. (2018). “Stellar Limb Darkenings Effects on Exoplanet Characterization”. *Handbook of Exoplanets*. Cham: Springer International Publishing, pp. 1403–1417. DOI: [10.1007/978-3-319-55333-7\\_{\\\_}41](https://doi.org/10.1007/978-3-319-55333-7_{\_}41) (Cited on page 78).
- Cubillos, P. et al. (2016). “ON CORRELATED-NOISE ANALYSES APPLIED TO EXOPLANET LIGHT CURVES”. *The Astronomical Journal* 153.1, p. 3. DOI: [10.3847/1538-3881/153/1/3](https://doi.org/10.3847/1538-3881/153/1/3) (Cited on pages 27, 28).

- Damasso, M. et al. (2020). “A precise architecture characterization of the  $\pi$  Mensae planetary system”. *Astronomy and Astrophysics* 642. DOI: [10.1051/0004-6361/202038416](https://doi.org/10.1051/0004-6361/202038416) (Cited on page 5).
- Dawson, R. I. and J. A. Johnson (2018). *Origins of Hot Jupiters*. DOI: [10.1146/annurev-astro-081817-051853](https://doi.org/10.1146/annurev-astro-081817-051853) (Cited on page 58).
- Delrez, L. et al. (2016). “WASP-121 b: A hot Jupiter close to tidal disruption transiting an active F star”. *Monthly Notices of the Royal Astronomical Society* 458.4, pp. 4025–4043. DOI: [10.1093/mnras/stw522](https://doi.org/10.1093/mnras/stw522) (Cited on pages 61, 66, 112).
- Delrez, L. et al. (2018). “High-precision multiwavelength eclipse photometry of the ultra-hot gas giant exoplanet WASP-103 b”. *Monthly Notices of the Royal Astronomical Society* 474.2, pp. 2334–2351. DOI: [10.1093/mnras/stx2896](https://doi.org/10.1093/mnras/stx2896) (Cited on pages 61, 81).
- Deming, D., S. Seager, L. J. Richardson, and J. Harrington (2005). “Infrared radiation from an extrasolar planet”. *Nature* 434.7034, pp. 740–743. DOI: [10.1038/nature03507](https://doi.org/10.1038/nature03507) (Cited on page 9).
- Diaz-Cordovez, J and A Gimenez (1992). “A new nonlinear approximation to the limb-darkening of hot stars”. *Astronomy and astrophysics (Berlin. Print)* 259.1, pp. 227–231 (Cited on page 11).
- Donati, J.-F. et al. (2018). “SPIRou: A NIR Spectropolarimeter/High-Precision Velocimeter for the CFHT”. *Handbook of Exoplanets*. Springer International Publishing, p. 107. DOI: [10.1007/978-3-319-55333-7\\_{\\\_}107](https://doi.org/10.1007/978-3-319-55333-7_{\_}107) (Cited on page 100).
- Dorn, C. et al. (2015). “Can we constrain the interior structure of rocky exoplanets from mass and radius measurements?” *Astronomy and Astrophysics* 577, A83. DOI: [10.1051/0004-6361/201424915](https://doi.org/10.1051/0004-6361/201424915) (Cited on page 59).
- Dorn, C. et al. (2017). “A generalized Bayesian inference method for constraining the interiors of super Earths and sub-Neptunes”. *Astronomy and Astrophysics* 597, A37. DOI: [10.1051/0004-6361/201628708](https://doi.org/10.1051/0004-6361/201628708) (Cited on page 59).
- Doyle, A. P., G. R. Davies, B. Smalley, W. J. Chaplin, and Y. Elsworth (2014). “Determining stellar macroturbulence using asteroseismic rotational velocities from Kepler”. *Monthly Notices of the Royal Astronomical Society* 444.4, pp. 3592–3602. DOI: [10.1093/mnras/stu1692](https://doi.org/10.1093/mnras/stu1692) (Cited on page 89).
- Dumusque, X., I. Boisse, and N. C. Santos (2014). “SOAP 2.0: A tool to estimate the photometric and radial velocity variations induced by stellar spots and plages”. *Astrophysical Journal* 796.2, p. 132. DOI: [10.1088/0004-637X/796/2/132](https://doi.org/10.1088/0004-637X/796/2/132) (Cited on page 41).
- Durante, D. et al. (2020). “Jupiter’s Gravity Field Halfway Through the Juno Mission”. *Geophysical Research Letters* 47.4, e2019GL086572. DOI: [10.1029/2019GL086572](https://doi.org/10.1029/2019GL086572) (Cited on pages 60, 109).
- Dyudina, U. A. et al. (2005). “Phase Light Curves for Extrasolar Jupiters and Saturns”. *The Astrophysical Journal* 618.2, pp. 973–986. DOI: [10.1086/426050](https://doi.org/10.1086/426050) (Cited on page 111).

- Espinoza, N. and A. Jordán (2015). “Limb darkening and exoplanets: testing stellar model atmospheres and identifying biases in transit parameters”. *Monthly Notices of the Royal Astronomical Society* 450.2, pp. 1879–1899. DOI: [10.1093/mnras/stv744](https://doi.org/10.1093/mnras/stv744) (Cited on pages [12](#), [77](#), [79](#)).
- (2016). “Limb darkening and exoplanets II. Choosing the best law for optimal retrieval of transit parameters”. *Monthly Notices of the Royal Astronomical Society* 457.4, pp. 3573–3581. DOI: [10.1093/mnras/stw224](https://doi.org/10.1093/mnras/stw224) (Cited on page [78](#)).
- Espinoza, N. et al. (2019). “Access: A featureless optical transmission spectrum for WASP-19b from Magellan/IMACS”. *Monthly Notices of the Royal Astronomical Society* 482.2, pp. 2065–2087. DOI: [10.1093/mnras/sty2691](https://doi.org/10.1093/mnras/sty2691) (Cited on pages [19](#), [20](#)).
- Esposito, M. et al. (2014). “The GAPS programme with HARPS-N at TNG III: The retrograde orbit of HAT-P-18b”. *Astronomy and Astrophysics* 564, p. 13. DOI: [10.1051/0004-6361/201423735](https://doi.org/10.1051/0004-6361/201423735) (Cited on page [14](#)).
- Faria, J. P. et al. (2020). “Decoding the radial velocity variations of HD 41248 with ESPRESSO”. *Astronomy and Astrophysics* 635. DOI: [10.1051/0004-6361/201936389](https://doi.org/10.1051/0004-6361/201936389) (Cited on page [81](#)).
- Faria, J. P. d. S. (2018). “Exoplanet detection in metal-poor stars”. *PhDT* (Cited on page [19](#)).
- Fischer, D. A. et al. (2015). “Exoplanet Detection Techniques”. DOI: [10.2458/azu\\_{\\\_}uapress{\\\_}9780816531240-ch031](https://doi.org/10.2458/azu_{\_}uapress{\_}9780816531240-ch031) (Cited on page [5](#)).
- Foreman-Mackey, D., E. Agol, S. Ambikasaran, and R. Angus (2017). “Fast and Scalable Gaussian Process Modeling with Applications to Astronomical Time Series”. *The Astronomical Journal* 154.6, p. 220. DOI: [10.3847/1538-3881/aa9332](https://doi.org/10.3847/1538-3881/aa9332) (Cited on pages [21](#), [81](#)).
- Foreman-Mackey, D., D. W. Hogg, D. Lang, and J. Goodman (2013). “emcee : The MCMC Hammer”. *Publications of the Astronomical Society of the Pacific* 125.925, pp. 306–312. DOI: [10.1086/670067](https://doi.org/10.1086/670067) (Cited on page [28](#)).
- Fortney, J. J., M. S. Marley, and J. W. Barnes (2007). “Planetary Radii across Five Orders of Magnitude in Mass and Stellar Insolation: Application to Transits”. *The Astrophysical Journal* 659.2, pp. 1661–1672. DOI: [10.1086/512120](https://doi.org/10.1086/512120) (Cited on page [59](#)).
- Fortney, J. J., R. I. Dawson, and T. D. Komacek (2021). “Hot Jupiters: Origins, Structure, Atmospheres”. *Journal of Geophysical Research: Planets*, pp. 1–28. DOI: [10.1029/2020je006629](https://doi.org/10.1029/2020je006629) (Cited on page [58](#)).
- Fressin, F. et al. (2013). “The false positive rate of Kepler and the occurrence of planets”. *Astrophysical Journal* 766.2, p. 81. DOI: [10.1088/0004-637X/766/2/81](https://doi.org/10.1088/0004-637X/766/2/81) (Cited on page [10](#)).
- Fulton, B. J., E. A. Petigura, S. Blunt, and E. Sinukoff (2018). “Radvel: The radial velocity modeling toolkit”. *Publications of the Astronomical Society of the Pacific* 130.986, p. 044504. DOI: [10.1088/1538-3873/aaaaa8](https://doi.org/10.1088/1538-3873/aaaaa8) (Cited on page [5](#)).
- Gaudi, B. S. and J. N. Winn (2007). “Prospects for the Characterization and Confirmation of Transiting Exoplanets via the Rossiter-[McLaughlin](#) Effect”. *The Astrophysical Journal* 655.1, pp. 550–563. DOI: [10.1086/509910](https://doi.org/10.1086/509910) (Cited on page [14](#)).

- Gelman, A. and D. B. Rubin (1992). “Inference from iterative simulation using multiple sequences”. *Statistical Science* 7.4, pp. 457–472. DOI: [10.1214/ss/1177011136](https://doi.org/10.1214/ss/1177011136) (Cited on page 28).
- Gettel, S. et al. (2016). “THE KEPLER-454 SYSTEM: A SMALL, NOT-ROCKY INNER PLANET, A JOVIAN WORLD, AND A DISTANT COMPANION”. *The Astrophysical Journal* 816.2, p. 95. DOI: [10.3847/0004-637x/816/2/95](https://doi.org/10.3847/0004-637x/816/2/95) (Cited on page 59).
- Gibson, N. P. (2014). “Reliable inference of exoplanet light-curve parameters using deterministic and stochastic systematics models”. *Monthly Notices of the Royal Astronomical Society* 445.4, pp. 3401–3414. DOI: [10.1093/mnras/stu1975](https://doi.org/10.1093/mnras/stu1975) (Cited on page 21).
- Gibson, N. P. et al. (2012). “A Gaussian process framework for modelling instrumental systematics: Application to transmission spectroscopy”. *Monthly Notices of the Royal Astronomical Society* 419.3, pp. 2683–2694. DOI: [10.1111/j.1365-2966.2011.19915.x](https://doi.org/10.1111/j.1365-2966.2011.19915.x) (Cited on page 21).
- Gilliland, R. L. et al. (2011). “Kepler mission stellar and instrument noise properties”. *Astrophysical Journal, Supplement Series* 197.1, p. 6. DOI: [10.1088/0067-0049/197/1/6](https://doi.org/10.1088/0067-0049/197/1/6) (Cited on page 18).
- Gillon, M. et al. (2014). “WASP-103 b: A new planet at the edge of tidal disruption”. *Astronomy and Astrophysics* 562, p. L3. DOI: [10.1051/0004-6361/201323014](https://doi.org/10.1051/0004-6361/201323014) (Cited on pages 61, 67).
- Goodman, J. and J. Weare (2010). “Ensemble samplers with affine invariance”. *Communications in Applied Mathematics and Computational Science* 5.1, pp. 65–80. DOI: [10.2140/camcos.2010.5.65](https://doi.org/10.2140/camcos.2010.5.65) (Cited on page 28).
- Grasset, O., J. Schneider, and C. Sotin (2009). “A study of the accuracy of mass-radius relationships for silicate-rich and ice-rich planets up to 100 earth masses”. *Astrophysical Journal* 693.1, pp. 722–733. DOI: [10.1088/0004-637X/693/1/722](https://doi.org/10.1088/0004-637X/693/1/722) (Cited on page 59).
- Guillot, T, A Burrows, W. B. Hubbard, J. I. Lunine, and D Saumon (1996). “Giant Planets at Small Orbital Distances”. *apjl* 459, p. L35. DOI: [10.1086/309935](https://doi.org/10.1086/309935) (Cited on page 89).
- Hamilton, D. P. and J. A. Burns (1991). “Orbital stability zones about asteroids”. *Icarus* 92.1, pp. 118–131. DOI: [10.1016/0019-1035\(91\)90039-V](https://doi.org/10.1016/0019-1035(91)90039-V) (Cited on page 39).
- (1992). “Orbital stability zones about asteroids. II. The destabilizing effects of eccentric orbits and of solar radiation”. *Icarus* 96.1, pp. 43–64. DOI: [10.1016/0019-1035\(92\)90005-R](https://doi.org/10.1016/0019-1035(92)90005-R) (Cited on page 38).
- Hartman, J. D. et al. (2016). “HAT-P-65b AND HAT-P-66b: TWO TRANSITING INFLATED HOT JUPITERS AND OBSERVATIONAL EVIDENCE FOR THE REINFLATION OF CLOSE-IN GIANT PLANETS”. *The Astronomical Journal* 152.6, p. 182. DOI: [10.3847/0004-6256/152/6/182](https://doi.org/10.3847/0004-6256/152/6/182) (Cited on page 66).
- Hébrard, G. et al. (2008). “Misaligned spin-orbit in the XO-3 planetary system?” *Astronomy and Astrophysics* 488.2, pp. 763–770. DOI: [10.1051/0004-6361:200810056](https://doi.org/10.1051/0004-6361:200810056) (Cited on page 14).



- Heising, M. Z., G. W. Marcy, and H. E. Schlichting (2015). “A Search for Ringed Exoplanets Using Kepler Photometry”. *The Astrophysical Journal* 814.1, p. 81 (Cited on pages 16, 38).
- Hellard, H., S. Csizmadia, S. Padovan, F. Sohl, and H. Rauer (2020). “HST /STIS Capability for Love Number Measurement of WASP-121b”. *The Astrophysical Journal* 889.1, p. 66. DOI: [10.3847/1538-4357/ab616e](https://doi.org/10.3847/1538-4357/ab616e) (Cited on page 82).
- Hellard, H. et al. (2019). “Retrieval of the fluid Love number  $k_2$  in exoplanetary transit curves”. DOI: [10.3847/1538-4357/ab2048](https://doi.org/10.3847/1538-4357/ab2048) (Cited on pages 98, 100).
- Henry, G. W., G. W. Marcy, R. P. Butler, and S. S. Vogt (2000). “A Transiting 51 Peglike Planet”. *The Astrophysical Journal* 529.1, pp. L41–L44. DOI: [10.1086/312458](https://doi.org/10.1086/312458) (Cited on page 9).
- Hestroffer, D (1997). “Centre to limb darkening of stars: New model and application to stellar interferometry”. *Astronomy and Astrophysics* 327.1, pp. 199–206 (Cited on page 11).
- Hippke, M., T. J. David, G. D. Mulders, and R. Heller (2019). “Wōtan : Comprehensive Time-series Detrending in Python”. *The Astronomical Journal* 158.4, p. 143. DOI: [10.3847/1538-3881/ab3984](https://doi.org/10.3847/1538-3881/ab3984) (Cited on page 20).
- Hippke, M. and R. Heller (2019). “Optimized transit detection algorithm to search for periodic transits of small planets”. *Astronomy and Astrophysics* 623.Ofir 2008, pp. 1–13. DOI: [10.1051/0004-6361/201834672](https://doi.org/10.1051/0004-6361/201834672) (Cited on page 20).
- Holczer, T. et al. (2016). “TRANSIT TIMING OBSERVATIONS FROM KEPLER . IX. CATALOG OF THE FULL LONG-CADENCE DATA SET”. *The Astrophysical Journal Supplement Series* 225.1, p. 9. DOI: [10.3847/0067-0049/225/1/9](https://doi.org/10.3847/0067-0049/225/1/9) (Cited on pages 12, 20, 23).
- Holman, M. J. et al. (2010). “Kepler-9: A System of Multiple Planets Transiting a Sun-Like Star, Confirmed by Timing Variations”. *Science* 330, p. 51. DOI: [10.1126/science.1195778](https://doi.org/10.1126/science.1195778) (Cited on page 12).
- Holman, M. J. (2005). “The Use of Transit Timing to Detect Terrestrial-Mass Extrasolar Planets”. *Science* 307.5713, pp. 1288–1291. DOI: [10.1126/science.1107822](https://doi.org/10.1126/science.1107822) (Cited on page 12).
- Howard, A. W. et al. (2010). “The Occurrence and Mass Distribution of Close-in Super-Earths, Neptunes, and Jupiters”. *Science* 330.6004, pp. 653–655. DOI: [10.1126/SCIENCE.1194854](https://doi.org/10.1126/SCIENCE.1194854) (Cited on page 5).
- Howard, A. W. et al. (2012). *Planet occurrence within 0.25AU of solar-type stars from Kepler*. DOI: [10.1088/0067-0049/201/2/15](https://doi.org/10.1088/0067-0049/201/2/15) (Cited on page 9).
- Howell, S. B. et al. (2014). “The K2 Mission: Characterization and Early Results”. *Publications of the Astronomical Society of the Pacific* 126.938, pp. 398–408. DOI: [10.1086/676406](https://doi.org/10.1086/676406) (Cited on page 9).
- Hut, P. (1980). “Stability of tidal equilibrium”. *Astronomy and Astrophysics* 92.1-2, pp. 167–170 (Cited on page 62).

- Jenkins, J. S. et al. (2020). “An ultrahot Neptune in the Neptune desert”. *Nature Astronomy* 4.12, pp. 1148–1157. DOI: [10.1038/s41550-020-1142-z](https://doi.org/10.1038/s41550-020-1142-z) (Cited on page 21).
- Jontof-Hutter, D., J. J. Lissauer, J. F. Rowe, and D. C. Fabrycky (2014). “Kepler-79’s Low Density Planets”. *ApJ* 785.1, p. 15. DOI: [10.1088/0004-637X/785/1/15](https://doi.org/10.1088/0004-637X/785/1/15) (Cited on page 46).
- Kaspi, Y. and A. P. Showman (2015). “ATMOSPHERIC DYNAMICS OF TERRESTRIAL EXOPLANETS OVER A WIDE RANGE OF ORBITAL AND ATMOSPHERIC PARAMETERS”. *The Astrophysical Journal* 804.1, p. 60. DOI: [10.1088/0004-637X/804/1/60](https://doi.org/10.1088/0004-637X/804/1/60) (Cited on page 84).
- Kass, R. E. and A. E. Raftery (1995). “Bayes Factors”. *Journal of the American Stat. Assoc.* 90.430, pp. 773–795 (Cited on pages 29, 30).
- Kellermann, C, A Becker, and R Redmer (2018). “Interior structure models and fluid Love numbers of exoplanets in the super-Earth regime”. *Astronomy and Astrophysics* 615, p. 39. DOI: [10.1051/0004-6361/201731775](https://doi.org/10.1051/0004-6361/201731775) (Cited on page 60).
- Kenworthy, M. A. and E. E. Mamajek (2015). “Modeling Giant Extrasolar Ring Systems in Eclipse and the Case of J1407b: Sculpting by Exomoons?” *The Astrophysical Journal* 800.2, p. 126 (Cited on page 38).
- Kipping, D. M. et al. (2016). “A Transiting Jupiter Analog”. *apj* 820, p. 112. DOI: [10.3847/0004-637X/820/2/112](https://doi.org/10.3847/0004-637X/820/2/112) (Cited on page 103).
- Kipping, D. et al. (2019). “A resonant pair of warm giant planets revealed by TESS”. *Monthly Notices of the Royal Astronomical Society* 486.4, pp. 4980–4986. DOI: [10.1093/mnras/stz1141](https://doi.org/10.1093/mnras/stz1141) (Cited on page 103).
- Kipping, D. M. (2009a). “Transit timing effects due to an exomoon”. *Monthly Notices of the Royal Astronomical Society* 392.1, pp. 181–189. DOI: [10.1111/j.1365-2966.2008.13999.x](https://doi.org/10.1111/j.1365-2966.2008.13999.x) (Cited on page 13).
- (2009b). “Transit timing effects due to an exomoon - II”. *Monthly Notices of the Royal Astronomical Society* 396.3, pp. 1797–1804. DOI: [10.1111/j.1365-2966.2009.14869.x](https://doi.org/10.1111/j.1365-2966.2009.14869.x) (Cited on page 13).
- Kipping, D. M. (2010a). “Binning is sinning: Morphological light-curve distortions due to finite integration time”. *Monthly Notices of the Royal Astronomical Society* 408.3, pp. 1758–1769. DOI: [10.1111/j.1365-2966.2010.17242.x](https://doi.org/10.1111/j.1365-2966.2010.17242.x) (Cited on page 103).
- Kipping, D. M. (2010b). “Investigations of approximate expressions for the transit duration”. *Monthly Notices of the Royal Astronomical Society* 407.1, pp. 301–313. DOI: [10.1111/j.1365-2966.2010.16894.x](https://doi.org/10.1111/j.1365-2966.2010.16894.x) (Cited on page 8).
- (2013a). “Efficient, uninformative sampling of limb darkening coefficients for two-parameter laws”. *Monthly Notices of the Royal Astronomical Society* 435.3, pp. 2152–2160. DOI: [10.1093/mnras/stt1435](https://doi.org/10.1093/mnras/stt1435) (Cited on pages 12, 16, 91, 114).

- Kipping, D. M. (2013b). “Parametrizing the exoplanet eccentricity distribution with the beta distribution”. *Monthly Notices of the Royal Astronomical Society: Letters* 434.1, pp. 51–55. DOI: [10.1093/mnrasl/slt075](https://doi.org/10.1093/mnrasl/slt075) (Cited on page 27).
- Kipping, D. M. (2016). “Efficient, uninformative sampling of limb-darkening coefficients for a three-parameter law”. *Monthly Notices of the Royal Astronomical Society* 455.2, pp. 1680–1690. DOI: [10.1093/mnras/stv2379](https://doi.org/10.1093/mnras/stv2379) (Cited on page 79).
- Kipping, D. M. and G. Tinetti (2010). “Nightside pollution of exoplanet transit depths”. *Monthly Notices of the Royal Astronomical Society* 407.4, pp. 2589–2598. DOI: [10.1111/j.1365-2966.2010.17094.x](https://doi.org/10.1111/j.1365-2966.2010.17094.x) (Cited on page 19).
- Kopal, Z. (1950). “Detailed Effects of Limb Darkening Upon Light and Velocity Curves of Close Binary Systems”. *Harvard College Observatory Circular* 454, pp. 1–12 (Cited on page 11).
- Kovács, G., S. Zucker, and T. Mazeh (2002). “A box-fitting algorithm in the search for periodic transits”. *Astronomy and Astrophysics* 391.1, pp. 369–377. DOI: [10.1051/0004-6361:20020802](https://doi.org/10.1051/0004-6361:20020802) (Cited on page 19).
- Kramm, U., N. Nettelmann, J. J. Fortney, R. Neuhäuser, and R. Redmer (2012). “Constraining the interior of extrasolar giant planets with the tidal Love number  $k_2$  using the example of HAT-P-13b”. *Astronomy and Astrophysics* 538. DOI: [10.1051/0004-6361/201118141](https://doi.org/10.1051/0004-6361/201118141) (Cited on page 60).
- Kramm, U., N. Nettelmann, R. Redmer, and D. J. Stevenson (2011). “On the degeneracy of the tidal Love number  $k_2$  in multi-layer planetary models: Application to Saturn and GJ 436b”. *Astronomy and Astrophysics* 528. DOI: [10.1051/0004-6361/201015803](https://doi.org/10.1051/0004-6361/201015803) (Cited on pages 59, 60, 109).
- Kreidberg, L. (2015). “batman : BASic Transit Model cAlculationN in Python”. *Publications of the Astronomical Society of the Pacific* 127.957, pp. 1161–1165. DOI: [10.1086/683602](https://doi.org/10.1086/683602) (Cited on page 24).
- (2018a). *Exoplanet Atmosphere Measurements from Transmission Spectroscopy and Other Planet Star Combined Light Observations*, pp. 2083–2105. DOI: [10.1007/978-3-319-55333-7\\_{\\\_}100](https://doi.org/10.1007/978-3-319-55333-7_{\_}100) (Cited on page 16).
- (2018b). “Exoplanet Atmosphere Measurements from Transmission Spectroscopy and Other Planet Star Combined Light Observations”. *Handbook of Exoplanets*. Cham: Springer International Publishing, pp. 2083–2105. DOI: [10.1007/978-3-319-55333-7\\_{\\\_}100](https://doi.org/10.1007/978-3-319-55333-7_{\_}100) (Cited on page 58).
- Kreidberg, L. et al. (2018). *Global climate and atmospheric composition of the ultra-hot jupiter wasp-103b from hst and spitzer phase curve observations*. DOI: [10.3847/1538-3881/aac3df](https://doi.org/10.3847/1538-3881/aac3df) (Cited on pages 76, 112).
- Lainey, V. et al. (2017). “New constraints on Saturn’s interior from Cassini astrometric data”. *Icarus* 281, pp. 286–296. DOI: <https://doi.org/10.1016/j.icarus.2016.07.014> (Cited on page 60).

- Laskar, J and P Robutel (1993). “The chaotic obliquity of the planets”. *Nature* 361.6413, pp. 608–612. DOI: [10.1038/361608a0](https://doi.org/10.1038/361608a0) (Cited on page 84).
- Latham, D. W. et al. (2011). “A first comparison of Kepler planet candidates in single and multiple systems”. *Astrophysical Journal Letters* 732.2 PART II, p. 24. DOI: [10.1088/2041-8205/732/2/L24](https://doi.org/10.1088/2041-8205/732/2/L24) (Cited on page 9).
- Leconte, J., D. Lai, and G. Chabrier (2011). “Distorted, nonspherical transiting planets: impact on the transit depth and on the radius determination”. *Astronomy & Astrophysics* 528, A41. DOI: [10.1051/0004-6361/201015811](https://doi.org/10.1051/0004-6361/201015811) (Cited on pages 61, 68, 112).
- Lee, M. D. and E. J. Wagenmakers (2013). *Bayesian cognitive modeling: A practical course*, pp. 1–264. DOI: [10.1017/CB09781139087759](https://doi.org/10.1017/CB09781139087759) (Cited on pages 29, 30).
- Lendl, M. et al. (2017). “Signs of strong Na and K absorption in the transmission spectrum of WASP-103b”. *Astronomy and Astrophysics* 606. DOI: [10.1051/0004-6361/201731242](https://doi.org/10.1051/0004-6361/201731242) (Cited on pages 16, 112).
- Lendl, M. et al. (2020). “The hot dayside and asymmetric transit of WASP-189 b seen by CHEOPS”. *Astronomy and Astrophysics* 643. DOI: [10.1051/0004-6361/202038677](https://doi.org/10.1051/0004-6361/202038677) (Cited on page 16).
- Li, J. and D. Lai (2020). *Planetary Spin and Obliquity from Mergers*. DOI: [10.3847/2041-8213/aba2c4](https://doi.org/10.3847/2041-8213/aba2c4) (Cited on page 84).
- Lightkurve Collaboration, L. et al. (2018). *Lightkurve: Kepler and TESS time series analysis in Python* (Cited on page 18).
- Lissauer, J. J. (1995). “Urey prize lecture: On the diversity of plausible planetary systems”. *Icarus* 114, pp. 217–236. DOI: [10.1006/icar.1995.1057](https://doi.org/10.1006/icar.1995.1057) (Cited on pages 84, 110).
- Lissauer, J. J. et al. (2011). “Architecture and dynamics of Kepler’s candidate multiple transiting planet systems”. *Astrophysical Journal, Supplement Series* 197.1, p. 8. DOI: [10.1088/0067-0049/197/1/8](https://doi.org/10.1088/0067-0049/197/1/8) (Cited on page 9).
- Lomb, N. R. (1976). “Least-squares frequency analysis of unequally spaced data”. *Astrophysics and Space Science* 39.2, pp. 447–462. DOI: [10.1007/BF00648343](https://doi.org/10.1007/BF00648343) (Cited on page 19).
- Lopez, E. D. and J. J. Fortney (2016). “Re-inflated Warm Jupiters around Red Giants”. *ApJ* 818.1, p. 4. DOI: [10.3847/0004-637X/818/1/4](https://doi.org/10.3847/0004-637X/818/1/4) (Cited on page 55).
- Love, A. E. H. (1911). *Some Problems of Geodynamics* (Cited on pages 59, 60).
- Lovis, C. et al. (2011). “The HARPS search for southern extra-solar planets: XXVIII. Up to seven planets orbiting HD 10180: Probing the architecture of low-mass planetary systems”. *Astronomy and Astrophysics* 528, A112. DOI: [10.1051/0004-6361/201015577](https://doi.org/10.1051/0004-6361/201015577) (Cited on page 5).
- Lovis, C. and D. A. Fischer (2010). “Radial Velocity Techniques for Exoplanets”. *Exoplanets*. Ed. by S. Seager. University of Arizona Press, p. 30 (Cited on page 5).
- Lund, M. N. et al. (2019). “Asteroseismology of the Multiplanet System K2-93”. *arXiv e-prints*, arXiv:1911.07519 (Cited on pages 47, 48, 56).

- Madhusudhan, N. (2018). *Atmospheric Retrieval of Exoplanets*, pp. 2153–2182. DOI: [10.1007/978-3-319-55333-7\\_{\\\_}104](https://doi.org/10.1007/978-3-319-55333-7_{\_}104) (Cited on page 16).
- Marcy, G. W. et al. (2014). “Masses, Radii, and Orbits of Small Kepler Planets: The Transition from Gaseous to Rocky Planets”. *ApJ SS* 210.2, p. 20. DOI: [10.1088/0067-0049/210/2/20](https://doi.org/10.1088/0067-0049/210/2/20) (Cited on page 49).
- Masuda, K (2014). “Very Low Density Planets around Kepler-51 Revealed with Transit Timing Variations and an Anomaly Similar to a Planet-Planet Eclipse Event”. *apj* 783, p. 53. DOI: [10.1088/0004-637X/783/1/53](https://doi.org/10.1088/0004-637X/783/1/53) (Cited on page 46).
- Maxted, P. F. L. (2016). “ellc: A fast, flexible light curve model for detached eclipsing binary stars and transiting exoplanets”. *Astronomy & Astrophysics* 591, A111. DOI: [10.1051/0004-6361/201628579](https://doi.org/10.1051/0004-6361/201628579) (Cited on page 65).
- Maxted, P. F. (2018). “Comparison of the power-2 limb-darkening law from the S TAGGER-grid to Kepler light curves of transiting exoplanets”. *Astronomy and Astrophysics* 616, p. 39. DOI: [10.1051/0004-6361/201832944](https://doi.org/10.1051/0004-6361/201832944) (Cited on pages 11, 79).
- Mayor, M and D Queloz (1995). “A Jupiter-mass companion to a solar-type star”. *nat* 378, pp. 355–359. DOI: [10.1038/378355a0](https://doi.org/10.1038/378355a0) (Cited on page 1).
- Mayor, M. et al. (2011). “The HARPS search for southern extra-solar planets XXXIV. Occurrence, mass distribution and orbital properties of super-Earths and Neptune-mass planets” (Cited on page 5).
- McLaughlin, D. B. (1924). “Some results of a spectrographic study of the Algol system.” *apj* 60. DOI: [10.1086/142826](https://doi.org/10.1086/142826) (Cited on page 13).
- Miller-Ricci, E., S. Seager, and D. Sasselov (2009). “THE ATMOSPHERIC SIGNATURES OF SUPER-EARTHS: HOW TO DISTINGUISH BETWEEN HYDROGEN-RICH AND HYDROGEN-POOR ATMOSPHERES”. *The Astrophysical Journal* 690.2, pp. 1056–1067. DOI: [10.1088/0004-637X/690/2/1056](https://doi.org/10.1088/0004-637X/690/2/1056) (Cited on page 55).
- Milne, E. A. (1921). “Radiative Equilibrium in the Outer Layers of a Star: the Temperature Distribution and the Law of Darkening”. *Monthly Notices of the Royal Astronomical Society* 81.5, pp. 361–375. DOI: [10.1093/mnras/81.5.361](https://doi.org/10.1093/mnras/81.5.361) (Cited on page 11).
- Mooij, E. J. de, C. A. Watson, and M. A. Kenworthy (2017). “Characterizing exo-ring systems around fast-rotating stars using the Rossiter-McLaughlin effect”. *Monthly Notices of the Royal Astronomical Society*. DOI: [10.1093/mnras/stx2142](https://doi.org/10.1093/mnras/stx2142) (Cited on page 38).
- Morello, G, A Tsiaras, I. D. Howarth, and D Homeier (2017). “High-precision Stellar Limb-darkening in Exoplanetary Transits”. *The Astronomical Journal* 154.3, p. 111 (Cited on page 79).
- Mortier, A., J. P. Faria, C. M. Correia, A. Santerne, and N. C. Santos (2015). “BGLS: A Bayesian formalism for the generalised Lomb-Scargle periodogram”. *Astronomy and Astrophysics* 573, p. 101. DOI: [10.1051/0004-6361/201424908](https://doi.org/10.1051/0004-6361/201424908) (Cited on page 20).

- Morton, T. D. (2012). “An efficient automated validation procedure for exoplanet transit candidates”. *Astrophysical Journal* 761.1, p. 6. DOI: [10.1088/0004-637X/761/1/6](https://doi.org/10.1088/0004-637X/761/1/6) (Cited on page 10).
- Müller, H. M. (2015). “Limb-darkening Measurements on Exoplanet Host Stars and the Sun Dissertation”. *PhD Thesis* (Cited on page 12).
- Murray, C. D. and S. F. Dermott (2000). “Tides, Rotation, and Shape”. *Solar System Dynamics*. Cambridge University Press, pp. 130–188. DOI: [10.1017/cbo9781139174817.005](https://doi.org/10.1017/cbo9781139174817.005) (Cited on page 62).
- Neilson, H. R., J. T. McNeil, R. Ignace, and J. B. Lester (2017). “Limb Darkening and Planetary Transits: Testing Center-to-limb Intensity Variations and Limb-darkening Directly from Model Stellar Atmospheres”. *The Astrophysical Journal* 845.1, p. 65 (Cited on page 77).
- Nesvorný, D et al. (2012). “The Detection and Characterization of a Nontransiting Planet by Transit Timing Variations”. *Science* 336, p. 1133. DOI: [10.1126/science.1221141](https://doi.org/10.1126/science.1221141) (Cited on page 13).
- Nesvorný, D. (2019). “How to find a planet from transit variations”. *New Astronomy Reviews* 84, p. 101507. DOI: [10.1016/j.newar.2019.03.001](https://doi.org/10.1016/j.newar.2019.03.001) (Cited on page 12).
- Nesvorný, D. et al. (2013). “KOI-142, the king of transit variations, is a pair of planets near the 2:1 resonance”. *Astrophysical Journal* 777.1, p. 3. DOI: [10.1088/0004-637X/777/1/3](https://doi.org/10.1088/0004-637X/777/1/3) (Cited on page 13).
- Nicholson, P. D. et al. (2008). “A close look at Saturn’s rings with Cassini VIMS”. *Icarus* 193.1, pp. 182–212. DOI: [10.1016/j.icarus.2007.08.036](https://doi.org/10.1016/j.icarus.2007.08.036) (Cited on page 56).
- Ohno, K. and Y. A. Tanaka (2021). “Grain Growth in Escaping Atmospheres: Implications for the Radius Inflation of Super-Puffs” (Cited on page 55).
- Ohta, Y., A. Taruya, and Y. Suto (2009). “Predicting photometric and spectroscopic signatures of rings around transiting extrasolar planets”. *Astrophysical Journal* 690.1, pp. 1–12. DOI: [10.1088/0004-637X/690/1/1](https://doi.org/10.1088/0004-637X/690/1/1) (Cited on pages 38, 43, 48, 110).
- Olmschenk, G. et al. (2021). “Identifying Planetary Transit Candidates in TESS Full-frame Image Light Curves via Convolutional Neural Networks”. *The Astronomical Journal* 161.6, p. 273. DOI: [10.3847/1538-3881/abf4c6](https://doi.org/10.3847/1538-3881/abf4c6) (Cited on page 111).
- Olson, B., I. Hashmi, K. Molloy, and A. Shehu (2012). “Basin Hopping as a General and Versatile Optimization Framework for the Characterization of Biological Macromolecules”. *Advances in Artificial Intelligence* 2012, pp. 1–19. DOI: [10.1155/2012/674832](https://doi.org/10.1155/2012/674832) (Cited on page 24).
- Ortiz, J. L. et al. (2015). “Possible ring material around centaur (2060) Chiron”. *Astronomy and Astrophysics* 576, A18. DOI: [10.1051/0004-6361/201424461](https://doi.org/10.1051/0004-6361/201424461) (Cited on pages 36, 37).
- Ortiz, J. L. et al. (2017). “The size, shape, density and ring of the dwarf planet Haumea from a stellar occultation”. *Nature* 550.7675, pp. 219–223. DOI: [10.1038/nature24051](https://doi.org/10.1038/nature24051) (Cited on pages 36, 37).

- Osborn, H. P. et al. (2020). “Rapid classification of TESS planet candidates with convolutional neural networks”. *Astronomy and Astrophysics* 633. DOI: [10.1051/0004-6361/201935345](https://doi.org/10.1051/0004-6361/201935345) (Cited on page [111](#)).
- Oshagh, M et al. (2013a). “Effect of stellar spots on high-precision transit light-curve”. *\aap* 556, A19. DOI: [10.1051/0004-6361/201321309](https://doi.org/10.1051/0004-6361/201321309) (Cited on page [81](#)).
- Oshagh, M et al. (2013b). “SOAP-T: a tool to study the light curve and radial velocity of a system with a transiting planet and a rotating spotted star”. *\aap* 549, A35. DOI: [10.1051/0004-6361/201220173](https://doi.org/10.1051/0004-6361/201220173) (Cited on page [41](#)).
- Oshagh, M. (2018a). “Noise Sources in Photometry and Radial Velocities”. *Asteroseismology and Exoplanets: Listening to the Stars and Searching for New Worlds*. Ed. by T. L. Campante, N. C. Santos, and M. J. P. F. G. Monteiro. Cham: Springer International Publishing, pp. 239–249 (Cited on pages [18](#), [91](#)).
- (2018b). “Noise Sources in Photometry and Radial Velocities”. *Asteroseismology and Exoplanets: Listening to the Stars and Searching for New Worlds*. Vol. 49, pp. 239–249. DOI: [10.1007/978-3-319-59315-9\\_{\\\_}13](https://doi.org/10.1007/978-3-319-59315-9_{\_}13) (Cited on page [81](#)).
- Parmentier, V. and I. J. M. Crossfield (2018). *Exoplanet Phase Curves: Observations and Theory*, pp. 1419–1440. DOI: [10.1007/978-3-319-55333-7\\_{\\\_}116](https://doi.org/10.1007/978-3-319-55333-7_{\_}116) (Cited on page [58](#)).
- Parviainen, H and S Aigrain (2015). “LDTK: Limb Darkening Toolkit”. *\mnras* 453, pp. 3821–3826. DOI: [10.1093/mnras/stv1857](https://doi.org/10.1093/mnras/stv1857) (Cited on page [31](#)).
- Parviainen, H. (2018). “Bayesian Methods for Exoplanet Science”. *Handbook of Exoplanets*. Cham: Springer International Publishing, pp. 1567–1590. DOI: [10.1007/978-3-319-55333-7\\_{\\\_}149](https://doi.org/10.1007/978-3-319-55333-7_{\_}149) (Cited on pages [26](#), [27](#)).
- Pater, I. d. and J. J. Lissauer (2015). “Planetary Rings”. *Planetary Sciences*. Cambridge University Press, pp. 448–488. DOI: [10.1017/cbo9781316165270.012](https://doi.org/10.1017/cbo9781316165270.012) (Cited on page [39](#)).
- Peale, S. J. (1999). “Origin and Evolution of the Natural Satellites”. *\araa* 37, pp. 533–602. DOI: [10.1146/annurev.astro.37.1.533](https://doi.org/10.1146/annurev.astro.37.1.533) (Cited on page [89](#)).
- Pepe, F. et al. (2002). “HARPS: ESO’s coming planet searcher. Chasing exoplanets with the La Silla 3.6-m telescope”. *The Messenger* 110 (Cited on page [4](#)).
- Pepe, F., F. Bouchy, M. Mayor, and S. Udry (2018). *High-Precision Spectrographs for Exoplanet Research: CORAVEL, ELODIE, CORALIE, SOPHIE and HARPS*, pp. 855–882. DOI: [10.1007/978-3-319-55333-7\\_{\\\_}190](https://doi.org/10.1007/978-3-319-55333-7_{\_}190) (Cited on page [4](#)).
- Pereira, F. et al. (2019). “Gaussian process modelling of granulation and oscillations in red giant stars”. *Monthly Notices of the Royal Astronomical Society* 489.4, pp. 5764–5774. DOI: [10.1093/mnras/stz2405](https://doi.org/10.1093/mnras/stz2405) (Cited on page [81](#)).
- Perryman, M. (2018). *The Exoplanet Handbook*. Cambridge University Press. DOI: [10.1017/9781108304160](https://doi.org/10.1017/9781108304160) (Cited on pages [3](#), [4](#), [8](#), [39](#)).

- Piro, A. L. and S. Vissapragada (2020). “Exploring Whether Super-puffs can be Explained as Ringed Exoplanets”. *The Astronomical Journal* 159.4, p. 131. DOI: [10.3847/1538-3881/ab7192](https://doi.org/10.3847/1538-3881/ab7192) (Cited on page 46).
- Pollacco, D. et al. (2006). “The WASP project and SuperWASP camera”. *Astrophysics and Space Science*. Vol. 304. 1-4. Springer, pp. 253–255. DOI: [10.1007/s10509-006-9124-x](https://doi.org/10.1007/s10509-006-9124-x) (Cited on page 9).
- Pont, F, S Zucker, and D Queloz (2006). “The effect of red noise on planetary transit detection”. *\mnras* 373, pp. 231–242. DOI: [10.1111/j.1365-2966.2006.11012.x](https://doi.org/10.1111/j.1365-2966.2006.11012.x) (Cited on page 79).
- Queloz, D. et al. (2000). “Detection of a spectroscopic transit by the planet orbiting the star HD209458”. *Astronomy and Astrophysics* 359.2 (Cited on page 14).
- Quirrenbach, A et al. (2016). “CARMENES: an overview six months after first light”. *\procspie*. Vol. 9908. Society of Photo-Optical Instrumentation Engineers (SPIE) Conference Series. SPIE, p. 990812. DOI: [10.1117/12.2231880](https://doi.org/10.1117/12.2231880) (Cited on page 100).
- Ragozzine, D. and A. S. Wolf (2009). “PROBING THE INTERIORS OF VERY HOT JUPITERS USING TRANSIT LIGHT CURVES”. *The Astrophysical Journal* 698.2, pp. 1778–1794. DOI: [10.1088/0004-637X/698/2/1778](https://doi.org/10.1088/0004-637X/698/2/1778) (Cited on pages 60–62, 109).
- Rao, S., A. Mahabal, N. Rao, and C. Raghavendra (2021). “Nigraha: Machine-learning-based pipeline to identify and evaluate planet candidates from TESS”. *Monthly Notices of the Royal Astronomical Society* 502.2, pp. 2845–2858. DOI: [10.1093/mnras/stab203](https://doi.org/10.1093/mnras/stab203) (Cited on page 111).
- Rasmussen, C. E. and C. K. I. Williams (2006). *Gaussian Processes for Machine Learning*. Cambridge, Massachusetts: the MIT Press (Cited on page 21).
- Rauer, H. et al. (2014). “The PLATO 2.0 mission”. *Experimental Astronomy* 38.1-2, pp. 249–330. DOI: [10.1007/s10686-014-9383-4](https://doi.org/10.1007/s10686-014-9383-4) (Cited on pages 10, 77, 100).
- Reiners, A. et al. (2018). “The CARMENES search for exoplanets around M dwarfs: High-resolution optical and near-infrared spectroscopy of 324 survey stars”. *Astronomy and Astrophysics* 612. DOI: [10.1051/0004-6361/201732054](https://doi.org/10.1051/0004-6361/201732054) (Cited on page 5).
- Ricker, G. R. et al. (2015). “Transiting Exoplanet Survey Satellite (TESS)”. *Journal of Astronomical Telescopes, Instruments, and Systems* 1.1, p. 14003. DOI: [10.1117/1.JATIS.1.1.014003](https://doi.org/10.1117/1.JATIS.1.1.014003) (Cited on page 9).
- Rossiter, R. A. (1924). “On the detection of an effect of rotation during eclipse in the velocity of the brighter component of beta Lyrae, and on the constancy of velocity of this system.” *\apj* 60. DOI: [10.1086/142825](https://doi.org/10.1086/142825) (Cited on page 13).
- Rowe, J. F. et al. (2014). “Validation of kepler’s multiple planet candidates. III. light curve analysis and announcement of hundreds of new multi-planet systems”. *Astrophysical Journal* 784.1, p. 45. DOI: [10.1088/0004-637X/784/1/45](https://doi.org/10.1088/0004-637X/784/1/45) (Cited on page 103).



- Saad-Olivera, X., D. Nesvorný, D. M. Kipping, and F. Roig (2017). “Masses of Kepler-46b, c from Transit Timing Variations”. *The Astronomical Journal* 153.4, p. 198. DOI: [10.3847/1538-3881/aa64e0](https://doi.org/10.3847/1538-3881/aa64e0) (Cited on pages [103](#), [104](#)).
- Sabadini, R and B Vermeersen (2004). *Global Dynamics of the Earth: Applications of Normal Mode Relaxation Theory to Solid-Earth Geophysics*. Kluwer Academic Publishers (Cited on page [60](#)).
- Sanchis-Ojeda, R. and J. N. Winn (2011). “Starspots, Spin-Orbit Misalignment, and Active Latitudes in the HAT-P-11 Exoplanetary System”. *The Astrophysical Journal* 743.1, p. 61 (Cited on page [16](#)).
- Santerne, A. et al. (2013). “The contribution of secondary eclipses as astrophysical false positives to exoplanet transit surveys”. *Astronomy and Astrophysics* 557, A139. DOI: [10.1051/0004-6361/201321475](https://doi.org/10.1051/0004-6361/201321475) (Cited on page [10](#)).
- Santerne, A. et al. (2019). “An extremely low-density and temperate giant exoplanet”. *arXiv* (Cited on pages [46](#), [47](#), [49](#), [56](#)).
- Santos, N. C. et al. (2015). “Detecting ring systems around exoplanets using high resolution spectroscopy: the case of 51 Pegasi b”. *AAS* 583, A50. DOI: [10.1051/0004-6361/201526673](https://doi.org/10.1051/0004-6361/201526673) (Cited on pages [38](#), [111](#)).
- Santos, N. C. et al. (2017). “Constraining planet structure and composition from stellar chemistry: Trends in different stellar populations”. *Astronomy and Astrophysics* 608. DOI: [10.1051/0004-6361/201731359](https://doi.org/10.1051/0004-6361/201731359) (Cited on page [59](#)).
- Santos, N. C. et al. (2020). “Detection and Characterization Methods of Exoplanets”. *Oxford Research Encyclopedia of Planetary Science*. DOI: [10.1093/acrefore/9780190647926.013.189](https://doi.org/10.1093/acrefore/9780190647926.013.189) (Cited on page [3](#)).
- Savitzky, A. and M. J. Golay (1964). “Smoothing and Differentiation of Data by Simplified Least Squares Procedures”. *Analytical Chemistry* 36.8, pp. 1627–1639. DOI: [10.1021/ac60214a047](https://doi.org/10.1021/ac60214a047) (Cited on page [23](#)).
- Scargle, J. D. (1982). “Studies in astronomical time series analysis. II - Statistical aspects of spectral analysis of unevenly spaced data”. *The Astrophysical Journal* 263, p. 835. DOI: [10.1086/160554](https://doi.org/10.1086/160554) (Cited on page [19](#)).
- Schlichting, H. E. (2018). “Formation of Super-Earths”. *Handbook of Exoplanets*. Vol. 3. 6. Cham: Springer International Publishing, pp. 2345–2364. DOI: [10.1007/978-3-319-55333-7\\_141](https://doi.org/10.1007/978-3-319-55333-7_141) (Cited on page [9](#)).
- Schlichting, H. E. and P. Chang (2011). “Warm Saturns: On the Nature of Rings around Extrasolar Planets That Reside inside the Ice Line”. *The Astrophysical Journal* 734.2, p. 117 (Cited on pages [37](#), [40](#), [46](#), [53](#)).
- Seager, S. and L. Hui (2002). “Constraining the Rotation Rate of Transiting Extrasolar Planets by Oblateness Measurements”. *The Astrophysical Journal* 574.2, pp. 1004–1010. DOI: [10.1086/340994](https://doi.org/10.1086/340994) (Cited on pages [61](#), [70](#), [83](#), [84](#), [86](#), [87](#), [89](#), [92](#)).

- Seager, S and G Mallen-Ornelas (2003). “A Unique Solution of Planet and Star Parameters from an Extrasolar Planet Transit Light Curve”. *The Astrophysical Journal* 585.2, pp. 1038–1055. DOI: [10.1086/346105](https://doi.org/10.1086/346105) (Cited on page 7).
- Short, D. R., W. F. Welsh, J. A. Orosz, G. Windmiller, and P. F. L. Maxted (2019). “Note on the Power-2 Limb-darkening Law”. *Research Notes of the AAS* 3.8, p. 117. DOI: [10.3847/2515-5172/ab3a3e](https://doi.org/10.3847/2515-5172/ab3a3e) (Cited on page 12).
- Sing, D. K. et al. (2009). “Transit spectrophotometry of the exoplanet HD 189733b: I. Searching for water but finding haze with HST NICMOS”. *Astronomy and Astrophysics* 505.2, pp. 891–899. DOI: [10.1051/0004-6361/200912776](https://doi.org/10.1051/0004-6361/200912776) (Cited on page 11).
- Skilling, J. (2004). “Nested Sampling”. *AIP Conference Proceedings*. Vol. 735. AIP, pp. 395–405. DOI: [10.1063/1.1835238](https://doi.org/10.1063/1.1835238) (Cited on page 29).
- (2006). “Nested sampling for general Bayesian computation”. *Bayesian Analysis* 1.4, pp. 833–860. DOI: [10.1214/06-BA127](https://doi.org/10.1214/06-BA127) (Cited on page 29).
- Snellen, I. A. et al. (2014). “Fast spin of the young extrasolar planet  $\beta$  Pictoris b”. *Nature* 508.7498, pp. 63–65. DOI: [10.1038/nature13253](https://doi.org/10.1038/nature13253) (Cited on page 107).
- Sotin, C., O. Grasset, and A. Mocquet (2007). “Mass-radius curve for extrasolar Earth-like planets and ocean planets”. *Icarus* 191.1, pp. 337–351. DOI: [10.1016/j.icarus.2007.04.006](https://doi.org/10.1016/j.icarus.2007.04.006) (Cited on page 59).
- Southworth, J et al. (2015). “High-precision photometry by telescope defocusing - VII. The ultrashort period planet WASP-103”. *mnras* 447, pp. 711–721. DOI: [10.1093/mnras/stu2394](https://doi.org/10.1093/mnras/stu2394) (Cited on page 61).
- Southworth, J. and D. F. Evans (2016). “Contamination from a nearby star cannot explain the anomalous transmission spectrum of the ultrashort period giant planet WASP-103 b”. *Monthly Notices of the Royal Astronomical Society* 463.1, pp. 37–44. DOI: [10.1093/mnras/stw1943](https://doi.org/10.1093/mnras/stw1943) (Cited on pages 66, 67).
- Sozzetti, A. et al. (2021). “A sub-Neptune and a non-transiting Neptune-mass companion unveiled by ESPRESSO around the bright late-F dwarf HD 5278 (TOI-130)”. *Astronomy and Astrophysics* 648. DOI: [10.1051/0004-6361/202040034](https://doi.org/10.1051/0004-6361/202040034) (Cited on page 5).
- Speagle, J. S. (2019). “dynesty: A Dynamic Nested Sampling Package for Estimating Bayesian Posteriors and Evidences”. *arXiv e-prints*, arXiv:1904.02180 (Cited on page 30).
- Spiegel, D. S., A. Burrows, and J. A. Milsom (2011). “The deuterium-burning mass limit for brown dwarfs and giant planets”. *Astrophysical Journal* 727.1, p. 57. DOI: [10.1088/0004-637X/727/1/57](https://doi.org/10.1088/0004-637X/727/1/57) (Cited on page 2).
- Steffen, J. H. et al. (2013). “Transit timing observations from Kepler - VII. Confirmation of 27 planets in 13 multiplanet systems via transit timing variations and orbital stability”. *Monthly Notices of the Royal Astronomical Society* 428.2, pp. 1077–1087. DOI: [10.1093/mnras/sts090](https://doi.org/10.1093/mnras/sts090) (Cited on page 13).

- Sterne, T. E. (1939). “Apsidal Motion in Binary Stars”. *Monthly Notices of the Royal Astronomical Society* 99.5, pp. 451–462. DOI: [10.1093/mnras/99.5.451](https://doi.org/10.1093/mnras/99.5.451) (Cited on pages [60](#), [61](#)).
- Storn, R. and K. Price (1997). “Differential Evolution - A Simple and Efficient Heuristic for Global Optimization over Continuous Spaces”. *Journal of Global Optimization* 11.4, pp. 341–359. DOI: [10.1023/A:1008202821328](https://doi.org/10.1023/A:1008202821328) (Cited on page [24](#)).
- Sucerquia, M., J. A. Alvarado-Montes, J. I. Zuluaga, M. Montesinos, and A. Bayo (2020). “Scattered light may reveal the existence of ringed exoplanets”. *Monthly Notices of the Royal Astronomical Society: Letters* 496.1, pp. L85–L90. DOI: [10.1093/mnrasl/slaa080](https://doi.org/10.1093/mnrasl/slaa080) (Cited on pages [38](#), [111](#)).
- Szabó, G. M., K Szatmáry, Z. Divéki, and A Simon (2006). “Possibility of a photometric detection of “exomoons” (Research Note)”. *Astronomy and Astrophysics* 450.1, pp. 395–398. DOI: [10.1051/0004-6361:20054555](https://doi.org/10.1051/0004-6361:20054555) (Cited on page [13](#)).
- Tabernero, H. M. et al. (2021). “ESPRESSO high-resolution transmission spectroscopy of WASP-76 b”. *Astronomy and Astrophysics* 646, A158. DOI: [10.1051/0004-6361/202039511](https://doi.org/10.1051/0004-6361/202039511) (Cited on page [16](#)).
- Tinetti, G. et al. (2016). “The science of ARIEL (Atmospheric Remote-sensing Infrared Exoplanet Large-survey)”. *Space Telescopes and Instrumentation 2016: Optical, Infrared, and Millimeter Wave*. Vol. 9904. International Society for Optics and Photonics, p. 99041X. DOI: [10.1117/12.2232370](https://doi.org/10.1117/12.2232370) (Cited on page [10](#)).
- Torres, G, J. N. Winn, and M. J. Holman (2008). “Improved Parameters for Extrasolar Transiting Planets”. *apj* 677, pp. 1324–1342. DOI: [10.1086/529429](https://doi.org/10.1086/529429) (Cited on page [87](#)).
- Torres, G. et al. (2011). “Modeling Kepler transit light curves as false positives: Rejection of blend scenarios for Kepler-9, and validation of Kepler-9 d, a super-earth-size planet in a multiple system”. *Astrophysical Journal* 727.1, p. 24. DOI: [10.1088/0004-637X/727/1/24](https://doi.org/10.1088/0004-637X/727/1/24) (Cited on page [10](#)).
- Tremaine, S., J. Touma, and F. Namouni (2009). “Satellite dynamics on the Laplace surface”. *AJ* 137.3, pp. 3706–3717. DOI: [10.1088/0004-6256/137/3/3706](https://doi.org/10.1088/0004-6256/137/3/3706) (Cited on page [40](#)).
- Triaud, A. H. M. J. et al. (2009). “The Rossiter-McLaughlin effect of CoRoT-3b and HD 189733b”. *Astronomy & Astrophysics* 506.1, pp. 377–384. DOI: [10.1051/0004-6361/200911897](https://doi.org/10.1051/0004-6361/200911897) (Cited on pages [87](#), [88](#)).
- Triaud, A. H. M. J. (2018). *The RossiterMcLaughlin Effect in Exoplanet Research*. 2000, pp. 1375–1401. DOI: [10.1007/978-3-319-55333-7\\_{\}\\_2](https://doi.org/10.1007/978-3-319-55333-7_{\}_2) (Cited on page [14](#)).
- Tusnski, L. R. M. and A. Valio (2011). “Transit Model of Planets with Moon and Ring Systems”. *The Astrophysical Journal* 743.1, p. 97 (Cited on page [38](#)).
- Udalski, A. et al. (2003). “The Optical Gravitational Lensing Experiment. Additional Planetary and Low-Luminosity Object Transits from the OGLE 2001 and 2002 Observational Campaigns”. *Acta Astronomica* 53.2, pp. 133–149 (Cited on page [9](#)).

- Ulmer-Moll, S, N. C. Santos, P Figueira, J Brinchmann, and J. P. Faria (2019). “Beyond the exoplanet mass-radius relation”. *A&A* 630, A135. DOI: [10.1051/0004-6361/201936049](https://doi.org/10.1051/0004-6361/201936049) (Cited on page 53).
- Vanderburg, A and J. A. Johnson (2014). “A Technique for Extracting Highly Precise Photometry for the Two-Wheeled Kepler Mission”. *PASP* 126, p. 948. DOI: [10.1086/678764](https://doi.org/10.1086/678764) (Cited on page 47).
- Vanderburg, A. et al. (2016). “Five Planets Transiting a Ninth Magnitude Star”. *The Astrophysical Journal* 827.1, p. L10. DOI: [10.3847/2041-8205/827/1/L10](https://doi.org/10.3847/2041-8205/827/1/L10) (Cited on page 46).
- VanderPlas, J. T. (2018). “Understanding the LombScargle Periodogram”. *The Astrophysical Journal Supplement Series* 236.1, p. 16. DOI: [10.3847/1538-4365/aab766](https://doi.org/10.3847/1538-4365/aab766) (Cited on page 20).
- Virtanen, P. et al. (2020). “{SciPy} 1.0: Fundamental Algorithms for Scientific Computing in Python”. *Nature Methods* 17, pp. 261–272. DOI: [10.1038/s41592-019-0686-2](https://doi.org/10.1038/s41592-019-0686-2) (Cited on page 24).
- Wang, L. and F. Dai (2019). “Dusty Outflows in Planetary Atmospheres: Understanding  $\{ \text{textquotedblleft} \}$ Suppuffs $\{ \text{textquotedblright} \}$  and Transmission Spectra of Sub-Neptunes”. *ApJL* 873.1, p. L1. DOI: [10.3847/2041-8213/ab0653](https://doi.org/10.3847/2041-8213/ab0653) (Cited on page 55).
- Wang, Y.-H. et al. (2019). “Transiting Exoplanet Monitoring Project (TEMP). V. Transit Follow Up for HAT-P-9b, HAT-P-32b, and HAT-P-36b”. *The Astronomical Journal* 157.2, p. 82. DOI: [10.3847/1538-3881/aaf6b6](https://doi.org/10.3847/1538-3881/aaf6b6) (Cited on page 66).
- West, R. G. et al. (2016). “Three irradiated and bloated hot Jupiters:: WASP-76b, WASP-82b, and WASP-90b”. *Astronomy and Astrophysics* 585. DOI: [10.1051/0004-6361/201527276](https://doi.org/10.1051/0004-6361/201527276) (Cited on page 66).
- Winn, J. N., D. Fabrycky, S. Albrecht, and J. A. Johnson (2010). “Hot stars with hot jupiters have high obliquities”. *Astrophysical Journal Letters* 718.2 PART 2, pp. 145–149. DOI: [10.1088/2041-8205/718/2/L145](https://doi.org/10.1088/2041-8205/718/2/L145) (Cited on page 14).
- Winter, O. C. and E. V. Neto (2001). “Time analysis for temporary gravitational capture stable orbits”. *Astronomy and Astrophysics* 377.3, pp. 1119–1127. DOI: [10.1051/0004-6361:20011165](https://doi.org/10.1051/0004-6361:20011165) (Cited on page 39).
- Wong, I. et al. (2016). “3.6 AND 4.5  $\mu$  m SPITZER PHASE CURVES OF THE HIGHLY IRRADIATED HOT JUPITERS WASP-19b AND HAT-P-7b”. *The Astrophysical Journal* 823.2, p. 122. DOI: [10.3847/0004-637x/823/2/122](https://doi.org/10.3847/0004-637x/823/2/122) (Cited on page 66).
- Wytttenbach, A, D Ehrenreich, C Lovis, S Udry, and F Pepe (2015). “Spectrally resolved detection of sodium in the atmosphere of HD 189733b with the HARPS spectrograph”. *Astronomy & Astrophysics* 577, A62. DOI: [10.1051/0004-6361/201525729](https://doi.org/10.1051/0004-6361/201525729) (Cited on page 87).
- Xiang, Y., D. Y. Sun, W. Fan, and X. G. Gong (1997). “Generalized simulated annealing algorithm and its application to the Thomson model”. *Physics Letters, Section A: General,*

- Atomic and Solid State Physics* 233.3, pp. 216–220. DOI: [10.1016/S0375-9601\(97\)00474-X](https://doi.org/10.1016/S0375-9601(97)00474-X) (Cited on page [24](#)).
- Zechmeister, M. and M. Kürster (2009). “The generalised Lomb-Scargle periodogram a new formalism for the floating-mean and Keplerian periodograms”. *Astronomy and Astrophysics* 496.2, pp. 577–584. DOI: [10.1051/0004-6361:200811296](https://doi.org/10.1051/0004-6361:200811296) (Cited on page [20](#)).
- Zeng, L. and D. Sasselov (2013). “A Detailed Model Grid for Solid Planets from 0.1 through 100 Earth Masses”. *Publications of the Astronomical Society of the Pacific* 125.925, pp. 227–239. DOI: [10.1086/669163](https://doi.org/10.1086/669163) (Cited on page [59](#)).
- Zhu, W., C. X. Huang, G. Zhou, and D. N. C. Lin (2014). “Constraining the Oblateness of Kepler Planets”. *The Astrophysical Journal* 796.1, p. 67. DOI: [10.1088/0004-637X/796/1/67](https://doi.org/10.1088/0004-637X/796/1/67) (Cited on pages [84](#), [87](#), [90](#)).
- Zuluaga, J. I., D. M. Kipping, M. Sucerquia, and J. A. Alvarado (2015). “A Novel Method for Identifying Exoplanetary Rings”. *The Astrophysical Journal Letters* 803.1, p. L14 (Cited on pages [41](#), [110](#)).